Title
Development of a methodology to evaluate material accountability in pyroprocess

Author
Woo, Seung Min

Publication Date
2017

Peer reviewed|Thesis/dissertation

Development of a methodology to evaluate material accountability in pyroprocess

by

Seungmin Woo

A dissertation submitted in partial satisfaction of the

requirements for the degree of

Doctor of Philosophy

in

Engineering - Nuclear Engineering

in the

Graduate Division

of the

University of California, Berkeley

Committee in charge:

Professor Massimiliano Fratoni, Chair
Professor Ehud Greenspan
Professor Rhonda Righter

Spring 2017

Abstract

Development of a methodology to evaluate material accountability in pyroprocess

by

Seungmin Woo

Doctor of Philosophy in Nuclear Engineering

University of California, Berkeley

Professor Massimiliano Fratoni, Chair

This study investigates the effect of the non-uniform nuclide composition in spent fuel on material accountancy in the pyroprocess. High-fidelity depletion simulations are performed using the Monte Carlo code SERPENT in order to determine nuclide composition as a function of axial and radial position within fuel rods and assemblies, and burnup. For improved accuracy, the simulations use short burnups step (25 days or less), Xe-equilibrium treatment (to avoid oscillations over burnup steps), axial moderator temperature distribution, and 30 axial meshes.

Analytical solutions of the simplified depletion equations are built to understand the axial non-uniformity of nuclide composition in spent fuel. The cosine shape of axial neutron flux distribution dominates the axial non-uniformity of the nuclide composition. Combined cross sections and time also generate axial non-uniformity, as the exponential term in the analytical solution consists of the neutron flux, cross section and time. The axial concentration distribution for a nuclide having the small cross section gets steeper than that for another nuclide having the great cross section because the axial flux is weighted by the cross section in the exponential term in the analytical solution. Similarly, the non-uniformity becomes flatter as increasing burnup, because the time term in the exponential increases.

Based on the developed numerical recipes and decoupling of the results between the axial distributions and the predetermined representative radial distributions by matching the axial height, the axial and radial composition distributions for representative spent nuclear fuel assemblies, the Type-0, -1, and -2 assemblies after 1, 2, and 3 depletion cycles, are obtained. These data are appropriately modified to depict processing for materials in the head-end process of pyroprocess that is chopping, voloxidation and granulation. The expectation and standard deviation of the Pu-to-^{244}Cm-ratio by the single granule sampling calculated by the central limit theorem and the Geary-Hinkley transformation. Then, the uncertainty propagation through the key-pyroprocess is conducted to analyze the Material Unaccounted For (MUF), which is a random variable defined as a receipt minus a shipment of a process, in the system. Finally, the Type-I error for the Pu MUF is evaluated for spent fuel assemblies with respect the size of granules and powders which are the key parameters to evaluate the uncertainty in determining ratio by sampling. The main observations of this calculation are the following: (1) the probabilities of Type-I error for the Pu MUF are occasionally greater than 5% when the size of powder particles and granules are large and small; (2) the possibility of Type-I error greater than 5% increases by increasing the depletion

period, because the increasing production of Pu and ^{244}Cm with increasing burnup propagates the uncertainty through the system; (3) the major contributor to the uncertainty of ratio is the non-uniformity of ^{244}Cm; (4) Pu generation in the Type-2 spent fuel assemblies is greater that in the others due to higher gadolinia bearing fuel (GBF) loading in the assembly, therefore, the area indicating the probability of Type-I error greater than or equal to 5% is the widest among the figures for the Type-0 and -1 spent fuel assemblies.

The random variable, LOPu, is defined for evaluating the non-detection probability at each Key Measurement Point (KMP) as the original Pu mass minus the Pu mass after a missing scenario. A number of assemblies for the LOPu to be 8 kg is considered in this calculation. The probability of detection for the 8 kg LOPu is evaluated with respect the size of granule and powder using the event tree analysis and the hypothesis testing method. We can observe there are possible cases showing the probability of detection for the 8 kg LOPu less than 95%. In order to enhance the detection rate, a new Material Balance Area (MBA) model is defined for the key-pyroprocess. The probabilities of detection for all spent fuel types based on the new MBA model are greater than 99%. Furthermore, it is observed that the probability of detection significantly increases by increasing granule sample sizes to evaluate the Pu-to-^{244}Cm-ratio before the key-pyroprocess.

Based on these observations, even though the Pu material accountability in pyroprocess is affected by the non-uniformity of nuclide composition when the Pu-to-^{244}Cm-ratio method is being applied, that is surmounted by decreasing the uncertainty of measured ratio by increasing sample sizes and modifying the MBAs and KMPs.

Acknowledgement

I would like to express the deepest appreciation to Professor Joonhong Ahn. Without your teaching and supporting, I would not have completed this dissertation. I will keep in mind all lessons you have given me during the time with you. I pray for the repose of the deceased.

I would also like to thank Professor Massimiliano Fratoni, Ehud Greenspan, and Rhonda Righter, for your mentorship. Your help makes me to complete this dissertation.

I would greatly appreciate my mentors, Professor Soon Heung Chang, Dr. Yoon Il Chang and Yongsoo Hwang, Professor Man-Sung Yim, Yong Hoon Jeong and Gyunyoung Heo, who have encouraged me.

I would like to thank my great Nuclear Waste Management Lab. mates, Xudong Liu, Milos Atz, Kyungjin Lee, Alex Salazar, Jihae Yoon, Sung Woo Kwak, Bret Patrick van den Akker, Elsa Lemaître-xavier, Esra Orucoglu, R. A. Borrelli and many visiting scholars, and my great colleague, Guanheng Zhang, Phil Gorman and Manuele Aufiero.

Lastly, I would like to greatly appreciate my family. I am very sure that I could not have made it anything without you. I am a person who should say ‘I thank you and I love you’.

Contents

LIST OF FIGURES

LIST OF TABLES

Chapter 1

Introduction

1.1 Background

The pyroprocessing technology, which was originally suggested and developed by Argonne National Laboratory (ANL) to be applied for the Integral Fast Reactor (IFR) in 1960s [1], has been developed by Korea Atomic Energy Research Institute (KAERI) for recycling of spent nuclear fuels since 1997 [2,3]. KAERI has shown interest in pyroprocess for the following reasons: (1) to reduce the volume of nuclear waste from Pressurized Water Reactor (PWR) spent fuels, (2) to produce transuranic (TRU) metal fuel for the Sodium-cooled Fast Reactor (SFR), (3) to reuse useful material in spent fuel, (4) to reduce heat generation from spent fuel and, (5) to reduce the toxicity of spent fuel [2,4].

Pyroprocess mainly consists of the head-end process, the key-pyroprocess, the storage and the waste treatment process [5]. The nuclear spent fuel after discharging and cooling time (e.g., 5 years) is firstly treated in the head-end process. The spent fuel assembly is disassembled and chopped. The length of the chopped pieces has not been clearly decided. However, some previous studies have mentioned as 1 to 2 inches [6], 30 to 50 mm [7], and 1.01 cm [8] in length. After chopping, KAERI has conducted experimental studies for the voloxidation coupled with oxidative decladding, which shows greater recovery rate of nuclear fuel materials from rod-cuts than the mechanical decladding [2,8]. The main purposes of this process are the oxidation of UO_2 into the U_3O_8 in the powder type and the volatilization of fission products such as Kr, Xe, and I_2, etc. After voloxidation, the pre-treatment process would be planned. The U_3O_8 powder generated from voloxidation as a feed material for the electrolytic-reduction process shows advantages; however, it requires a well-designed cathode basket for electrolytic-reduction process [2,9]; therefore, the pretreatment such as the porous pellet manufacturing [8,10] or the granulation process [9,11] has been suggested. The first of key-pyroprocess is the electrolytic-reduction process. In this process, metal oxide feed materials are reduced to the metal (M) type in the LiCl-Li_2O electrolyte as shown in below [2];

$$M_xO_y + 2yLi \rightarrow xM + yLi_2O \quad (1.1)$$

The electrolytic-reduction process has been developed not only to reduce the volume of feed material for electro-refining, but also to dissolve fission products remained under the 650^oC operating temperature. The products contain metals and salt which is around 20% of metal products. In order to remover the salts, the cathode process has been developed. The metals including uranium (U), TRU, and rare earth (RE) materials are installed at the anode cell

surrounded by the LiCl-KCl molten salt solution for the electro-refining process. By this process, U is selectively deposited on the cathode by controlling a cell voltage and the rest of metals, TUR, RE and small amount of U, are dissolved in the molten salt as shown in Eq. (1.2) [12,13].

$$\text{Anode: } U \rightarrow U^{3+} + e^{3-} \qquad \text{Cathode: } U^{3+} + e^{3-} \rightarrow U \tag{1.2}$$

$$Nd \rightarrow Nd^{3+} + e^{3-}$$

$$Pu \rightarrow Pu^{3+} + e^{3-}$$

The U product is finally stored by the U-ingot form through the salt distillation and U-ingot casting processes. The rest of metals (TRU and RE) dissolved in the molten salt is transported into the electro-winning process. This process leads the pyroprocessing system has a great feature in term of non-proliferation, because all TRUs and the small amount of resting U in the salt are deposited together in the liquid cadmium cathode (LCC) [2]. Finally, TRU and U are recovered from the LCC.

Even though the pyroprocess shows advantages in term of proliferation resistance as well as reducing and reusing spent fuel from PWR, the system would not be operated without establishing material accountancy. The reason of that is that material accountancy is a fundamental basis for safeguards against weapons proliferation [14]. Therefore, the reliable material accountancy must be established before starting operation of a nuclear facility such as the pyroprocessing system.

In order to establish material accountancy, the amount of Pu in spent fuel and reprocessing wastes can be verified by counting neutrons emission from ^{244}Cm based on Eq. (1.3) [15]. This method is called Pu-to-Cm-ratio method.

$$\left(\text{Pu mass}\right) = \left(\frac{\text{Pu}}{^{244}\text{Cm}}\right) \times \left(^{244}\text{Cm mass}\right) \tag{1.3}$$

First, the mass of ^{244}Cm can be directly measured by measuring neutron count rates, because neutrons from spent fuel are mostly generated by the spontaneous fission of ^{244}Cm [15]. The ratio of Pu-to-^{244}Cm can be determined either by numerical evaluation with a fuel burnup code [16], destructive assay (DA), or Non-destructive assay (NDA) methods by taking samples [15].

Inaccuracy in this method occurs in each term of the right-hand side of Eq. (1.1). For example, existence of minor neutron sources other than ^{244}Cm [15], such as ^{240}Pu and ^{246}Cm, affect the accuracy of the ^{244}Cm mass measurement, even though their contribution is small. In order to enhance the accuracy of ^{244}Cm measuring, the advanced neutron detecting system has been developed [17,18]. In reference [17], DUPIC safeguards Neutron Counter (DSNC) is developed by the joint research between KAERI and LANL and authorized by International Atomic Energy Agency (IAEA). Borrelli has analyzed the expected magnitude of neutron fluxes by spontaneous fission from ^{244}Cm in the fuel fabrication hot cell of pyroprocess [19]. Moreover, in order to

support the NDA analysis for measuring ^{244}Cm, characterization of neutron sources term has been conducted [20]. When the Pu-to-^{244}Cm-ratio is evaluated by numerical simulations, the expected uncertainty sources are input sources such as the cross-section data and design parameters associated with manufacturing uncertainties [21], and numerical errors itself. Moreover, the value of the Pu-to-^{244}Cm-ratio can vary significantly because of non-uniformity of Pu [22] and ^{244}Cm [15] concentration in spent fuel and batches at various stages of pyroprocessing. It is imperative to establish numerical models to accurately estimate non-uniformity of the ratio within a spent fuel assembly as well as the evaluation of the ratio through pyroprocessing stages. The Pu-to-^{244}Cm-ratio setting before the key-pyroprocess is assumed that the ratio has not varied during the entire process, because it is claimed that Pu and Cm cannot be separated in the system [23]. Therefore, material accountancy could be negatively affected by various uncertainty sources. In this study, we primarily focus on evaluating non-uniform nuclide compositions in spent fuel and how that affects material accountancy in pyroprocess.

1.2 Scope and objective

Recognizing the aforementioned problem, a research is proposed to investigate mechanisms of error generation in the Pu-to-^{244}Cm-ratio method that utilizes Eq. (1.3) and its propagation through the system. The first objective of this study is the development of a numerical recipes from high-fidelity depletion simulation to obtain non-uniformity of Pu and ^{244}Cm concentration. The results in this task have been utilized as an input data for the evaluation of material accountability. Based on this, how that non-uniformity affects material accountancy in the pyroprocessing system has been analyzed when the Pu-to-^{244}Cm-ratio method is applied. After understanding how the uncertainty for material accounting is generated, the performance assessment for material accountability as the third objective has been conducted. The performance metric for the assessment is the probability of Type-I error for the Pu Material Unaccounted For (MUF) and the probability of detection for the loss of Pu (LOPu), which are compared with the current criteria.

Chapter 2

Methodology

2.1 Overall approach for the uncertainty quantification

In order to investigate the mechanisms of error generations by the non-uniformity of nuclide concentration in spent fuel and its propagation through the system, this study consists of the detailed simulations for burnup of nuclear fuel and for the error propagation based on the developed mass-flow in the pyroprocessing system. To begin with, in order to obtain non-uniformity of nuclide concentration for Pu and ^{244}Cm, a numerical recipe for high-fidelity depletion simulation has been developed using the SERPENT code. The goodness of the developed recipe has been checked by careful benchmarking against available data. Based on the result of first task, the analysis for understanding how the observed non-uniformity affects material accountancy in the pyroprocessing system has been conducted. In this stage, the material flow stream for pyroprocess is modeled in detail based on experiment and numerical studies. Then, the uncertainty in determination of the Pu-to-^{244}Cm-ratio associated with non-uniformity of nuclide composition in spent fuel has been quantitatively evaluated. The expectation of Pu MUF and its uncertainty propagated and induced by non-uniformity have been computed. Those achieved parameters are applied to assess material accountability for pyroprocess in a statistical manner. In addition to the analysis for this normal condition, the material accountability for abnormal scenarios given material missing conditions has been performed. For this assessment, we developed the LOPu parameter and evaluated the probability of detection for the LOPu scenarios. The tasks of this study are summarized in Figure 1.

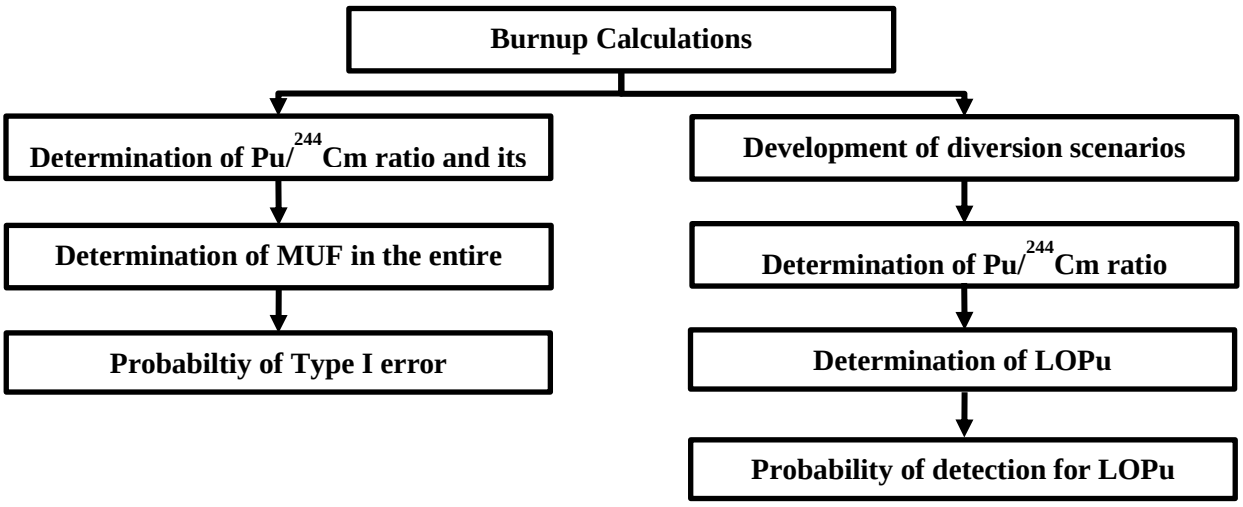

Figure 1 Schematic procedure for evaluation of material accountability in the pyroprocessing system

2.2 High resolution depletion simulations to develop numerical recipes

2.2.1 Unit cell description

In order to develop numerical recipes, depletion simulations at a fuel pin-cell scale are conducted. The physical design parameter of a fuel rod for Optimized Power Reactor (OPR)-1000 is utilized in this study. In the OPR-1000 reactor core, the power and burnup are different, depending on the location of fuel rod and assembly in the reactor core. The number of assemblies loaded in the core as a function of discharged burnup and the initial enrichment is plotted in Figure 2. As the extreme conditions, the lowest (brown color arrow) and 2nd highest (yellow color arrow) burnup conditions are selected based on Zhang [24]. By these two extreme cases, one can determine the ranges of nuclide compositions in spent fuel of OPR-1000. The detail design parameters and burnup conditions are summarized in Table 1, Table 2, and Table 3 [24]. Because sufficient information is not available in open literature, the additional assumptions are applied as follows: 1) the cooling time between cycles is 60 days, 2) the power output (36.91kW/kgU) is constant during the cycles as the specific power of core, and 3) there is no boron in the coolant.

A single fuel rod consists of three parts (Figure 3): upper and lower plenums, and an active fuel region. Because there is a limitation to design a spiral spring in the upper plenum in SERPENT, the solid cylinder tube shape is applied to represent it. The volume of spring is assumed to be 20 % of the total volume of the upper plenum. The composition for the spring is assumed to be stainless steel 302 alloy as shown in Table 4. The empty space of the upper and lower plenums is filled with helium gas. In addition, there are two 50-cm thick of water reflectors above and bottom of the fuel rod. The boundary conditions are ‘black’ at the bases [25], and ‘reflective’ at the lateral faces of the fuel pin-cell.

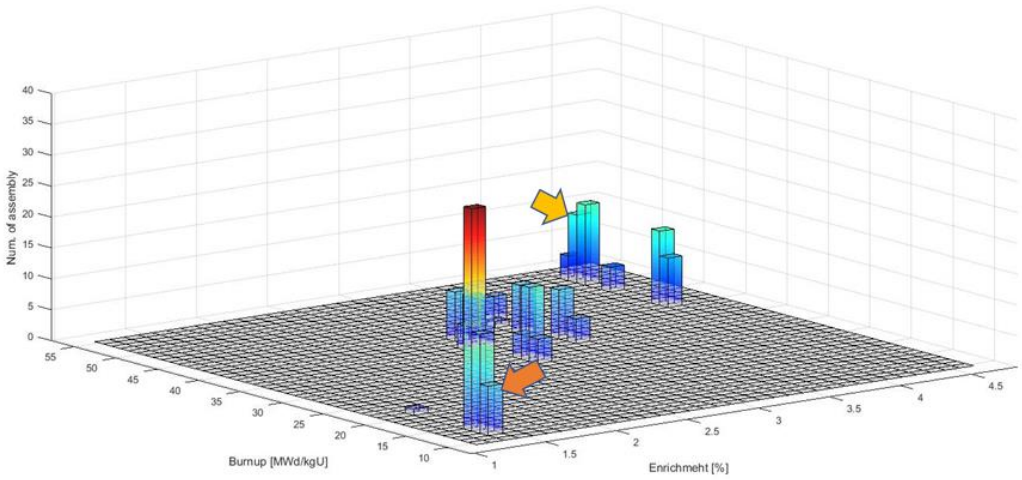

Figure 2 Number of assemblies (z-axis) as a function of burnup (x-axis) and initial enrichment (y-axis).

Table 1 Design parameter for OPR-1000.

Parameters	Value
Thermal power [MW]	2815
Specific power [kW/kgU]	36.91
Inlet temperature [^{o}C]	296.11
Avg. temperature [^{o}C]	312.22
Pellet material	UO_2
Pellet density [g/cm^3]	10.44
Pellet diameter [cm]	0.826
Clad inner diameter [cm]	0.843
Clad outer diameter [cm]	0.970
Cladding	ZIRLO
Active length [cm]	381
Fuel pitch [cm]	1.285
Fuel assembly	16x16

Table 2 Two extreme depletion conditions in OPR-1000.

A004 assembly (low burnup, LBU)	Burnup [MWd/kgU]	Enrichment [%]
1st cycle	11.59	1.42
D009 assembly (high burnup, HBU)	Burnup [MWd/kgU]	Enrichment [%]
1st cycle 2nd cycle 3rd cycle	16.90 34.61 51.24	4.42

Table 3 Mass density of isotopes in a fresh fuel rod for LBU and HBU.

Isotope	Mass density [g/cm^3]	
	LBU	HBU
U-235	3.35E-04	9.90E-04
U-238	2.29E-02	2.23E-02
C-12	9.13E-06	9.13E-06
N-14	1.04E-05	1.04E-05
O-16	4.48E-02	4.48E-02

Table 4 Composition of stainless steel 302 alloy.

Element	Composition
Ni	9.00 [%]
Cr	18.0 [%]
Fe	69.6 [%]
Si	1.00 [%]
C	0.15 [%]
S	0.29 [%]
Mass density	8.03 [g/cm^3]

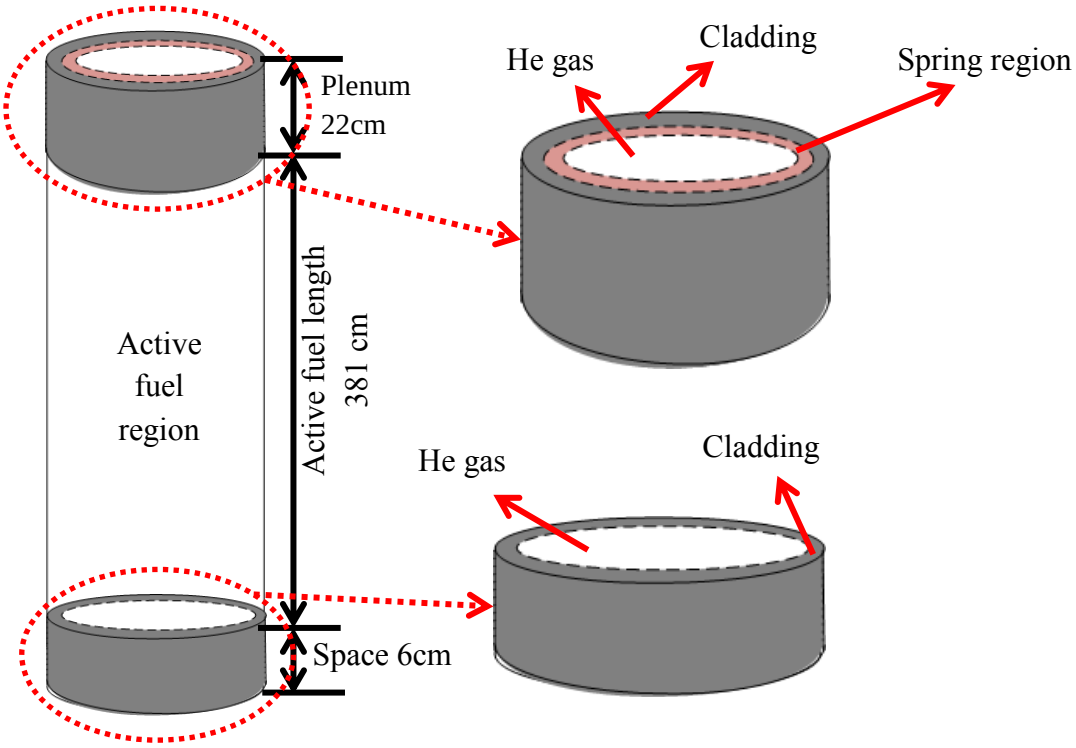

Figure 3 Schematic layout for a fuel rod.

The variation of the moderator density by temperature changes in the axial direction influences on the axial neutron flux distribution; therefore, that should be taken into account for the depletion simulation. The temperature as a function of axial location (z) [26] is formulated by

$$T_{water}(z) = T_{inlet} + \frac{q_0' \tilde{H}}{\pi C_p w}\left[\sin\left(\frac{\pi z}{\tilde{H}}\right) + \sin\left(\frac{\pi H}{2\tilde{H}}\right)\right], \quad (2.1)$$

where $T_{water}(z)$ is the water temperature at the axial location z, T_{inlet} is the inlet water temperature in the reactor core, C_p is the heat capacity of water, w is the water flow rate, H is the length of a fuel, $\tilde{H}$ is the extrapolation length, and $q_0' = \pi r^2 w \Sigma_f \phi_0 J_0(\frac{2.405 r_f}{\tilde{R}})$. The extrapolation length ($\tilde{H}$) is assumed 381.3 [cm] using the thermal cross section data for water [26] as

$$\tilde{H} = H + z_o,$$

$$z_o = 0.7104\lambda_{tr}\,,\ \lambda_{tr} = \frac{1}{\Sigma_{tr}}\,,$$

where λ_{tr} is the transport mean free path and Σ_{tr} is the transport cross section. In fact, the extrapolation length should be evaluated by considering all materials together such as a fuel rod and water, etc. Because it would not dramatically differ from considering only water, the fuel rod is not taken into account to evaluate the extrapolation length. By the assumption of the length of a fuel rod is closed to the extrapolation length ($H \sim \tilde{H}$), the formula is simplified as below

$$if \quad H \sim \tilde{H},\ T_{outlet} - T_{inlet} = \frac{q_0' \tilde{H}}{\pi C_p w} = 32\,, \quad (2.2)$$

which is the temperature difference between inlet and outlet, 32°C [27]. By substituting Eq. (2.2) and the extrapolation length into Eq. (2.1), we can rewrite the formula as

$$T_{water}(z) = T_{inlet} + 32\left[\sin\left(\frac{\pi z}{H}\right) + \sin\left(\frac{\pi}{2}\right)\right]. \quad (2.3)$$

Then, the axial temperature distribution can be evaluated. The water density for every 10 cm of the active fuel rod is evaluated by IAPWS-95 using the evaluated water temperature profile under a constant pressure as 15.5 MPa as shown Figure 4.

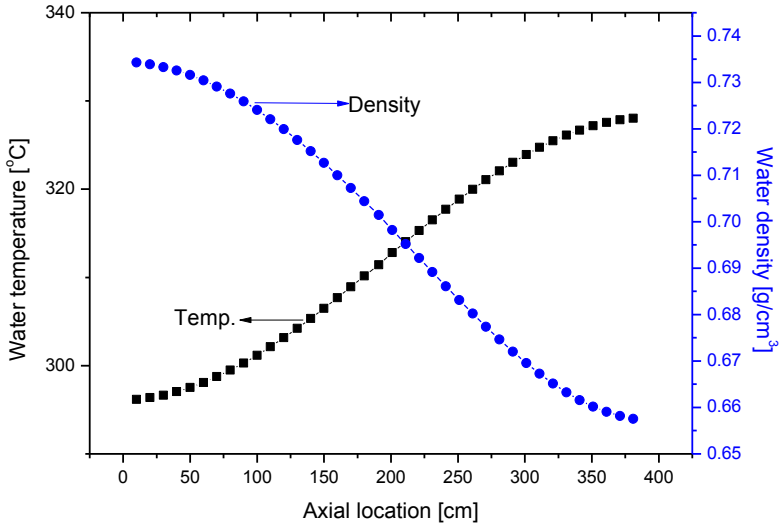

Figure 4 The axial distributions for moderator temperature and density.

2.2.2 SERPENT for a depletion simulation

The depletion simulation is performed with the SERPENT code. SERPENT is a continuous-energy Monte Carlo code that performs both neutron transport and depletion. From the Monte Carlo transport, effective cross sections under desired geometry and nuclide composition are determined. The cross-section data is utilized as input parameter for the depletion simulation. After a set time, the number density of nuclide j has changed. The changed composition is utilized as the input parameter for the Monte Carlo simulation. Then, the cross-section data are newly generated and then the new cross section is substituted into the depletion simulation again as shown in Figure 5. Users control the time intervals for the update of the cross-section data and flux, which is called a burnup step. A short burnup step would be better to get more reliable nuclide composition in spent fuel; however, it requires longer running time. Setting of the appropriate burnup step will be discussed in the next Section.

The neutron population is 150,000. If the statistical uncertainty is greater than 0.1, the number of population will be adjusted. The number of active and inactive cycles is set as 250 and 50, respectively. A predictor-corrector method is applied for depletion. The fission yield, cross section and decay data of ENDF-VII are utilized. The thermal scattering libraries based on JEFF-3.1 at 573.6K.

In order to obtain the axial distribution of nuclide composition for the active fuel rod, 30 meshes are applied as shown in

Table 5. The smaller mesh is applied for the top and bottom of the fuel rod. In contrast, the large mesh is for the middle of the fuel rod, because the non-uniformity of nuclide composition is more significant at the top and bottom of the rod than at the middle. Additional discussion on the axial resolution will provided in the next Section. Based on the descriptions of fuel pin-cell, the side view of geometry for that is shown in Figure 6, as plotted by SERPENT.

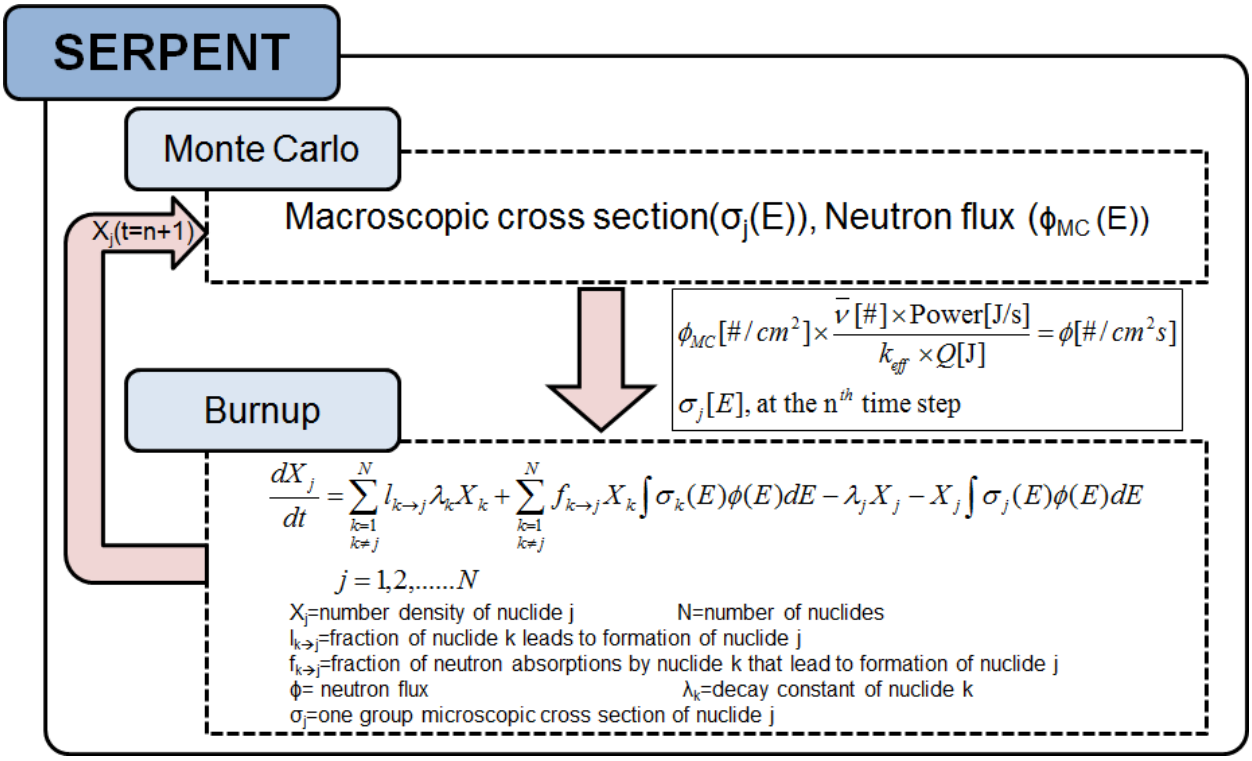

Figure 5 Charts to describe the main structure of SERPENT.

Table 5 Axial mesh configuration for the active fuel rod.

Mesh name	Mesh size [cm]	Accumulated height [cm]
1	1.00	1.00
2	1.00	2.00
3	1.00	3.00
4	1.00	4.00
5	1.00	5.00
6	5.00	10.0
7	5.00	15.0
8	5.00	20.0
9	5.00	25.0
10	5.00	30.0
11	10.0	40.0
12	20.0	60.0
13	30.0	90.0
14	40.0	130
15	60.5	191
16	60.5	251
17	40.0	291
18	30.0	321
19	20.0	341
20	10.0	351
21	5.00	356
22	5.00	361
23	5.00	366
24	5.00	371
25	5.00	376
26	1.00	377
27	1.00	378
28	1.00	379
29	1.00	380
30	1.00	381

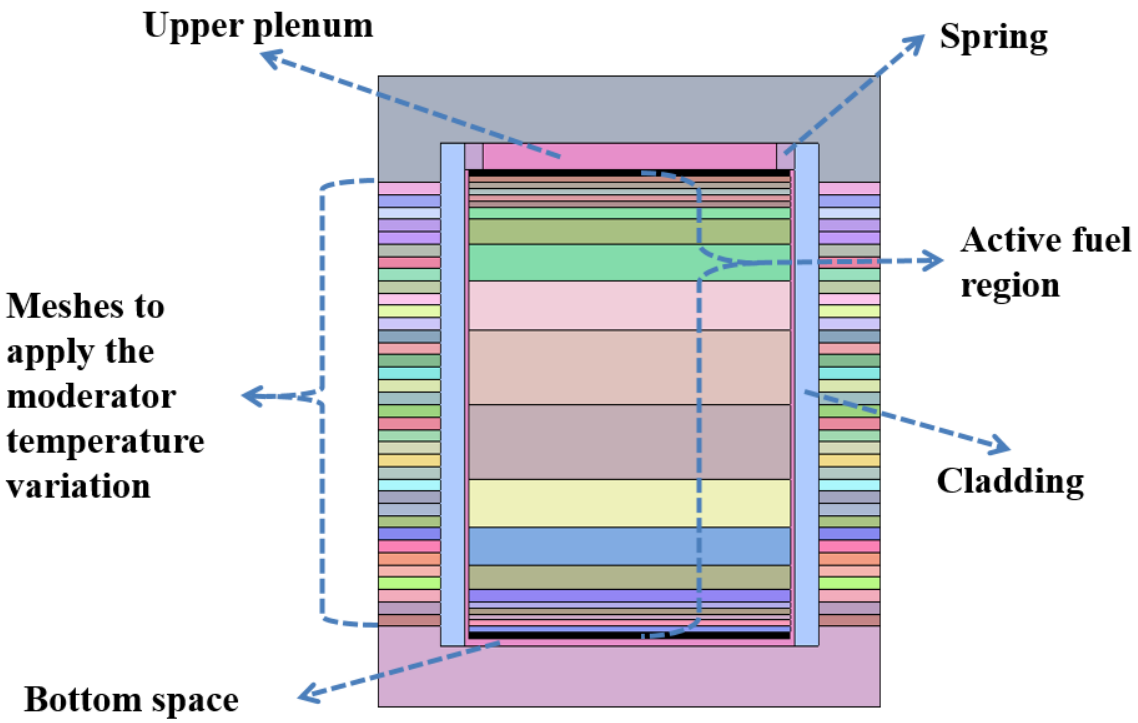

Figure 6 Geometry for the fuel pin-cell plotted by SERPENT.

2.3 Characterization of representative spent fuel assembly

2.3.1 Determination of representative assembly

The previous Section describes the fuel cell, however, it could not be a representative spent fuel, because Zhang's study takes into account only the first five cycles in the OPR-1000 reactor lifetime. The nuclear fuel assembly loading configuration in the reactor core of the Hanbit nuclear power plant, which is also the OPR-1000 type, is describes in Reference [28]. The loading pattern for the quarter of the core shown Figure 7 is for the equilibrium core [28]. The red color box (alphabet: A) is indicating the fresh fuel assembly. The assemblies of the 2nd (alphabet: B) and 3rd (alphabet: C) cycle residence are printed by green and yellow boxes, respectively. The single alphabet-number at the second line of each yellow and green box is indicating where that assembly was located in the previous cycle. Therefore, the shuffling scheme can be recognized by the location information consisting of column and row indicated by the alphabet (A to H) and the number (1 to 7). The red boxes do not contain this information because they are the fresh fuel assemblies. The three different types of assembly are named as Type-0, -1, and -2, respectively. The difference among three types is a number of gadolinia bearing fuel (GBF) rod and its loading pattern in the assembly as shown in Figure 8 and Table 6 [28]. The power from the single assembly is not provided in Reference [28]; therefore, the power per assembly, 15.90 MW, is calculated by the

thermal power of reactor core (2,815 MW) divided by the number of assembly in the core (177 assemblies). The quarter of assembly shows diagonally symmetric structure, therefore, the same lattice, which is the special universes filled with a structure of another universe for SERPENT simulations, number and name is given for fuel rods which are located at the symmetric position. In order to evaluate the number of produced spent fuel assemblies during the entire lifetime (40 years) of the reactor, the capacity factor and the cycle length are assumed as 90% and 18 months. The number of cycles for the 40 years lifetime is 26 as shown in Figure 9. Table 7 shows the information for loading assemblies at each cycle. The loading information for the first five cycles (blue) is referred Zhang's report [24]. From the 6^{th} cycle to the 26^{th} cycle (green), the number of assemblies is evaluated based on the equilibrium core condition shown in Reference [28]. The orange region in Table 7 is evaluated assumptions that the F0 and F1 assemblies are depleted during the 3 cycles and the conservation of total assembly at Cycle-6. Finally, the produced spent fuel assemblies depending on the depletion periods and nuclear fuel assembly type can be expected as shown in Table 8. By a combination of three types of assemblies and three difference depletion periods, nine cases are utilized as the representative spent fuel assembly in this study.

	A	B	C	D	E	F	G	H
1						C, Type-2 E- 4	A, Type-0	C, Type-1 F-4
2				C, Type-1 L-8	A, Type-0	A, Type-2	B, Type-0 G-1	A, Type-1
3			C, Type-0 P-7	A, Type-1	B, Type-1 D-13	B, Type-0 B-11	A, Type-2	B, Type-2 E-11
4		C, Type-1 M-12	A, Type-1	B, Type-1 G-9	B, Type-2 P-10	B, Type-1 L-9	C, Type-1 C-11	C, Type-1 M-10
5		A, Type-0	B, Type-1 N-4	B, Type-2 K-14	A, Type-2	B, Type-2 N-9	A, Type-1	B, Type-1 H-14
6	C, Type-2 D-5	A, Type-2	B, Type-0 L-2	B, Type-1 J-11	B, Type-2 J-13	C, Type-0 J-2	C, Type-0 K-13	A, Type-2
7	A, Type-0	B, Type-0 A-7	A, Type-2	C, Type-1 L-3	A, Type-1	C, Type-0 N-10	A, Type-1	B, Type-2 H-6
8	C, Type-1 D-10	A, Type-1	B, Type-2 L-11	C, Type-1 K-4	B, Type-1 P-8	A, Type-2	B, Type-2 F-8	C, Type-2 F-5

Figure 7 Loading pattern of nuclear fuel assemblies in the equilibrium core

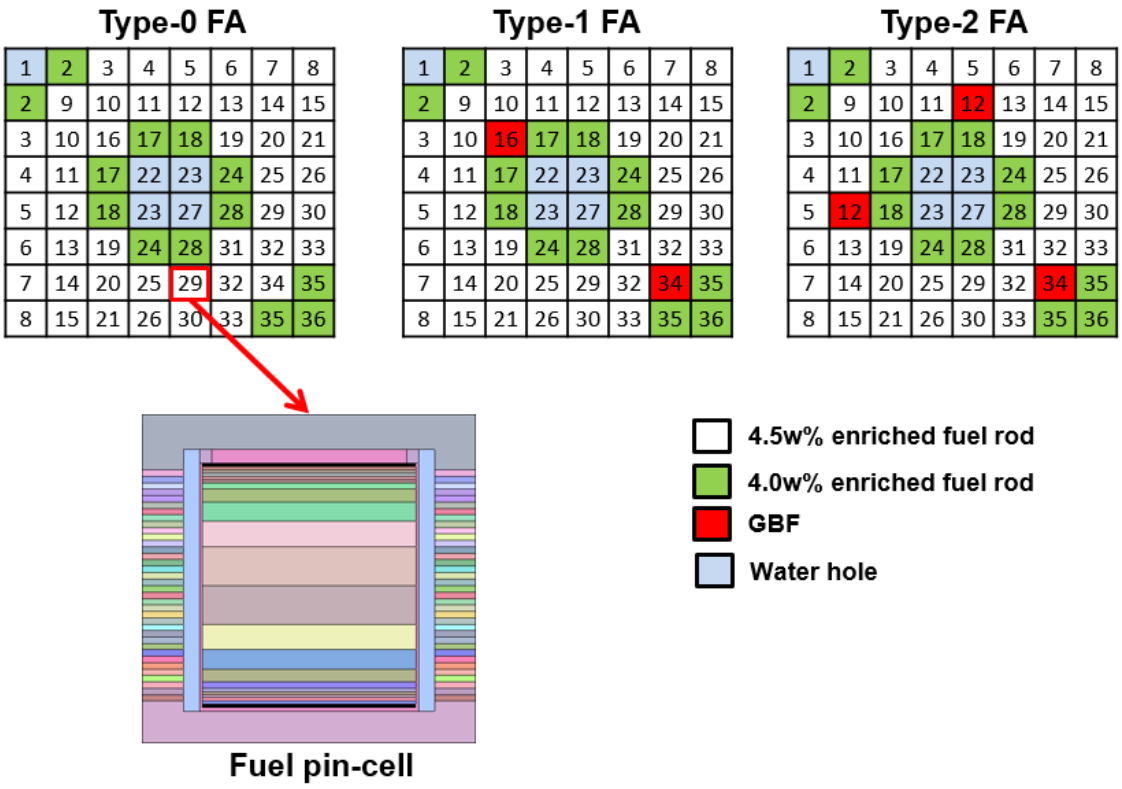

Figure 8 Quarter of Type-0, -1, and -2 fuel assembly (FA).

Table 6 Parameters of nuclear fuel assembly for PLUS-7.

Parameters (PLUS-7)	Value
Pellet density [g/cm^3]	10.41
Pellet diameter [cm]	0.819
Clad inner diameter [cm]	0.837
Clad outer diameter [cm]	0.952
Cladding	ZIRLO
Active length [cm]	381
Fuel pitch [cm]	1.288
Fuel assembly	16X16
GBF	6w% Gd_2O_3
Power [MW/Assembly]	15.90* (evaluated)

Table 7 Number of assemblies at each cycle (blue region from Reference [24], green region from Reference [28], orange region based on assumptions and conservation of number of assemblies in the core).

Type	cycle									
	1	2	3	4	5	6	7	8	9	…
A0	61	1								
B0	24	24	24							
B1	20	20								
B2	16	16	4							
C0	16	16	16							
C1	40	40	9							
D0		28	28	28						
D2		32	32	25						
E0			16	16	16					
E1			24	24	24					
E2			24	24	13					
F0				12	12	12				
F1				20	20	20				
F2				28	28	17				
Type-0					16	16	16			
Type-1					24	24	24			
Type-2					24	24	9			
Type-0						16	16	16		
Type-1						24	24	24		
Type-2						24	24	9		
Type-0							16	16	16	
Type-1							24	24	24	
Type-2							24	24	9	
Type-0								16	16	…
Type-1								24	24	…
Type-2								24	24	…
Type-0									16	…
Type-1									24	…
Type-2									24	…
⋮										⋮

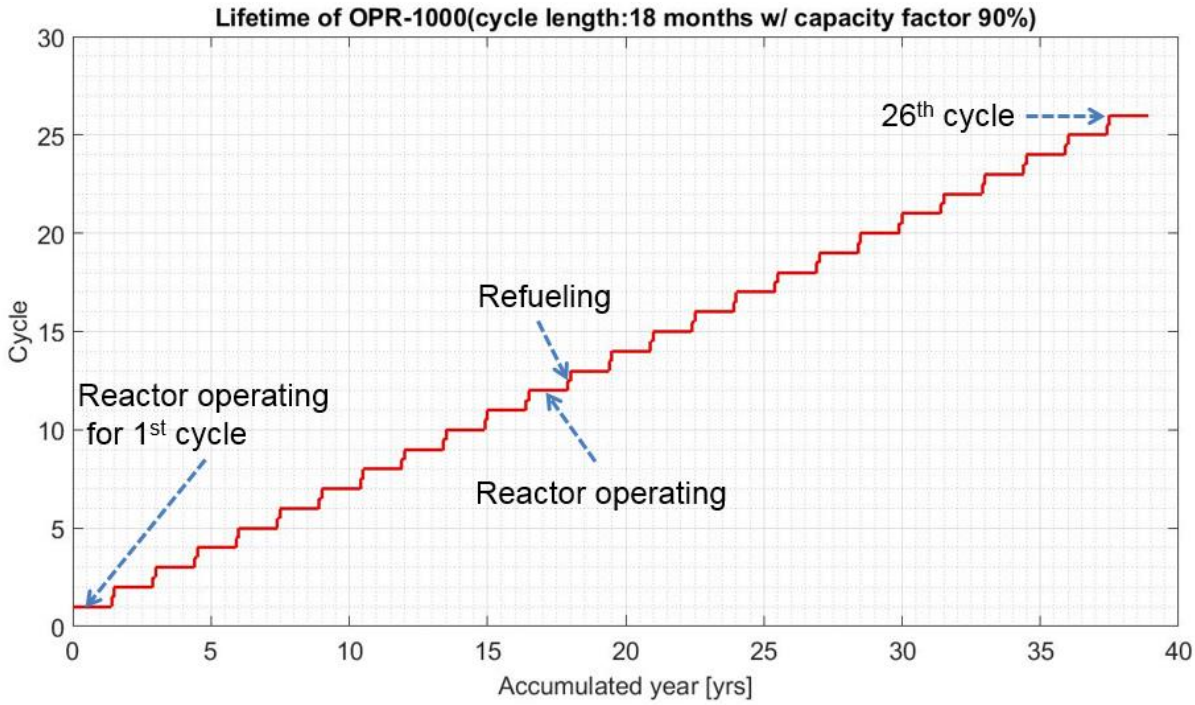

Figure 9 Expectation of operating cycles during the entire lifetime of a nuclear power plant.

Table 8 Expected number of produced spent fuel assemblies during the entire lifetime of OPR-1000 depending on the assembly type and the depletion length.

Assembly type	1 cycle	2cycles	3cycles
Type-0	16	16	320
Type-1	24	24	480
Type-2	24	324	180

2.3.2 Radial and axial non-uniformity

The particle size of powder after the voloxidation process, which is the head-end process in pyroprocess, is around tens to hundreds micrometer [μm], thus, the radial non-uniformity of nuclide composition of fuel pellets could have a strong impact on the material accounting; therefore, the radial non-uniformity in fuel rods should be taken into account for a more realistic simulation of sampling in pyroprocess. However, those simulation conditions mentioned in previous Sections do not take into account the radial distribution of nuclide composition, because simulating fuel rod burnup with sufficient meshes in both the axial and radial direction requires excessive computation time and computer memory. In order to mitigate computational limitations for a large number of domains for each fuel rod in the assembly-scale simulations, the distribution for radial non-uniformity has been decoupled from that for axial non-uniformity. The

normalized and average radial non-uniformity for fuel rods in the assembly has been predetermined depending on the axial location. For these simulations, the fuel rod consists of 10 meshes in the radial direction as shown in Table 9 and 30 meshes in the axial direction, which is equivalent to the axial mesh configuration applying for the assembly scale simulation as shown in

Table 5. The radial distributions of nuclide composition will be determined for each axial mesh and applied proportionally to the results of the assembly scale simulation by matching the results with the axial height of the assembly. In this way, the approximate non-uniformity of nuclide composition in the radial and axial directions can be achieved.

Table 9 Radial mesh configuration.

Radial mesh name	1	2	3	4	5	6	7	8	9	10
Accumulated radius	0.224	0.317	0.330	0.343	0.355	0.366	0.378	0.389	0.399	0.410

As mentioned in the previous Section, there are three different fuel types in the assembly: the low-enriched fuel rod, the normal-enriched fuel rod, and the GBF. In order to achieve the radial distributions for each rod type, the simulation has been conducted independently as shown in Figure 10.

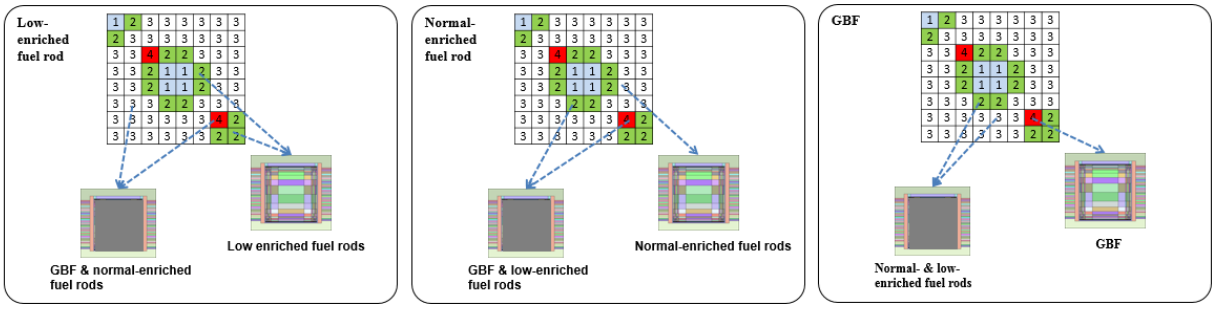

Figure 10 Mesh configurations to obtain the average radial distributions for 3 different rods in the Type-1 fuel assembly.

The normalized mass density for each location in the fuel rod (axial and radial) is evaluated as the mass density of each radial mesh divided by the average mass density of that axial layer of meshes, as shown in Figure 11 and the following equation:

$$\text{Normalized MD}_{i,j} = \frac{\text{MD of i}^{\text{th}}\text{ mesh on j}^{\text{th}}\text{ layer}}{\text{Avg. MD of j}^{\text{th}}\text{ layer meshes}} \quad , \tag{2.4}$$

where MD is mass density, *i* is the i^{th} mesh in the radial direction, and *j* is the j^{th} (layer) mesh in the axial direction. Then, the mass density of each axial mesh from the simulations based on Figure 8 is substituted into the below equation in order to produce the radial distribution of nuclide composition of each axial mesh

$$\text{MD}_{i,j} = \text{Normalized MD}_{i,j}^{\text{fuel pin sim}} \times \text{MD}_{j}^{\text{assembly sim}} \quad , \tag{2.5}$$

where "fuel pin sim" and "assembly sim" are the results from one fuel pin and one assembly simulation, respectively.

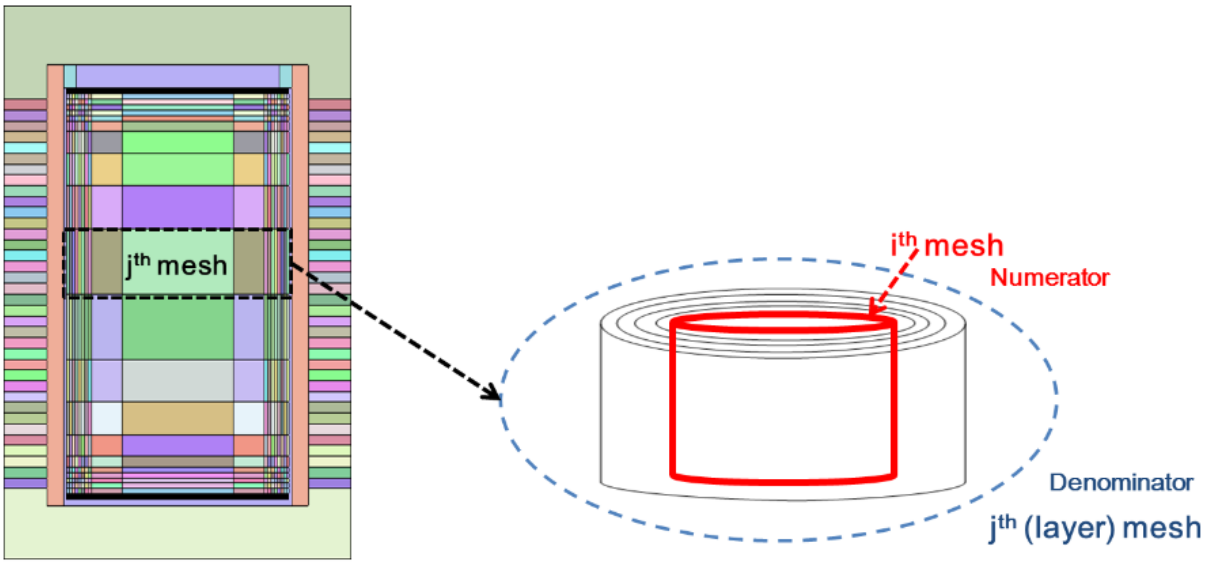

Figure 11Evaluation of normalized radial mass density at each axial location.

The total number of discrete meshes is 30 in the axial direction and 10 in the radial direction, for a total of 236 fuel rods. Different radial and axial mesh sizes are applied for the depletion simulations as shown in Figure 8 and Figure 10; therefore, the volumes of each mesh are different. To account for the fact that some meshes are larger than others, the Serpent simulation result is rearranged into 381 and 20 equally sized segments for the axial and radial directions, respectively, for each fuel rod. The larger meshes are split into smaller meshes of uniform nuclide composition. Finally, the nuclide composition data is rearranged in a 381(axial)-by-20(radial)-by-236(fuel rods) matrix form.

2.4 Descriptions of the processes in the head-end process to develop mass flow diagram and probability distributions of the ratio after each process

2.4.1 Chopping process

A spent fuel assembly, which is generally around 3 to 4 m in length, could not be an appropriate form as a feed material for the pyroprocessing. It should be disassembled and pre-treated to enhance efficiencies in the system. To begin with, the disassembling and chopping is assigned. The length of chopping has not been decided, however, the literature has mentioned a potential and conceptual length. The one to two inches [in] in length of chopped pieces is introduced in Williamson's paper [6]. A IAEA report mentions that the sheared fuel sections are generally 3 to 5 cm in length [7]. In order to calculate the necessary reactor size for decladding and voloxidation process, the length of piece considered is 3, 5, 7, and 10 cm [29]. The length of UO_2 pellets as a

feed material for voloxidation experiments are 1.5 cm [30] and 1.01 cm [8]. In this study, the 1cm long chopped piece, which is generally close to the length of one pellet, is assumed, because not only the latest publication considers 1.01cm in length [8], but also the smaller length of piece would increase the non-uniformity of nuclide composition distribution in the products. By that, the total generated chopped pieces for one assembly is 89,916.

The 89,916 pieces have individual mass densities for Pu and ^{244}Cm, and the Pu-to-^{244}Cm-ratio values. The expected probability distribution of Pu and ^{244}Cm mass densities in samples are generated by the random sampling method. The various sample sizes have been applied, for example, 5, 10, 20, 30, and 40 chopped pieces. In order to be consistent, the total number of sampled pieces for the entire sampling realization, the number of trials for 5, 10, 20, 30, and 40 sample size cases are 240,000, 120,000, 60,000, 40,000, and 30,000, respectively. The normality of the obtained distributions is tested by the Quantile-Quantile (Q-Q) plot as a graphical manner and Jarque-Bera (JB) test as a statistical manner.

Q-Q plots have been utilized to visually confirm that two random variables have same distribution [31]. The quantile is the value that corresponds to a specified proportion of a sample or population [32]. The quantiles of two random variables are plotted in the x- and y-axis, respectively. If the two random variables are from the same distribution, the linear line could be observed. In order to test the normality of obtained data, the quantile for that (y-axis) is plotted against the quantile for the data from the standard normal distribution (x-axis).

The JB test has been developed to statistically test the normality of distributions [33,34]. The equation for this method consists of two parameters, skewness and kurtosis as shown below,

$$JB = \frac{N}{6}\left[\hat{\beta}_1^2 + \frac{\left(\hat{\beta}_2 - 3\right)^2}{4}\right] \overset{approx}{\sim} \chi_2^2 ,$$

$$\hat{\beta}_1 = \frac{\frac{1}{n}\sum_{i=1}^{n}\left(x_i - \bar{x}\right)^3}{\left(\frac{1}{n}\sum_{i=1}^{n}\left(x_i - \bar{x}\right)^2\right)^{3/2}} \ , \hat{\beta}_2 = \frac{\frac{1}{n}\sum_{i=1}^{n}\left(x_i - \bar{x}\right)^4}{\left(\frac{1}{n}\sum_{i=1}^{n}\left(x_i - \bar{x}\right)^2\right)^{2}}, \tag{2.6}$$

where $\widehat{\beta_1}$: the skewness, $\widehat{\beta_2}$ is the kurtosis and N is the sample size. It is pursued that the JB value by Eq. (2.6) is approximately following the χ^2-distribution with two degrees of freedom. Then, that evaluated JB value is tested by the χ^2-test. If the JB value is greater than the significance point shown in Table 10, the normality could be rejected with that significance level.

Table 10 Significance values for the JB normality test [34].

Sample size	Significance level	
	α=0.10	α=0.05
20	2.13	3.26
30	2.49	3.71
40	2.70	3.99
50	2.90	4.26
75	3.09	4.27
100	3.14	4.29
125	3.31	4.34
150	3.43	4.39
200	3.48	4.43
250	3.54	4.51
300	3.68	4.60
400	3.76	4.74
500	3.91	4.82
800	4.32	5.46
∞	4.61	5.99

2.4.2 Decladding and voloxidation process

The comparison between a mechanical and oxidative decladding is concluded that the oxidative decladding is able to enhance the efficiency of decladding and electrolytic reduction [2]. The main purposes of voloxidation are 1) releasing and reducing volatile and semi-volatile fission products in spent fuel, and 2) the oxidation of pellets to convert UO_2 to U_3O_8 [35]. The oxygen diffuses through grains in UO_2 pellets. During the oxidation reaction with UO_2, the volume of feed material increases as the grains are expand. Then, UO_2 is converted into the powder type U_3O_8 [35]. KAERI has been developing the process performing decladding and voloxidation together [8–10,29,30,36,37]. According to Kim's paper [30], the powder particles generally ranges in size from 3 to 120 μm at 500°C. However, it varies depending on the operating temperature. The mean and variance of particle size distribution under the higher operating temperature are generally greater than that in lower temperature conditions.

In order to generate the probability of concentration in particles size after voloxidation, the mass density distributions of Pu and ^{244}Cm for each fuel rod are combined with the radial distributions of those by matching the axial location of the two distributions as mentioned in the section 2.3.2. Although non-uniformity exists within each segment as shown in Figure 11, it is assumed that powders are uniform, if they are from the same segment. By this assumption, we could achieve the approximate distributions for nuclide composition after the voloxidation process.

2.4.3 Granulation

The homogenization process of powder was planned prior to the electrolytic reduction process [13,38,39]. Even though the electrolytic reduction with a feed material U_3O_8 powder is efficient, it has difficulty to handle the fine powder and requires a well-designed cathode basket [2,40,41]. Therefore, the pretreatment such as granulation [9,11] or porous pellet manufacturing process [8,10] has been suggested. In this study, the granulation process has been considered.

As mentioned above, the one granule consists of multiple powder particles. The sizes of single powder and granule are in the μm and mm scale, therefore, a number of sampled powder particle to be one granule is around hundreds to thousands. If we take a sample after the granule process, that number of powder particles in one granule could be utilized to determine the sample size. Based on this concept, the sampling scheme from the depletion simulation results for fuel rods to granulation is shown in Figure 12.

For this sampling strategy, the central limit theorem can be applied for the statistical analysis of nuclide concentration distributions by the law of large number. Let X_1, X_2, …, X_n be the random variables which come from an independent and identical distribution. Each random variable has the mean (μ) and variance (σ^2) values. If n is large, the distribution of $X_1+X_2+\ldots+X_n$ is approximately following the normal distribution with μ (mean) and σ^2/n (variance), respectively [42]. Therefore, the sample mean and variance can be evaluated by below equations

$$\begin{aligned}\text{Sample mean}: \mathrm{Exp}[\overline{X}] &= \mathrm{E}\left[\frac{\mathrm{X_1}+\mathrm{X_2}+\ldots+\mathrm{X_n}}{\mathrm{n}}\right] = \frac{1}{n}\left(\mathrm{Exp}[\mathrm{X_1}]+\mathrm{Exp}[\mathrm{X_2}]+\ldots+\mathrm{Exp}[\mathrm{X_n}]\right) = \mu, \\ \text{Sample variance}: \mathrm{Var}[\overline{X}] &= \mathrm{Var}\left[\frac{\mathrm{X_1}+\mathrm{X_2}+\ldots+\mathrm{X_n}}{\mathrm{n}}\right] = \frac{1}{n^2}\left(\mathrm{Var}[\mathrm{X_1}]+\mathrm{Var}[\mathrm{X_2}]+\ldots+\mathrm{Var}[\mathrm{X_n}]\right) = \frac{\sigma^2}{n}.\end{aligned} \tag{2.7}$$

The statistical results for concentration distributions after the granulation process are evaluated by applying this central limit theorem properties.

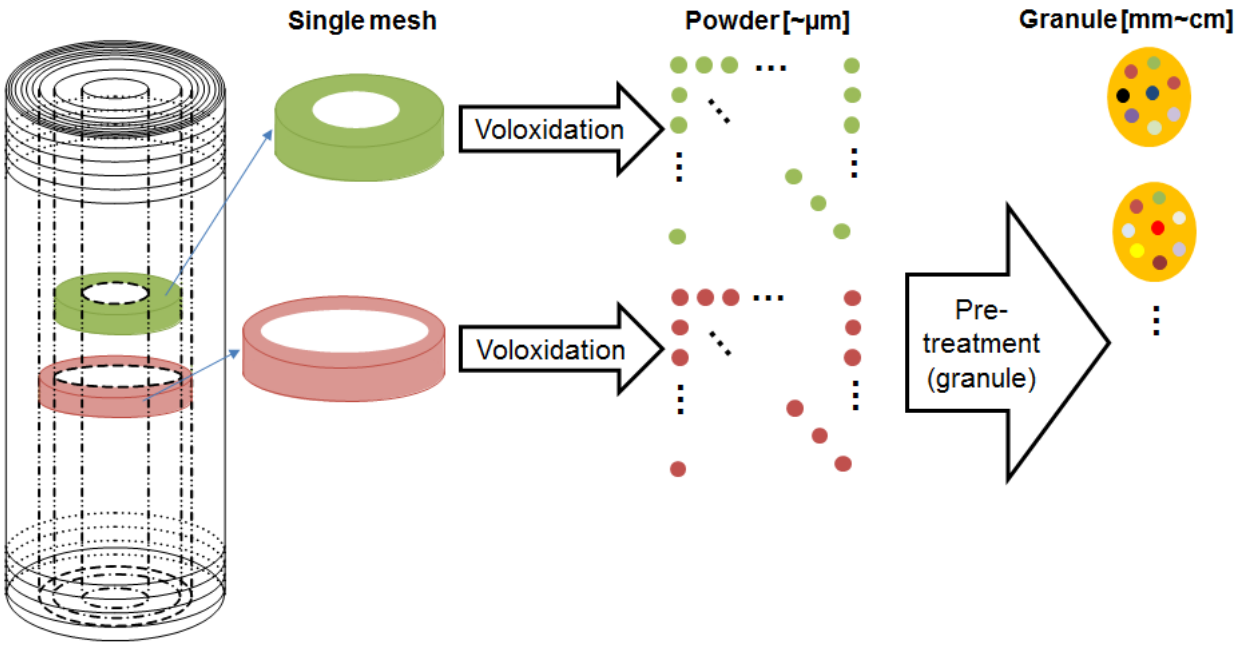

Figure 12 Sampling scheme of a granule using the SERPENT simulation results.

The Pu and ^{244}Cm concentrations could be independently measured using the granule sample, therefore, the those measured values can be defined as the independent random variables. As mentioned above, a sample size for powders in the sampled granule is large enough to apply the law of large number. It is rationally assumed the two random variables, the measured data for Pu and ^{244}Cm concentration, follow the normal distribution. Therefore, the Pu-to-^{244}Cm-ratio consisting of the ratio of two normally distributed random variables is following the Cauchy distribution for which the mean and variance cannot be computed. The Cauchy distribution could be approximately transformed to the normal distribution, for example, the Geary-Hinkley (GH) transformation [43]. The governing equation of the method for R=X/Y and ρ=0 is

$$R^2\left(\mu_X^{\,2}-z^2\sigma_X^{\,2}\right)-2R\left(\mu_X\mu_Y\right)+\left(\mu_Y^{\,2}-z^2\sigma_Y^{\,2}\right)=0, \tag{2.8}$$

where R, X, and Y are random variables, ρ is the correlation coefficient, μ_I and σ_I are the mean and standard deviation of random variable, I. The criteria to apply this transformation method is i) the coefficient of variance X is greater than 0.005 and ii) the coefficient of variance Y is less than 0.39. By solving the quadratic Eq. (2.8) with respect to R, the average of two solutions represents the mean of R and the summation of two values divide by z is the standard deviation of R with a certain confidence interval, for example, if z is 1.96, the 95% probability interval would be applied.

2.5 Hypothesis testing

To begin with, let us define the well closed system that contains receives and shipments of the nuclear material at a given time t_0 and t_1. The closed system can be named as the MBA (Material Balance Area) [44]. The MBA is the nuclear material accounting area for reporting to the IAEA.

The book inventory (B) is able to be defined as the summation of the initial physical inventory (I_0) which is the amount of contained material in the closed system at time t_0 and the throughput (D) which is the receipt (R) minus the shipment (Sh). The amount of contained material in the closed system at time t_1 is the physical inventory (I_1). Using all terms defined above, we can formulate for the MUF as below

$$\mathrm{MUF} = \mathrm{B} - \mathrm{I}_1 = \mathrm{I}_0 + \mathrm{D} - \mathrm{I}_1 = \mathrm{I}_0 + \mathrm{R} - \mathrm{Sh} - \mathrm{I}_1. \tag{2.9}$$

However, in the pyroprocessing system, the feed materials are treated in the batch, then the product and waste are transferred to other processes. In other words, the physical inventories at time t_0 and t_1 would be ignored. The MUF can be redefined as

$$\mathrm{MUF} = \mathrm{R} - \mathrm{Sh}. \tag{2.10}$$

The MUF should be zero; however, the MUF is normally expected non-zero due to measurement errors, the natural phenomenon such as the spread out of materials into the atmosphere and remainders in a basket or a batch containing nuclear materials. Each term is assumed as random variables and those are following normal distribution. The R and Sh can be represented in the following forms:

$$\begin{aligned} \mathrm{R} &\sim N\left(\mu_R, \sigma_R^2\right), \\ \mathrm{S} &\sim N\left(\mu_{Sh}, \sigma_{Sh}^2\right), \end{aligned} \tag{2.11}$$

where μ_R and μ_{Sh} are the mean of R and S, and σ_R and σ_X are the standard deviations of R and Sh. The σ_R and σ_{Sh} are the uncertainty associated with the non-uniformity of nuclide composition in this study. The standard deviation (σ_{MUF}) and mean (μ_{MUF}) of MUF can be calculated by the properties of variance and mean as shown below

$$\begin{aligned} \mu_{\mathrm{MUF}} &= \mu_R + \mu_{Sh}, \\ \sigma_{\mathrm{MUF}} &= \sqrt{\sigma_R^2 + \sigma_{Sh}^2}. \end{aligned} \tag{2.12}$$

In order to apply the hypothesis testing method, the null and alternative hypothesis should be defined so that if one hypothesis is true, the other is false. The null hypothesis (H_0) and the alternative hypothesis (H_a) are defined as

$$\begin{aligned} \mathrm{H}_0 &: \mu_{\mathrm{MUF}} = 0, \\ \mathrm{H}_\mathrm{a} &: \mu_{\mathrm{MUF}} = M, (M > 0). \end{aligned} \tag{2.13}$$

The M value is referred the Significant Quantity (SQ, i.e. SQ of Pu = 8 kg) recommended by IAEA [14]. The Type-I and -II errors can be explained as following. The definition of Type-I error is 'Incorrectly rejecting a true null hypothesis' and Type-II error is 'Incorrectly rejecting a true alternative hypothesis'[42]. For example, even though the real expected value of MUF is zero,

which means the null hypothesis is true, the measurement can show the expected value of MUF is not zero, which means the diversion or missing of material happens. This is called the Type-I error. In contrast, the Type-II error is the diversion or missing happens, but the measurement instrument indicates there is no missing and diversion of material. Table 11 is able to help to understand the Type-I and -II errors.

Table 11 Type-I and -II errors

	H_0 True	H_a True
Accept H_0	Correct decision (true positive)	Type-II error (false negative)
Accept H_a	Type-I error (false positive)	Correct decision (true negative)

For the mathematical expression for Type-I and -II errors, we need one more parameter, the significant threshold value (S). The probability of Type-I (α) and -II (β) errors are formulated as

$$\begin{aligned} \alpha &= \mathrm{Prob}\left\{\mathrm{MUF} > \mathrm{S} \middle| \mathrm{H}_0\right\}, \\ \beta &= \mathrm{Prob}\left\{\mathrm{MUF} \le \mathrm{S} \middle| \mathrm{H}_a\right\}. \end{aligned} \tag{2.14}$$

We can represent the cumulative density function (Φ) to represent the probability of Type-I and -II errors as

$$\begin{aligned} \alpha &= \mathrm{Prob}\left\{\frac{\mathrm{MUF}}{\sigma_{\mathrm{MUF}}} > \frac{\mathrm{S}}{\sigma_{\mathrm{MUF}}} \middle| \mathrm{H}_0\right\} = \Phi\left\{\frac{\mathrm{S}}{\sigma_{\mathrm{MUF}}}\right\}, \\ \beta &= \mathrm{Prob}\left\{\frac{\mathrm{MUF-M}}{\sigma_{\mathrm{MUF}}} \le \frac{\mathrm{S-M}}{\sigma_{\mathrm{MUF}}} \middle| \mathrm{H}_a\right\} = \Phi\left\{\frac{\mathrm{S-M}}{\sigma_{\mathrm{MUF}}}\right\}. \end{aligned} \tag{2.15}$$

In addition, the probability of two errors can be graphically explained as shown in Figure 13. The arrow dot lines are indicating the interval of integration. The black plotting line is for the null hypothesis (H_0), whereas the red plotting line is for the alternative hypothesis (H_a). The probability of Type-I error (α) and detection (1-β) will be utilized as a performance metric to assess safeguardability and material accountability for pyroprocess in this study.

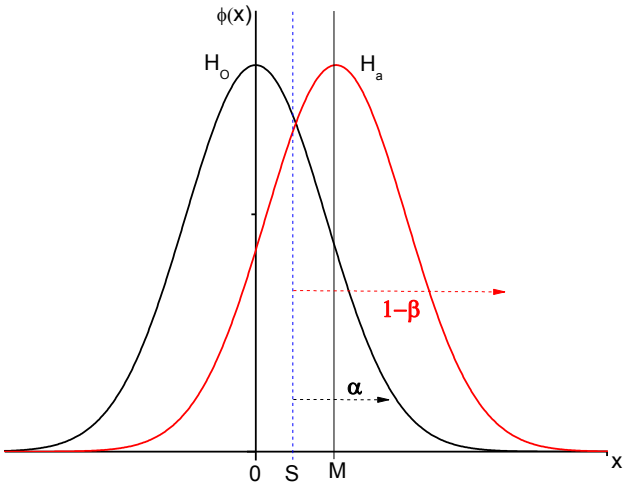

Figure 13 Probability of Type-I (α) and -II (β) errors.

Chapter 3

Results

3.1 Development of numerical recipes for high resolution depletion simulations of a PWR fuel rod by SERPENT

3.1.1 Input data for sensitivity study to modeling assumptions

3.1.1.1 Xe equilibrium calculation and burnup step

Spatial power oscillations can be caused by xenon (Xe) oscillations, because Xe is a strong neutron absorber. According to the DOE handbook [45], the mechanism of Xe oscillation is introduced by following four steps;

(1) An initial lack of symmetry in the core power distribution, for example, individual control rod movement or misalignment, causes an imbalance in fission rates within the reactor core, in the iodine-135 (^{135}I) buildup and the ^{135}Xe absorption.

(2) In the high-flux region, ^{135}Xe burnout allows the flux to increase further, whereas in the low-flux region, the increase in ^{135}Xe causes a further reduction in flux. The ^{135}I concentration increases where the flux is high and decreases where the flux is low.

(3) As soon as the ^{135}I levels build up sufficiently, decay to Xe reverses the initial situation. Flux decreases in this area, and the former low-flux region increases in power.

(4) Repetition of these patterns can lead to Xe oscillations moving about the core with periods on the order of about 15 hours.

The oscillations of overall power can influence on local powers by a factor of three or more. In order to prevent Xe oscillations, SERPENT calculates ^{135}I and ^{135}Xe concentrations using flux and cross-section tallied during that cycle using below equations

$$\begin{aligned} \mathrm{N}_{\mathrm{I-135}} &= \frac{\gamma_{\mathrm{I-135}}\Sigma_{\mathrm{f}}\phi}{\lambda_{\mathrm{I-135}}}, \\ \mathrm{N}_{\mathrm{Xe-135}} &= \frac{\gamma_{\mathrm{Xe-135}}\Sigma_{\mathrm{f}}\phi}{\lambda_{\mathrm{Xe-135}} + \sigma^{\mathrm{cap}}_{\mathrm{Xe-135}}\phi}, \end{aligned} \tag{3.1}$$

where N_i is the concentration of isotope i, γ_i is the cumulative fission yield of isotope i, Σ_f^{tot} is the macroscopic total fission cross-section of the material, λ_i is the decay constant of isotope i, σ^{cap}_{Xe-135} is the microscopic capture cross-section of ^{135}Xe, ϕ is the neutron flux [46]. The assumption of this

method is ^{135}Xe and its precursors are in a secular equilibrium. These newly calculated concentrations are used during for the next cycle.

As mentioned above, the burnup step to update of nuclear data, flux, and nuclide composition would alter the final nuclide composition in spent fuel. Therefore, by different combinations of burnup steps, long and short burnup steps shown in Table 12, and an option for applying Xe equilibrium calculation, four cases are considered as below,

- Case 1: the long burnup step & not applying Xe equilibrium calculation,
- Case 2: the long burnup step & applying Xe equilibrium calculation,
- Case 3: the short burnup step & not applying Xe equilibrium calculation,
- Case 4: the short burnup step & applying Xe equilibrium calculation.

In order to further discuss the impact of the length of burnup step, one more simulation with shorter burnup step, 10 days, has been conducted. In detail, the burn steps 1 to 4 of additional simulation case are equal to the current short burnup step case shown in Table 12. However, after the step 4, the gap between steps is set as 10 days. The total number of steps for this case is 34. The simulation results with the 25-day and 10-day burnup steps are compared.

3.1.1.2 Axial resolution

SERPENT generates an average nuclide concentration for each domain, which is called a mesh in this study. The 30 meshes configuration for the active fuel rod shown in

Table 5 is arbitrary decided for the depletion simulation. Intuitively, the simulation result with more mesh number for the region is able to provide more detail and reliable axial distribution for nuclide concentrations; however, there is a limitation of mesh number to execute the code due to a computer memory. Therefore, a good enough axial resolution should be discussed. For that, the simulation result conducted with 381 meshes for the active fuel region is compared with that with 30 meshes.

Table 12 Burnup steps.

Long burnup step		Step	Short burnup step	
Day	Burnup [MWd/kgU]		Day	Burnup [MWd/kgU]
1.00	0.04	1	1.00	0.04
3.00	0.11	2	3.00	0.11
5.00	0.18	3	5.00	0.18
10.0	0.37	4	10.0	0.37
50.0	1.85	5	50.0	1.85
100	3.69	6	75.0	2.77
200	7.38	7	100	3.69
314	11.6	8	125	4.61
		9	150	5.54
		10	175	6.46
		11	200	7.38
		12	225	8.30
		13	250	9.23
		14	275	10.2
		15	314	11.6

3.1.1.2 Effect of axial water temperature change with respect to time

The axial water temperature distribution evaluated by Eq. (2.1) is assumed to be constant during the entire burnup steps. In real situations, the temperature has continuously changed as a function of time. Therefore, the effect of water temperature change as a function of burnup on evaluation of nuclide composition in spent fuel will be discussed. For that, after each single burnup step, the depletion simulation has been intentionally stopped to evaluate the new axial water temperature distribution for the next burnup step based on the assumption of all heat from the fuel is transfered into water. The power for each mesh is obtained from the burnup [MWd/kgU] times the initial mass of uranium [kgU] divided by the depletion time [day]. The energy conservation between the generated power of the fuel rod from bottom to n^{th} mesh and power contained in water from bottom to n^{th} mesh height is formulated as

$$\sum_{i=1}^{n} \mathrm{P}(\mathrm{Mesh\_i}) = C_p w(\mathrm{T}_{\mathrm{water}}(\mathrm{Mesh\_i}) - \mathrm{T}_{\mathrm{inlet}}), \tag{3.2}$$

where P is the generated power at the mesh_i location [kW], C_p is the specific heat capacity of water [kJ/kg^{o}C], w is the mass flow rate [kg/s], T_{water} is the water temperature at the mesh_i location [^{o}C], T_{inlet} is inlet water temperature (296^{o}C). Finally, the water temperature can be calculated by

$$\mathrm{T}_{\mathrm{water}}(\mathrm{Mesh\_i}) = \frac{\sum_{i=1}^{n} \mathrm{P}(\mathrm{Mesh\_i})}{c_p w} + \mathrm{T}_{\mathrm{inlet}}. \tag{3.3}$$

Let us assume appropriate values for the specific heat capacity and the mass flow rate. The specific heat capacity is assumed to be 5.458 kJ/kg at 15.5 MPa and 300^{o}C. The mass flow is assumed 0.393 kg/s. However, it is not sure this assumption is made under a consistent condition with the case that the water temperature is assumed to be fixed. In order to give the consistent condition between the fixed and updated water temperature cases, the term in Eq. (2.1) should be kept as 32 as shown in Eq. (2.3). By this approach, the peaking factor should be assumed as 1.55, because q'_0 can be defined by the maximum linear power referred by Nuclear System [47]. The peaking factor is not going to be utilized in the modified equation which is taking into account the approximation shown in Eq. (2.3), however, it is able to support to generate the axial water distribution for the 1st burnup step. Then, Eq. (3.3) is applied to evaluate it for the rest of all burnup steps as shown the flow chart in Figure 14 .

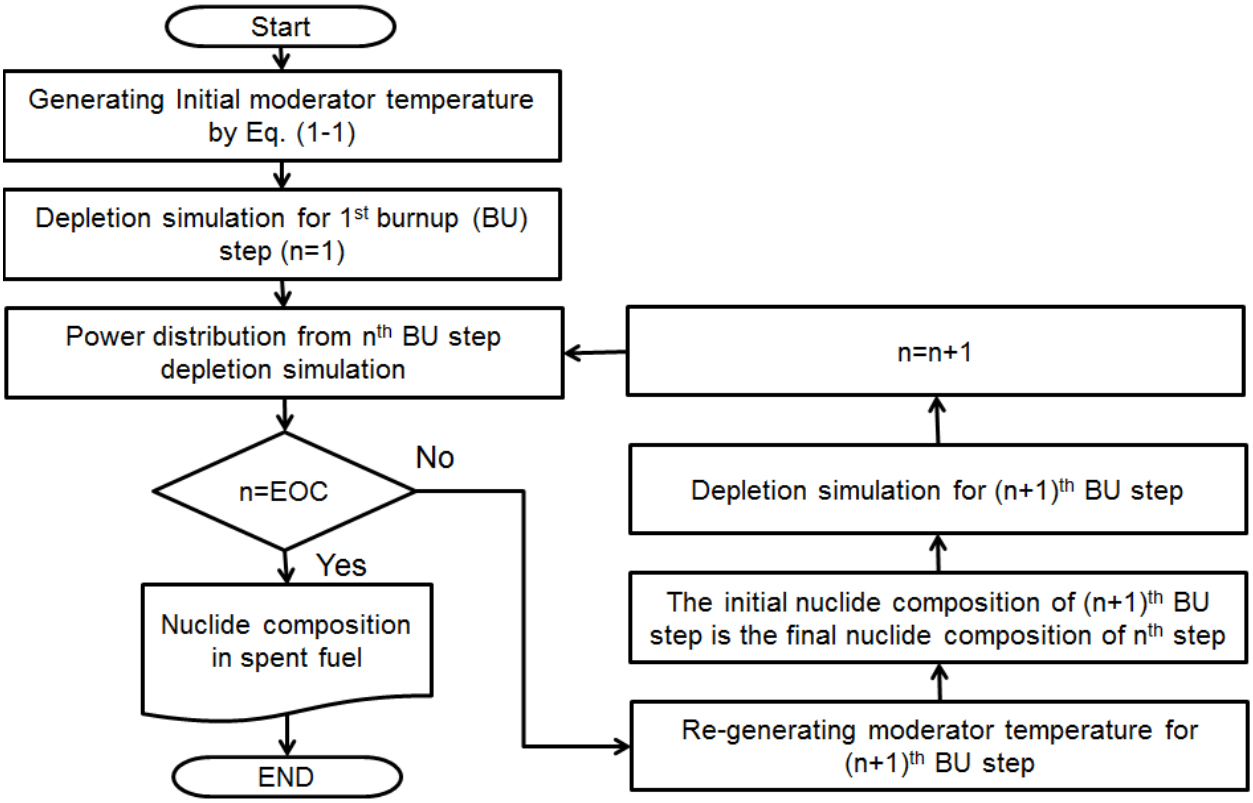

Figure 14 The flow chart to evaluate the effect of water temperature change as a function of burnup step (EOC: end of cycle).

3.1.2 Results for sensitivity study

3.1.2.1 Xe equilibrium calculation and burnup steps

The axial distribution of neutron flux [#/cm^{2}sec] and ^{239}Pu atom density [#/cm^3] for four cases mentioned in Section 3.1.1.1 at different burnup steps for the LBU fuel pin-cell are plotted in Figure 15 and Figure 16. The thick blue and red lines in each figure indicate the axial distribution at the beginning and end of cycle, respectively. The axial flux distributions for the beginning of cycle (thick blue) for four cases are like a cosine shape. However, the flux shapes at the end of cycle among four cases turn out differently. The axial peak of flux for the cases 1, 2, and 3 are located near 20% height from the bottom of the fuel rod, whereas case 4 shows nearly flat for the middle fuel rod and the peak at 80% height. The ^{239}Pu atom density distribution as a function of axial location at the end of cycle for the four cases (thick red) shows that the peaking of that is located around 80% height. The axial flux distribution in case 4 is only consistent with the axial ^{239}Pu concentration distribution. Therefore, it would be said that the more reliable nuclide

composition distribution in the axial direction for the fuel rod can be achieved by taking into account the Xe equilibrium calculation and short burnup steps.

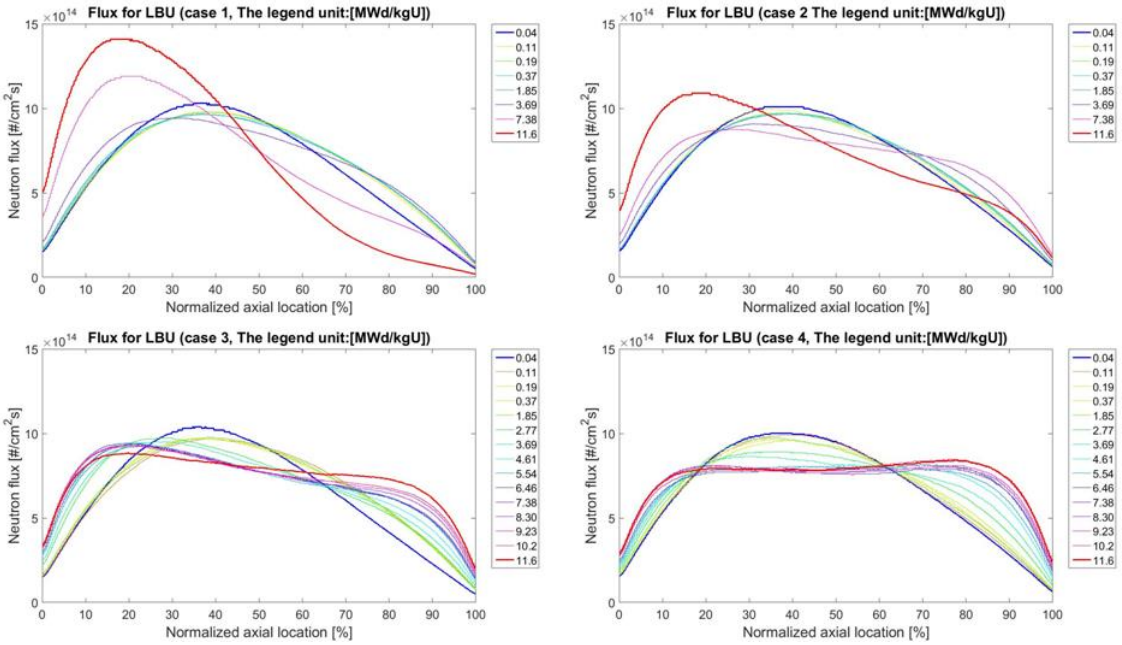

Figure 15 Axial flux distributions at each burnup step for the LBU fuel rod (case1: left top, case2: right top, case3: left bottom, case4: right bottom).

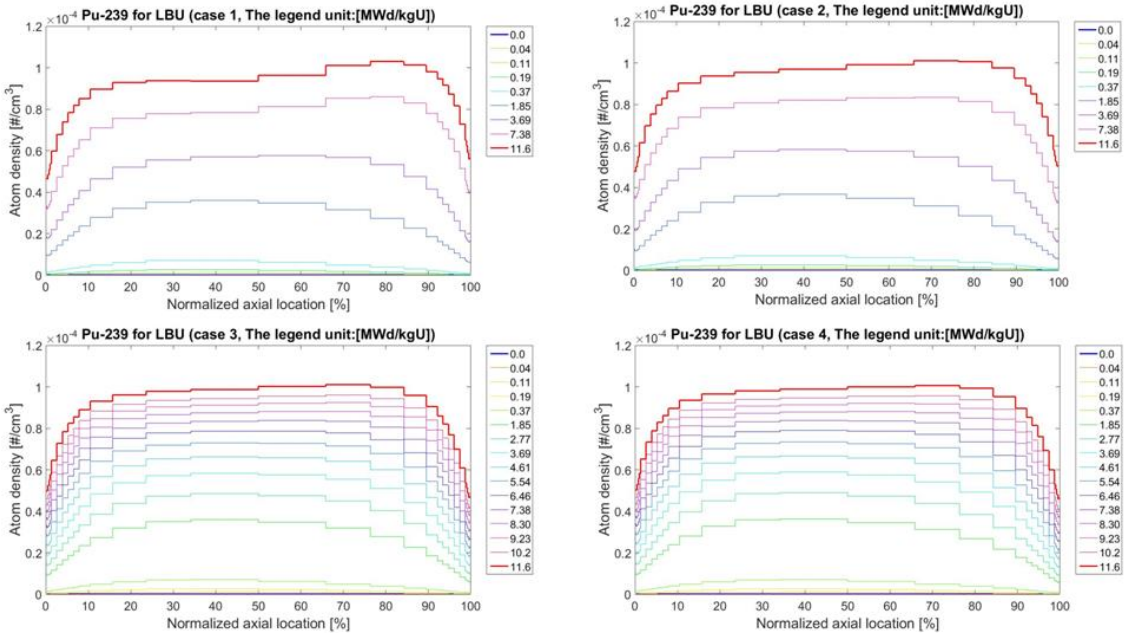

Figure 16 Axial ^{239}Pu atom density distributions at each burnup step for the LBU fuel rod (case1: left top, case2: right top, case3: left bottom, case4: right bottom).

The axial distribution of ^{239}Pu for the 25-day and 10-day burnup step cases are plotted in Figure 17. The red and black lines are the results of 10-day and 25-day burnup step cases, respectively. The average mass density of ^{239}Pu for the entire fuel rod, which is plotted by the dotted lines, is 3.84E-2g/cm^3 for the 10-day burnup step case and 3.83E-2g/cm^3 for 25-day burnup step case, respectively. As the two results show very good agreement, the 25-day burnup step is considered good enough in term of accuracy.

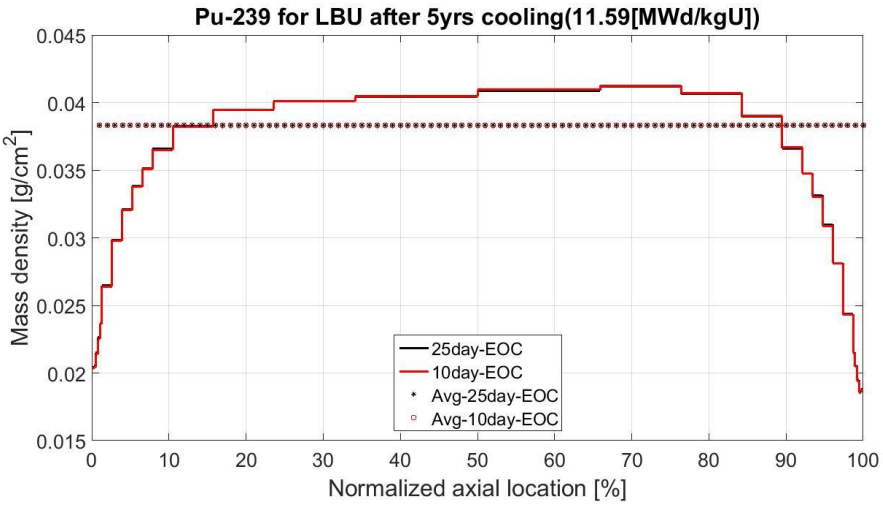

Figure 17 The axial distribution for ^{239}Pu after 5years cooling simulated with 10 (red) and 25 (black) days for burnup step.

3.1.2.2 Axial resolution

The ^{239}Pu mass density distributions with 30 and 381 meshes for the active fuel rod are compared as shown in Figure 18. The red and black lines are the axial distribution using 381 and 30 meshes, respectively. The dotted lines indicate the average mass density for the entire fuel rod. The average mass density of ^{239}Pu for both cases is 0.0383 g/cm^3. The axial distribution and average mass density between two cases show very good agreement; therefore, the 30 meshes configuration could be acceptable to achieve the reliable nuclide composition in spent fuel.

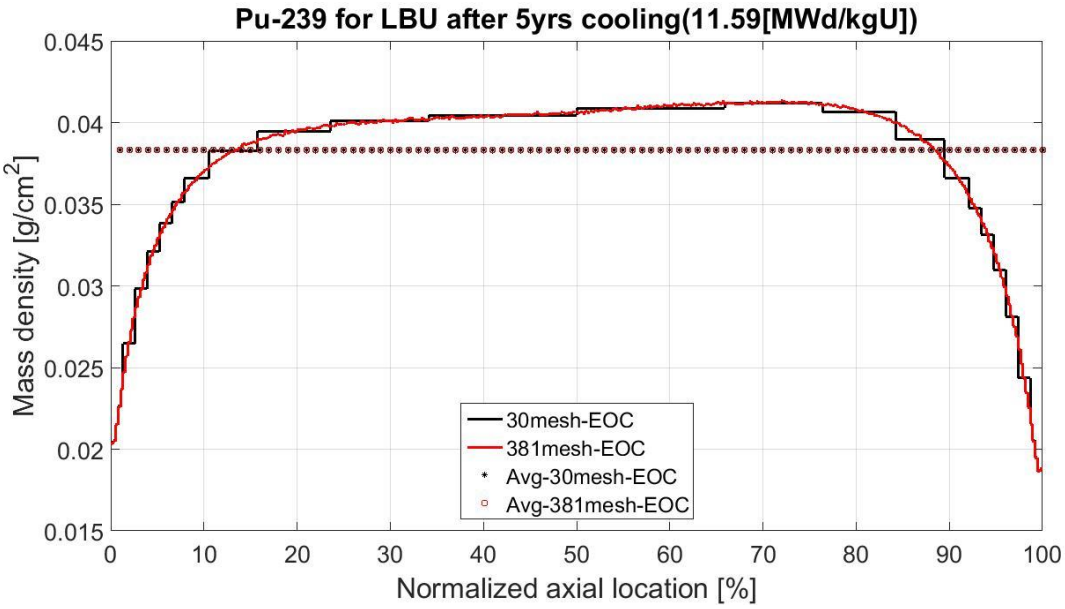

Figure 18 The axial distribution for ^{239}Pu after 5years cooling simulated with 381 (red) and 30 (black) meshes for the active fuel region.

3.1.2.3 Effect of axial water temperature change with respect to time

The water temperature and density as a function of burnup step are plotted in Figure 19. The thick black and green lines are the distribution for the beginning of cycle. The thick blue line is for that at the end of cycle using Eq. (3.3). The inlet and outlet temperatures of each burnup are identical as 296ºC and 328ºC. Based on these, the Pu and ^{244}Cm mass densities are plotted in Figure 20. The average Pu mass density, which is plotted by a dotted line, is 5.50E-2 g/cm^3 and 5.51E-2 g/cm^3 for the fixed and updated water temperature cases, respectively. The average ^{244}Cm mass density is 1.37E-5 g/cm^3 and 1.35E-5 g/cm^3 for the fixed and updated water temperature cases. The difference, which is evaluated by

$$\text{Difference b/w A and B}[\%] = \frac{|\text{A - B}|}{(\text{A} + \text{B})/2} \times 100\,, \tag{3.4}$$

are 0.11 and 0.98% for Pu and ^{244}Cm. By this result, we could conclude that the water temperature evaluated by Eq. (2.3) is well representative of that for the entire burnup steps.

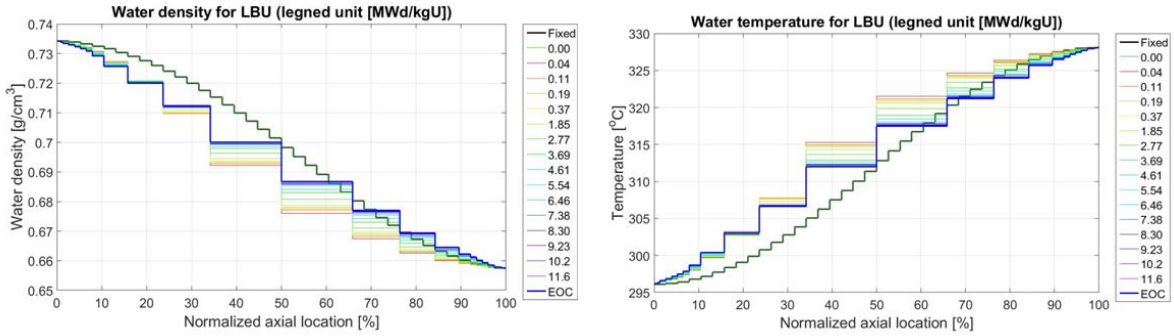

Figure 19 Change of water densities (left) and temperatures (right) as a function of burnup step.

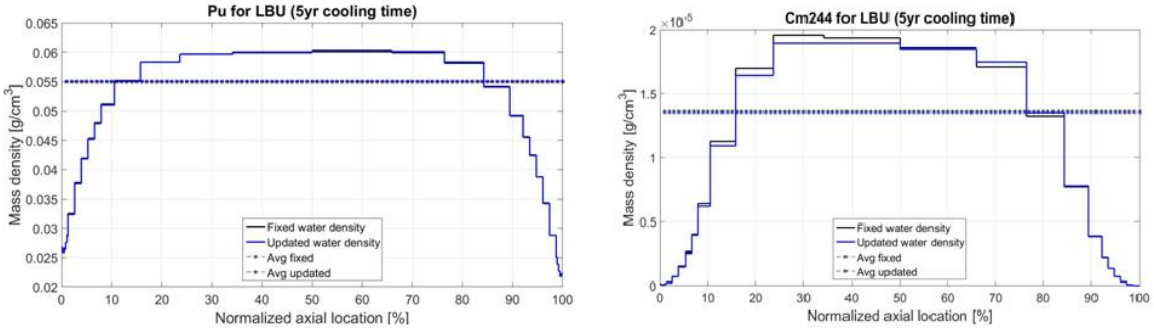

Figure 20 Axial distributions for Pu (left) and ^{244}Cm (right) after 5years cooling by two water temperature evaluation methods (black: the fixed water temperature case using Eq. (2.3), blue: the updated water temperature case using Eq. (3.3)).

3.1.2.4. Axial distribution for Pu and ^{244}Cm

The mass density of Pu and ^{244}Cm are evaluated based on the numerical recipes. The mass density in each mesh is normalized by the average mass density for the entire fuel rod. The normalized Pu (solid) and ^{244}Cm (dot) mass density distributions as a function of axial location for HBU (red) and LBU (blue) are plotted in Figure 21. The maximum and minimum Pu mass densities are 0.130 g/cm^3 and 0.0618 g/cm^3 for HBU, and 0.06 g/cm^3 and 0.0219 g/cm^3 for LBU. The maximum values for each burnup case are around 2 to 3 times greater than the minimum value. The maximum values are closer to the average values shown in Table 13 than the minimum values. The maximum and minimum ^{244}Cm mass densities are 1.10E-3 g/cm^3 and 5.14E-5 g/cm^3 for HBU, and 1.96E-5 g/cm^3 and 2.50E-8 g/cm^3 for LBU, respectively. The maximum values are 21 and 784 times greater than the minimum values for HBU and LBU. The axial non-uniformity of ^{244}Cm is more significant than that of Pu. By comparing between the red and blue lines for each actinide in Figure 21, it would be said that the axial non-uniformity becomes less significant as burnup increases. The mass density of Pu peaks at 70 to 80% height from the bottom of the fuel rod. The peaking of ^{244}Cm mass density is at near 30 and 80% for LBU and HBU, respectively. Based on these observations, the more detailed discussions on the axial non-uniformity will be made in the next section.

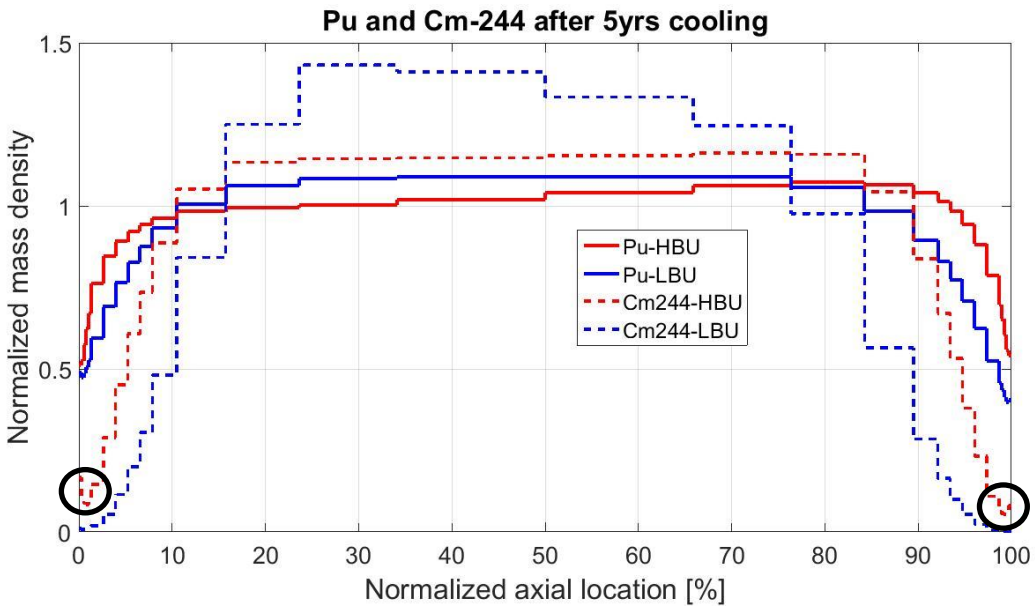

Figure 21 Normalized mass density for Pu (solid) and ^{244}Cm (dot) as a function of axial location for the LBU (blue) and HBU (red) single fuel pin-cell.

Table 13 Average mass density of Pu and ^{244}Cm for the entire fuel rod.

Unit: [g/cm^3]	HBU	LBU
Pu mass density	1.21E-01	5.50E-02
^{244}Cm mass density	9.63E-04	1.37E-05

3.1.3 Discussion

3.1.3.1 Axial distribution for Pu and ^{244}Cm

As mentioned in the previous Section, the non-uniformity of ^{244}Cm mass density in the axial direction is more significant than that of Pu. For this discussion, first, the atom density of ^{239}Pu with respect to time (t) is driven as following

$$\frac{dN_{Pu239}}{dt} = N^{0}_{U238}\sigma^{\gamma}_{U238}\phi - N_{Pu239}\sigma^{abs}_{Pu239}\phi,$$
$$\text{I.C.: } N_{Pu239}(t=0) = 0,\ N_{U238}(t=0) = N^{0}_{U238}, \tag{3.5}$$
$$N_{Pu239}(t) = \frac{N^{0}_{U238}\sigma^{\gamma}_{U238}}{\sigma^{abs}_{Pu239}}\left(1 - \exp(-\sigma^{abs}_{Pu239}\phi\, t)\right),$$

where N^{0}_{U238} is the initial atom density of ^{238}U, $N_{Pu239}(t)$ is the atom density of ^{239}Pu at time t, σ^{γ}_{U238} is the one-group capture cross section of ^{238}U, σ^{abs}_{Pu239} is the one-group absorption cross section of ^{239}Pu, and ϕ is the one-group neutron flux. The equation consists of two parts such as gain and loss terms. ^{239}Pu is generated by the neutron capture in ^{238}U, in contrast, the absorption neutron in ^{239}Pu consumes itself. The initial conditions (I.C.) are no Pu isotopes, but ^{238}U. The analytical solution of this equation is also shown in Eq. (3.5).

The next decay chain of ^{239}Pu is ^{240}Pu for which the analytical solution of atom density with respect to time is shown below

$$\frac{dN_{Pu240}}{dt} = N_{Pu239}\sigma^{\gamma}_{Pu239}\phi - N_{Pu240}\sigma^{\gamma}_{Pu240}\phi,$$
$$\text{I.C.: } N_{Pu240}(t=0) = 0,\ N_{Pu239}(t=0) = 0,\ N_{U238}(t=0) = N^{0}_{U238},$$
$$N_{Pu240}(t) = \frac{N^{0}_{U238}\sigma^{\gamma}_{Pu239}\sigma^{\gamma}_{U238}}{\sigma^{abs}_{Pu239}\sigma^{\gamma}_{Pu240}} \times \left(1 + \frac{1}{\sigma^{\gamma}_{Pu239}\phi - \sigma^{\gamma}_{Pu240}\phi}\right) \tag{3.6}$$
$$\times \left(\sigma^{\gamma}_{Pu240}\phi\exp(-\sigma^{\gamma}_{Pu239}\phi\, t) - \sigma^{\gamma}_{Pu239}\phi\exp(-\sigma^{\gamma}_{Pu240}\phi\, t)\right),$$

where $N_{Pu240}(t)$ is the atom density of ^{240}Pu at time t, σ^{γ}_{Pu239} is the one-group capture cross section of ^{239}Pu, and σ^{γ}_{Pu240} is the one-group capture cross section of ^{240}Pu. In addition, the analytical solution for atom density with respect to time for ^{241}Pu and ^{242}Pu are shown below

$$\frac{dN_{Pu241}}{dt} = N_{Pu240}\sigma^{\gamma}_{Pu240}\phi - N_{Pu241}\sigma^{ab}_{Pu241}\phi$$
$$\text{I.C.: } N_{Pu241}(t=0) = 0, N_{Pu240}(t=0) = 0, N_{Pu239}(t=0) = 0,\ N_{U238}(t=0) = N^{0}_{U238}, \tag{3.7}$$
$$N_{Pu241}(t) = N^{0}_{U238}\sigma^{\gamma}_{U238}\sigma^{\gamma}_{Pu239}\sigma^{\gamma}_{Pu240}\left[\begin{array}{l} \dfrac{1}{\sigma^{abs}_{Pu239}\sigma^{\gamma}_{Pu240}\sigma^{abs}_{Pu241}} - \dfrac{\exp(-\sigma^{abs}_{Pu239}\phi\, t)}{\sigma^{abs}_{Pu239}\left(\sigma^{abs}_{Pu239} - \sigma^{\gamma}_{Pu240}\right)\left(\sigma^{abs}_{Pu239} - \sigma^{abs}_{Pu241}\right)} \\ + \dfrac{\exp(-\sigma^{\gamma}_{Pu240}\phi\, t)}{\left(\sigma^{abs}_{Pu239} - \sigma^{\gamma}_{Pu240}\right)\sigma^{\gamma}_{Pu240}\left(\sigma^{\gamma}_{Pu240} - \sigma^{abs}_{Pu241}\right)} \\ + \dfrac{\exp(-\sigma^{abs}_{Pu241}\phi\, t)}{\left(\sigma^{abs}_{Pu239} - \sigma^{abs}_{Pu241}\right)\left(\sigma^{abs}_{Pu241} - \sigma^{\gamma}_{Pu240}\right)\sigma^{abs}_{Pu241}} \end{array}\right]$$

$$\frac{dN_{Pu242}}{dt} = N_{Pu241}\sigma^{\gamma}_{Pu241}\phi - N_{Pu242}\sigma^{\gamma}_{Pu242}\phi$$

I.C.: $N_{Pu242}(t=0)=0, N_{Pu241}(t=0)=0, N_{Pu240}(t=0)=0, N_{Pu239}(t=0)=0,\ N_{U238}(t=0)=N^{0}_{U238}$

$$N_{Pu242}(t) = N^{0}_{U238}\sigma^{\gamma}_{U238}\sigma^{\gamma}_{Pu239}\sigma^{\gamma}_{Pu240}\sigma^{\gamma}_{Pu241}\left[\begin{array}{l}\dfrac{1}{\sigma^{abs}_{Pu239}\sigma^{\gamma}_{Pu240}\sigma^{abs}_{Pu241}\sigma^{\gamma}_{Pu242}} + \dfrac{\exp(-\sigma^{abs}_{Pu239}\phi\, t)}{\sigma^{abs}_{Pu239}\left(\sigma^{abs}_{Pu239}-\sigma^{\gamma}_{Pu240}\right)\left(\sigma^{abs}_{Pu239}-\sigma^{abs}_{Pu241}\right)\left(\sigma^{abs}_{Pu239}-\sigma^{\gamma}_{Pu242}\right)} \\ -\dfrac{\exp(-\sigma^{\gamma}_{Pu240}\phi\, t)}{\left(\sigma^{abs}_{Pu239}-\sigma^{\gamma}_{Pu240}\right)\sigma^{\gamma}_{Pu240}\left(\sigma^{\gamma}_{Pu240}-\sigma^{abs}_{Pu241}\right)\left(\sigma^{\gamma}_{Pu240}-\sigma^{\gamma}_{Pu242}\right)} \\ -\dfrac{\exp(-\sigma^{abs}_{Pu241}\phi\, t)}{\left(\sigma^{abs}_{Pu239}-\sigma^{abs}_{Pu241}\right)\left(\sigma^{abs}_{Pu241}-\sigma^{\gamma}_{Pu240}\right)\sigma^{abs}_{Pu241}\left(\sigma^{abs}_{Pu241}-\sigma^{\gamma}_{Pu242}\right)} \\ -\dfrac{\exp(-\sigma^{\gamma}_{Pu242}\phi\, t)}{\left(\sigma^{abs}_{Pu239}-\sigma^{\gamma}_{Pu242}\right)\left(\sigma^{\gamma}_{Pu242}-\sigma^{\gamma}_{Pu240}\right)\left(\sigma^{\gamma}_{Pu242}-\sigma^{abs}_{Pu241}\right)\sigma^{\gamma}_{Pu242}}\end{array}\right] \quad (3.8)$$

There are several decay chains for ^{244}Cm from ^{238}U. Among those, one decay chain shown in Figure 22 is selected based on the highest probability for production of ^{244}Cm. Based on this decay chain, the analytical solution for ^{244}Cm atom density as a function of time is shown below

$$\frac{dN_{Cm244}}{dt} = \lambda_{Am244}N_{Am244} - N_{Cm244}\sigma^{\gamma}_{Cm244}\phi$$

I.C.: $N_{U238}(t=0)=N^{0}_{U238}, N_{Pu239}(t=0)=0, N_{Pu240}(t=0)=0, N_{Pu241}(t=0)=0, N_{Pu242}(t=0)=0,$
$N_{Pu243}(t=0)=0, N_{Am243}(t=0)=0, N_{Am244}(t=0)=0, N_{Cm244}(t=0)=0,$

$$N_{Cm244}(t) = N^{0}_{U238}\sigma^{\gamma}_{U238}\phi\sigma^{\gamma}_{Pu239}\phi\sigma^{\gamma}_{Pu241}\phi(abcdefgh)\left[\begin{array}{l}\dfrac{1}{abcdefgh} + \dfrac{\exp(-a\,t)}{a(a-b)(a-c)(a-d)(a-e)(a-f)(a-g)(a-h)} \\ -\dfrac{\exp(-b\,t)}{b(a-b)(b-c)(b-d)(b-e)(b-f)(b-g)(b-h)} \\ -\dfrac{\exp(-c\,t)}{c(a-c)(c-b)(c-d)(c-e)(c-f)(c-g)(c-h)} \\ -\dfrac{\exp(-d\,t)}{d(a-d)(d-b)(d-c)(d-e)(d-f)(d-g)(d-h)} \\ -\dfrac{\exp(-e\,t)}{e(a-e)(e-b)(e-c)(e-d)(e-f)(e-g)(e-h)} \\ -\dfrac{\exp(-f\,t)}{f(a-f)(f-b)(f-c)(f-d)(f-e)(f-g)(f-h)} \\ -\dfrac{\exp(-g\,t)}{g(a-g)(g-b)(g-c)(g-d)(g-e)(g-f)(g-h)} \\ -\dfrac{\exp(-h\,t)}{h(a-h)(h-b)(h-c)(h-d)(h-e)(h-f)(h-g)}\end{array}\right] \quad (3.9)$$

where $a=\sigma^{abs}_{Pu239}\phi, b=\sigma^{\gamma}_{Pu240}\phi, c=\sigma^{abs}_{Pu241}\phi, d=\sigma^{\gamma}_{Pu242}\phi,\ e=\lambda_{Pu243}, f=\sigma^{\gamma}_{Am243}\phi, g=\lambda_{Am244}, h=\sigma^{\gamma}_{Cm244}\phi$

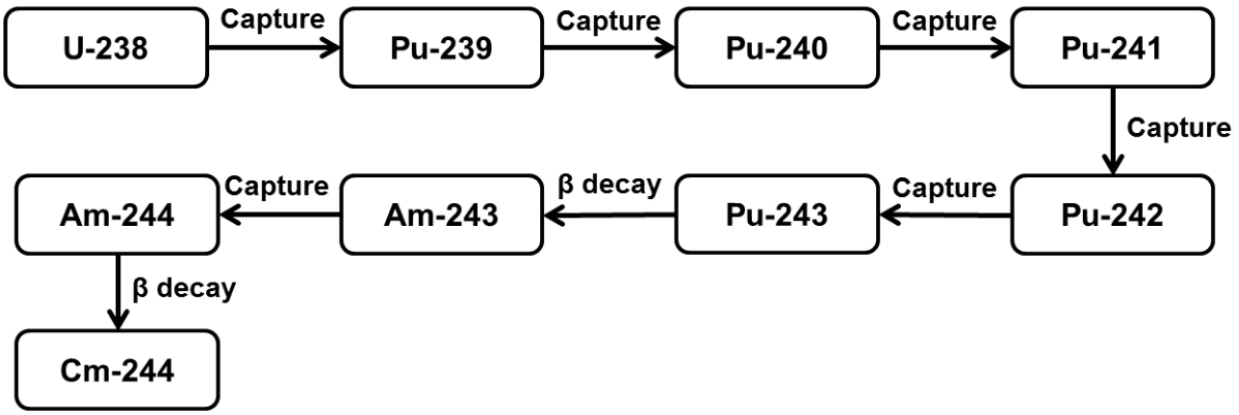

Figure 22 Decay chain for ^{244}Cm considered.

In order to decide dominant terms, the nuclear data at 2200m/s (thermal neutron) and the decay constants for precursor isotopes of ^{244}Cm as shown in Table 14 is substituted into Eq. (3.9).

Table 14 Cross section data at 2200m/s and decay constants for precursor isotopes of ^{244}Cm

Parameters	values
σ^{γ}_{U238}	2.73 [barn]
σ^{γ}_{Pu239}	274 [barn]
σ^{abs}_{Pu239}	1120 [barn]
σ^{γ}_{Pu240}	286 [barn]
σ^{abs}_{Pu241}	1380 [barn]
σ^{γ}_{Pu242}	30 [barn]
σ^{γ}_{Am243}	80 [barn]
σ^{γ}_{Cm244}	15 [barn]
λ_{Pu243}	3.88E-5 [1/s]
λ_{Am244}	1.9E-5 [1/s]
ϕ	1E14 [#/cm^2/s]
N^0_{U238}	2.29E22 [#/cm^3]

The dominant terms are 1st, 5th, 7th, and 9th terms, because those terms have 10^{54} order of magnitude coefficient and the smallest exponential value as $e^{-1E\text{-}9\times t}$. After removing terms except three terms, the Eq. (3.9) can be rewritten as

$$\begin{aligned}
N_{Cm244}(t) &= X\left[Y - D\exp(-\sigma^{\gamma}_{Pu242}\phi\, t) - F\exp(-\sigma^{\gamma}_{Am243}\phi\, t) - H\exp(-\sigma^{\gamma}_{Cm244}\phi\, t)\right], \\
X &= N^{0}_{U238}\sigma^{\gamma}_{U238}\phi\sigma^{\gamma}_{Pu239}\phi\sigma^{\gamma}_{Pu241}\phi(abcdefgh), \\
Y &= \frac{1}{abcdefgh}, \\
D &= \frac{1}{d(a-d)(d-b)(d-c)(d-e)(d-f)(d-g)(d-h)}, \\
F &= \frac{1}{f(a-f)(f-b)(f-c)(f-d)(f-e)(f-g)(f-h)}, \\
H &= \frac{1}{h(a-h)(h-b)(h-c)(h-d)(h-e)(h-f)(h-g)}.
\end{aligned} \tag{3.10}$$

The order of magnitudes of microscopic capture cross sections of ^{242}Pu, ^{243}Am, and ^{244}Cm are equal as 10 to 1, therefore, one simplification is done by replacing of three values into σ' as

$$\begin{aligned}
N_{Cm244}(t) &= X'\left[1 - M\exp(-\sigma'\phi\, t)\right], \\
X' &= \frac{X}{Y}, \\
M &= \frac{D+F+H}{Y}, \\
\sigma^{\gamma}_{Pu242} &\approx \sigma^{\gamma}_{Am243} \approx \sigma^{\gamma}_{Cm244} \equiv \sigma'.
\end{aligned} \tag{3.11}$$

In order to discuss the axial location effect, the parameter, z, which is the axial height information, is added. Then, the analytical solution for ^{239}Pu and ^{244}Cm with respect to time and the axial location (z) are summarized as below

$$\begin{aligned}
N_{Pu239}(t,z) &= \frac{N^{0}_{U238}\sigma^{\gamma}_{U238}}{\sigma^{abs}_{Pu239}}\left(1 - \exp(-\sigma^{abs}_{Pu239}\phi(t,z)\, t)\right), \\
N_{Cm244}(t,z) &= X'\left[1 - M\exp(-\sigma'\phi(t,z)\, t)\right],
\end{aligned} \tag{3.12}$$

where σ' is approximately 10 [barn], and σ^{abs}_{Pu239} is 1120 [barn]. First, the flux at the middle of a fuel rod (ϕ^{Middle}) is greater than top (ϕ^{Top}) and bottom (ϕ^{Bottom}) of a fuel rod as

$$\phi^{Middle} > \phi^{Top} \text{and } \phi^{Bottom} \tag{3.13}$$

causing non-uniformity for all nuclides in the axial direction. If this is only the term to influence on the axial non-uniformity, the axial distribution of all isotopes should be identical. However,

that is not true as shown in Figure 21. The exponential value in analytical solutions consists of the neutron flux, the cross section, and the time. Not only the neutron flux but also the time and the cross-section data can be factors to determine the shape of axial isotope distribution. The slope of axial concentration distribution is steeper when the exponent value is smaller. The capture cross section of ^{244}Cm is smaller than that of absorption cross section of ^{239}Pu; therefore, the non-uniformity of ^{244}Cm is more significant than that of ^{239}Pu as shown in Figure 23.

The decreasing of non-uniformity of isotopes as a function of time can be explained with a similar way. As burnup increases, the values of the exponents become more negative, resulting in less steeper slopes. Therefore, the non-uniformity of nuclide composition in the axial direction for LBU is more significant than that of HBU as shown in Figure 21.

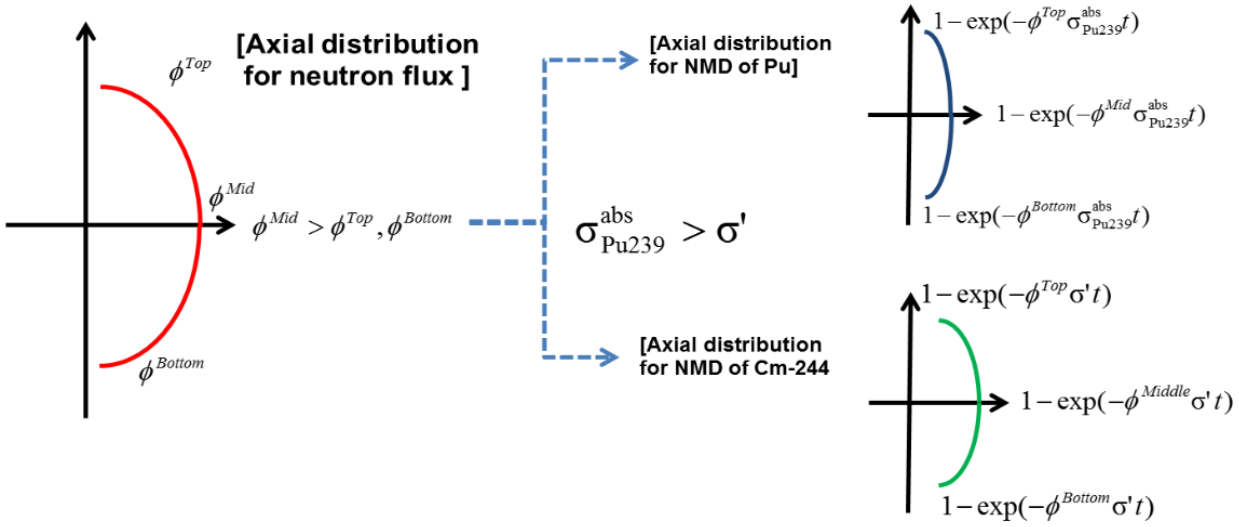

Figure 23 Diagram to explain the effect of cross section on the axial non-uniformity.

3.1.3.2 Axial peaking of ^{239}Pu and ^{244}Cm

The axial normalized mass densities of ^{239}Pu at different burnup steps with different colors are plotted in Figure 24. The thick blue and red lines are the axial distributions at 0.04MWd/kgU and after the 5-year cooling time from discharged. Let us recall Eq. (3.5) with adding a location term (z) for all parameters as shown below

$$N_{Pu239}(t,z) = \frac{N^{0}_{U238}(z)\times\sigma^{\gamma}_{U238}(t,z)}{\sigma^{abs}_{Pu239}(t,z)}\left(1-\exp\left(-\sigma^{abs}_{Pu239}(t,z)\times\phi(t,z)\times t\right)\right). \quad (3.14)$$

In order to discuss the axial peak at the beginning of cycle or low burnup, it is assumed time (t) is zero. Then, Eq. (3.14) is rewritten into

$$N_{Pu239}(t,z)=\frac{N^{0}_{U238}(z)\times\sigma^{\gamma}_{U238}(t,z)}{\sigma^{abs}_{Pu239}(t,z)}\left(-\sigma^{abs}_{Pu239}(t,z)\times\phi(t,z)\times t\right)=N^{0}_{U238}\times\sigma^{\gamma}_{U238}(t,z)\times\phi(t,z)\times t, \quad (3.15)$$
$$\left(\because t\sim 0\Rightarrow\left(1-\exp(-\sigma^{abs}_{Pu239}(t,z)\times\phi(t,z)\times t)\right)\approx\left(-\sigma^{abs}_{Pu239}(t,z)\times\phi(t,z)\times t\right)\right).$$

By Eq. (3.15), it would be said that the dominant factor in determination of ^{239}Pu concentration at the beginning of depletion is the axial flux and the axial capture cross section of ^{238}U distribution. The axial variation of flux is more significant than that of the ^{238}U capture cross section. Therefore, the axial distribution of ^{239}Pu is similar with that of flux as shown in Figure 25.

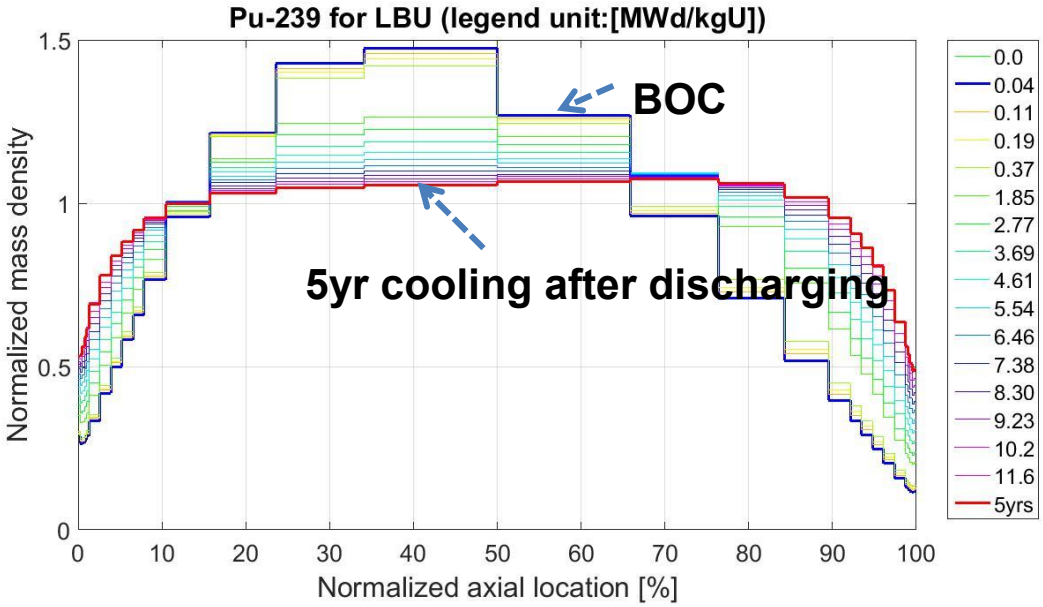

Figure 24 Normalized mass density of ^{239}Pu as a function of axial location (x-axis) and burnup up (color) for LBU.

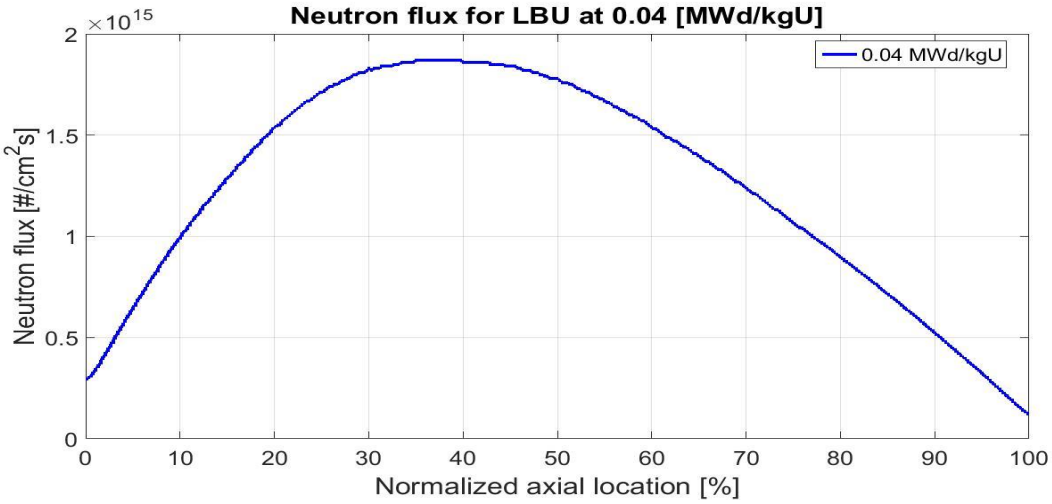

Figure 25 The axial distributions for flux (left) and mass density of ^{239}Pu (right) at 0.04 [MWd/kgU] for LBU.

In contrast, the analytical solution is modified from Eq. (3.14) by assuming time (t) is infinite as following

$$N_{Pu239}(t,z) = \frac{N^{0}_{U238}(z) \times \sigma^{\gamma}_{U238}(t,z)}{\sigma^{abs}_{Pu239}(t,z)}, \quad \left(\because t \to \infty \Rightarrow \exp(-\sigma^{abs}_{Pu239}(t,z) \times \phi(t,z) \times t) \approx 0\right). \tag{3.16}$$

By this derivation, it would say that the ratio of capture cross section of ^{238}U to the absorption cross section of ^{239}Pu gets a more significant factor in determination of the axial ^{239}Pu concentration as a time goes on. Therefore, we need to consider not only the flux distribution, but also the absorption cross section of ^{239}Pu and the capture cross section of ^{238}U. By plotting of the ratio of two cross sections and flux at the end of cycle and burnup as shown in Figure 26, the axial peak of ^{239}Pu at near 70 % height after 5-year cooling time from discharged is reasonable.

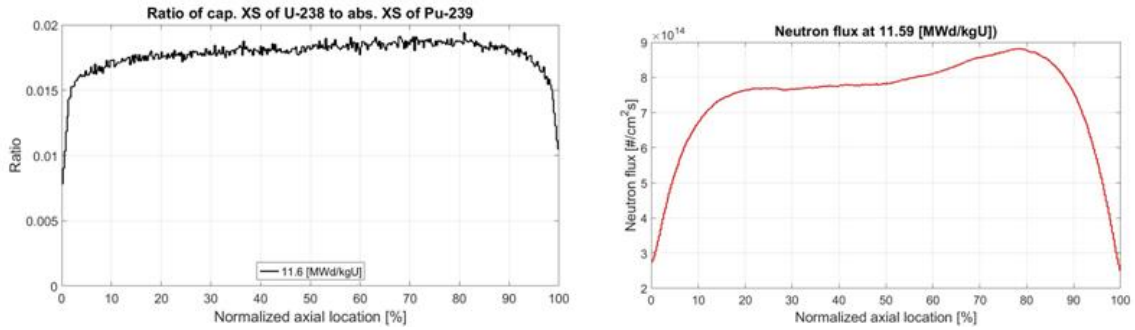

Figure 26 Ratio of capture cross section of U-238 to absorption cross section of Pu-239 (left) and flux (right) as a function of axial location at the end of cycle (11.50MWd/kgU) for LBU.

The axial normalized mass density distributions of ^{244}Cm at different burnup steps are plotted in Figure 27. At the beginning of cycle, the axial peak distribution is at 40% height, which is similar to that of ^{239}Pu, because of the axial neutron flux distribution. However, at the end of cycle, the peak of ^{244}Cm is shown at 30% height. The daughter of ^{239}Pu is ^{240}Pu. ^{241}Pu is generated by the neutron capture of ^{240}Pu. Then, finally, ^{244}Cm is produced through several decay chains. The shape of axial ^{244}Cm distribution would be close to that of ^{240}Pu and ^{241}Pu rather than that of ^{239}Pu. The peaking of axial mass density for ^{240}Pu (black) and ^{241}Pu are around at 30% height as shown in Figure 28. Therefore, the ^{244}Cm mass density peaks at 30% height at the end of cycle. However, as time goes on, the axial distribution of ^{244}Cm shows analogous trend with the that of Pu, because ^{239}Pu is the very first precursor of ^{244}Cm.

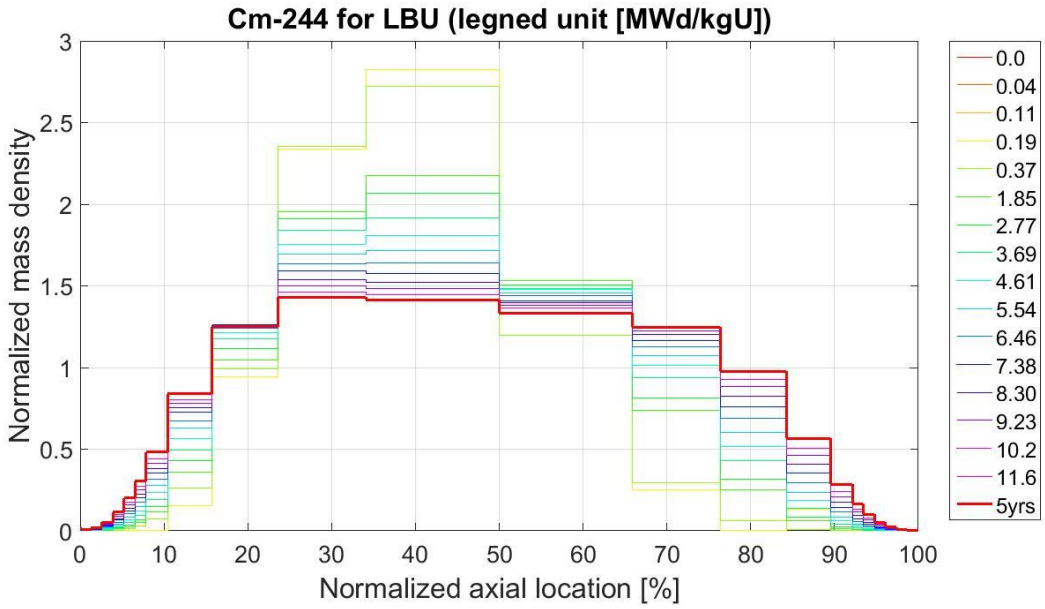

Figure 27 Normalized mass densities of ^{244}Cm as a function of axial location (x-axis) and burnup up (color) for LBU.

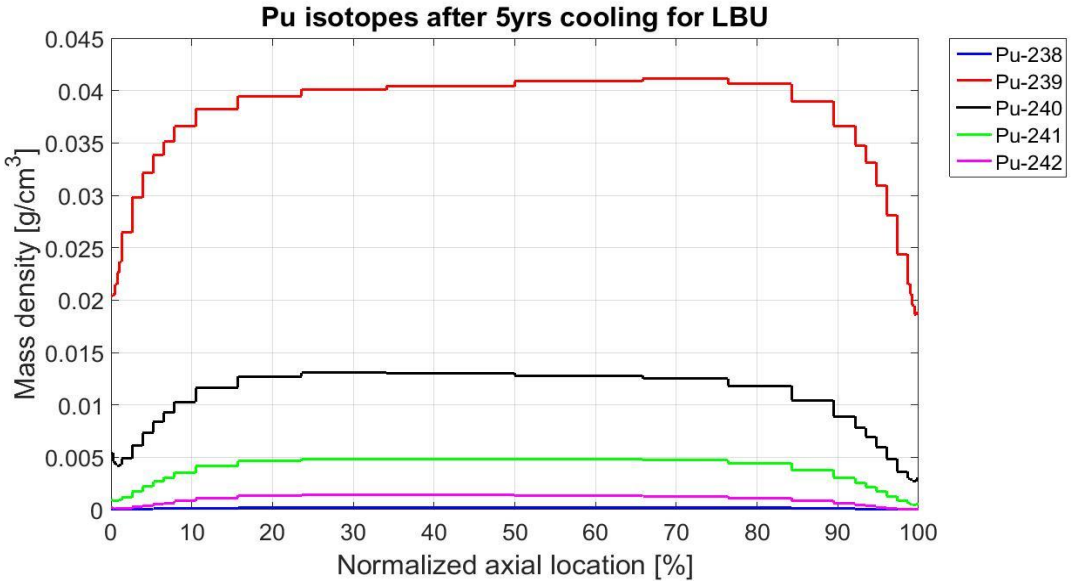

Figure 28 Axial mass density distributions of Pu isotopes after the 5-year cooling time.

3.1.3.3 Nuclear reactions near axial surface regions

The mass density suddenly decreases at few centimeters from an axial surface of fuel rod as marked with black dot circles in Figure 21. It would be due to the axial rim-effect. The rim-effect is occurred by the moderated neutrons, particularly within resonance energy range, are mostly captured at the surface of fuel, ^{238}U. Therefore, the ^{239}Pu mass density shows peaking at the radial surface, and then it dramatically decreases as farther from the surface. This kind of phenomena

would affect in the axial direction. In other words, the moderated neutrons are captured at the surface before penetrating through the fuel in the axial direction as shown in Figure 29.

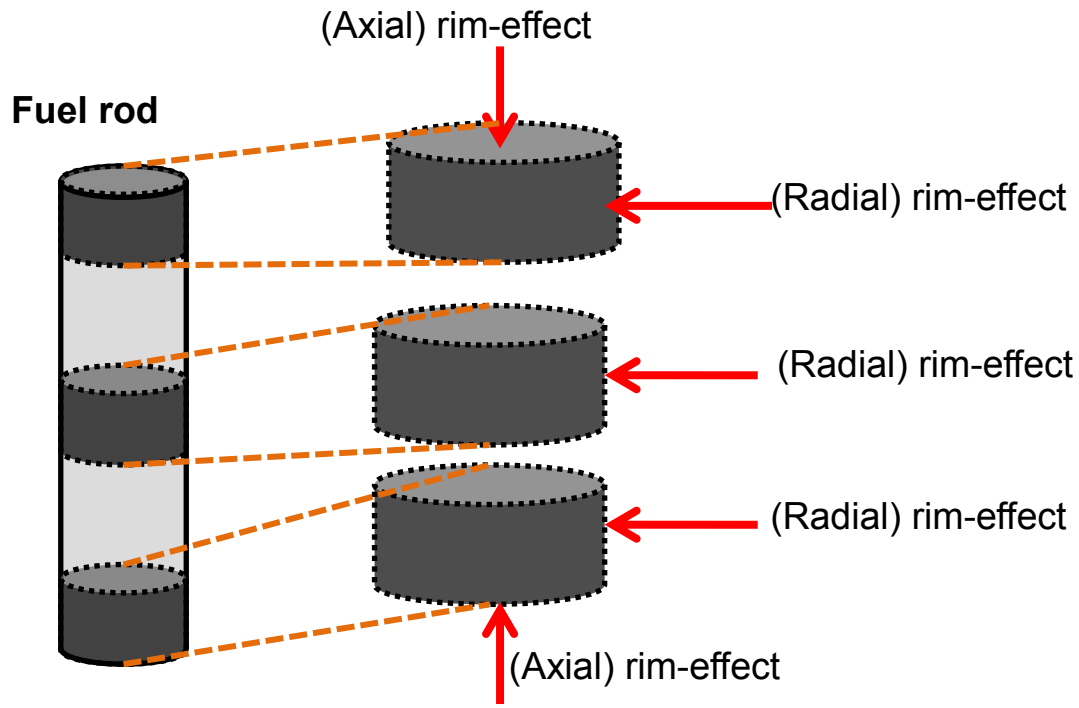

Figure 29 Diagram to explain the axial rim-effect.

3.2 Characterization of nuclide composition non-uniformity for representative spent fuel assemblies

3.2.1 Axial distributions for Pu and ^{244}Cm for the representative spent fuel assemblies

The Pu (a linear scale) and ^{244}Cm (a semi-log scale) mass densities of each fuel rod (a single solid line) for the Type-0 (1st row), -1 (2nd row), and -2 (3rd row) fuel assembly depending on the depleting cycles (blue lines: 1cycle, black lines: 2cycles, and red lines: 3cycles) have been plotted as a function of the axial location in Figure 30. The averages of those case for the entire assembly are summarized in Table 15 and plotted by the dot lines in the figures. The 5-year cooling time after discharging is taken into account for all following results. The phenomena discussed in the previous discussion section (section 3.1.3) can be observed as following. First, the Pu and ^{244}Cm concentrations have increased as a function of burnup. Second, the axial peaking location is varied depending on burnup. For example, at the low burnup case, the peaking point is a little below from

the middle of the fuel rod, however, the peaking location moves to the higher location at the high burnup case. Third, the significant non-uniformity of Pu and ^{244}Cm mass density at the bottom and top of fuel rods has been observed for all results cases. Fourth, the axial non-uniformity of ^{244}Cm is more significant than that of Pu. Fifth, the axial non-uniformity is getting flatter as increasing burnup.

The two lines of each depletion case in the Type-1 and -2 fuel assembly results are distributed a little far away from the group of lines, but they are close each other. Those two lines for Pu mass density are greater than others and the average Pu mass density for the entire assembly, whereas the two lines for ^{244}Cm mass densities are less than others and the average mass density for the assembly. The two lines are results for GBFs. The GBF consists of 6w% of gadolinium oxide (Gd_2O_3) and 94w% of natural uranium dioxide (UO_2) as shown in Table 6. In other words, there are greater ^{238}U concentration contained in GBFs than that in normal or low enriched fuel rods. Therefore, the breeding ^{239}Pu from ^{238}U in GBFs is relatively more active than that in other fuel rods. This leads greater Pu concentrations in GBFs. ^{244}Cm is produced by multiple combinations of neutron capture reactions and beta decay from ^{238}U. However, the neutron absorption cross section of Gd (Σ_a of Gd for the thermal neutron (2200m/s) 1403 cm^{-1}) is generally greater than that of precursors of ^{244}Cm. Therefore, the more neutrons are absorbed in Gd of GBFs than mother isotopes of ^{244}Cm. This could be the fact that disturbs the production of ^{244}Cm in GBFs. Generally, the non-uniformity of nuclide composition in spent fuel assemblies containing GBFs is more significant than that of spent fuel assemblies without GBFs.

Based on the simulation results, the ratio of Pu-to-^{244}Cm-ratio in spent fuel has a large variation depending on the depletion scheme, the fuel assembly type, the axial location, and the loading location in the assembly.

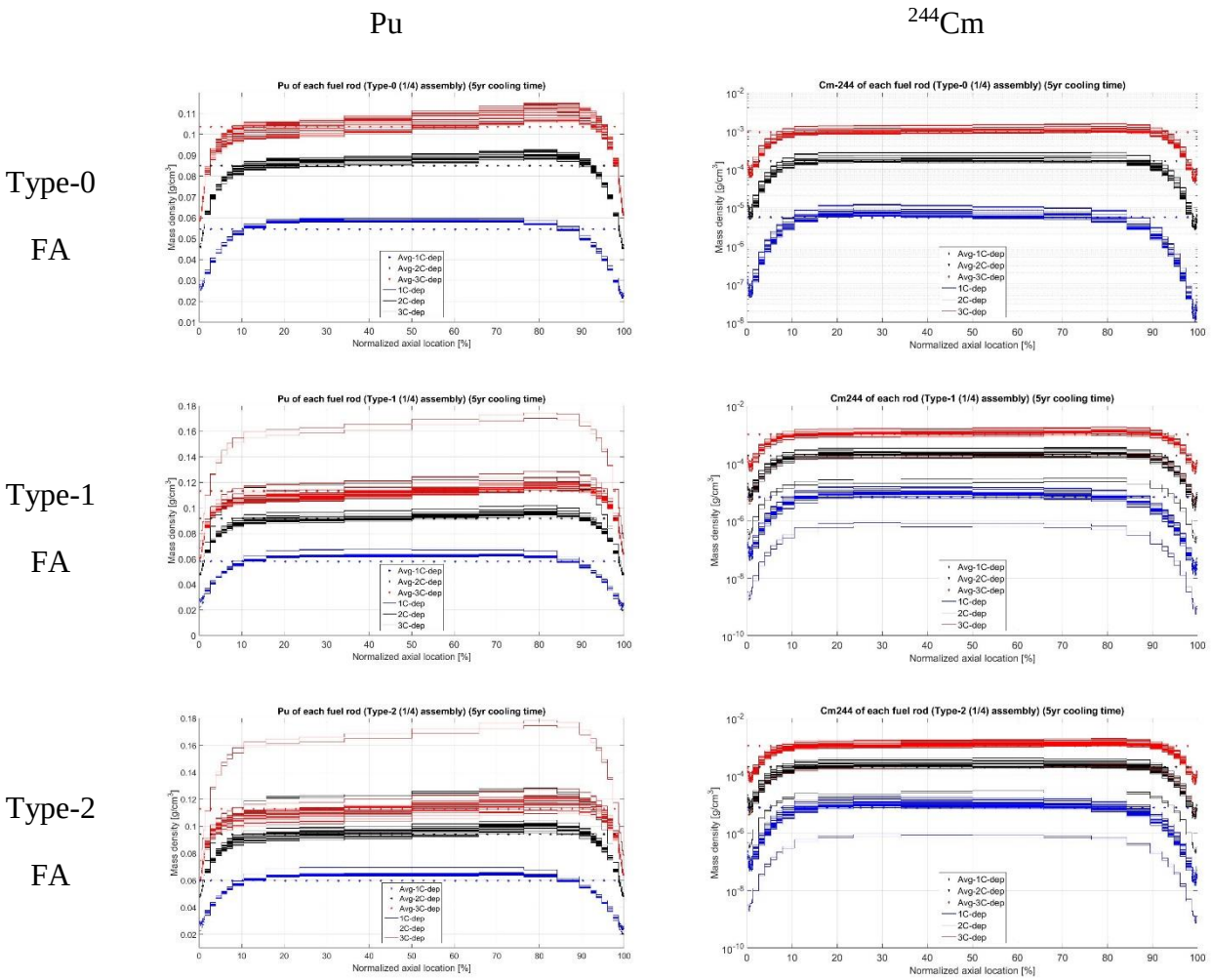

Figure 30 Axial Pu (1st column) and ^{244}Cm (2nd column) mass density distributions of each fuel rod for the Type-0 (1st row), -1 (2nd row), and -2 (3rd row) fuel assembly with three depleting cycle cases (blue line: 1 cycle, black line: 2cycles, red line: 3 cycles).

Table 15 Average Pu and ^{244}Cm mass density for the entire Type-0, -1, and -2 fuel assemblies after 1, 2, and 3 cycles depletion.

FA Type	Depletion period	Pu [g/cm^3]	^{244}Cm [g/cm^3]	Ratio
Type-0	1 cycle	5.45E-02	5.52E-06	9.88E+02
	2 cycles	8.49E-02	1.60E-04	5.32E+02
	3 cycles	1.04E-01	9.28E-04	1.12E+02
Type-1	1 cycle	5.82E-02	6.74E-06	8.63E+03
	2 cycles	9.16E-02	1.84E-04	4.99E+02
	3 cycles	1.13E-01	1.02E-03	1.11E+02
Type-2	1 cycle	5.99E-02	7.76E-06	7.71E+03
	2 cycles	9.42E-02	2.04E-04	4.61E+02
	3 cycles	1.13E-01	1.10E-03	1.02E+02

3.2.2 Axial and radial non-uniformity of nuclide compositions

The normalized radial distributions for each axial location have obtained in this section. The mass density and the reaction rate, are plotted as a function of the normalized radial location from the center to the surface of the fuel rod for every axial location which is distinguished by the color of lines as shown in Figure 31. In order to discuss in detail, the thick red line is the radial distribution at the middle of the fuel rod in the axial direction. The thick green and blue lines are the radial results at the top and bottom of the fuel rod in the axial direction.

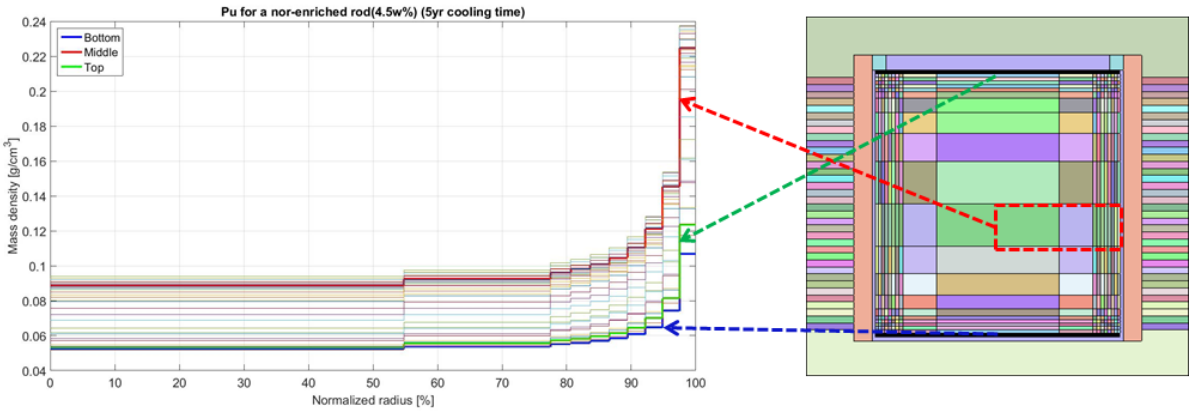

Figure 31 Description showing how to plot the radial non-uniformity for each axial layer mesh.

The Pu and ^{244}Cm mass density in the radial direction for each axial height of the 4.5 w% and 4.0 w% enriched fuel rods with different depletion lengths (1st column: 1cycle depletion, 2nd

column: 2 cycles depletion, and 3rd column: 3 cycles depletion) are plotted in Figure 32. The mass density of Pu and ^{244}Cm at the perimeter of the fuel rod is generally two or three times greater than that at the center of the fuel rod. This could be caused by the high probability of neutron captures in ^{238}U at the surface of a fuel rod, so called the rim effect [48–50]. The rim region is approximately tens to hundreds μm in thickness from the surface of the fuel rod. Therefore, the first radial mesh from the surface shows the greatest Pu mass density. The production of Am and Cm, which are produced subsequently to the neutron capture reaction and the beta decay from ^{239}Pu, are also enhanced at the surface region [48].

Pu for the 4.5w% enriched fuel rod

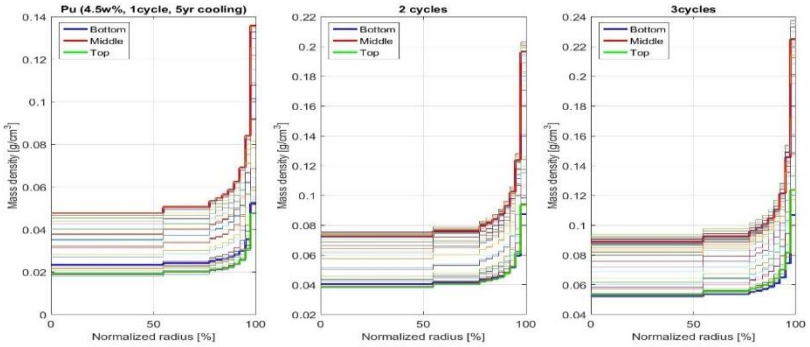

Pu for the 4.0w% enriched fuel rod

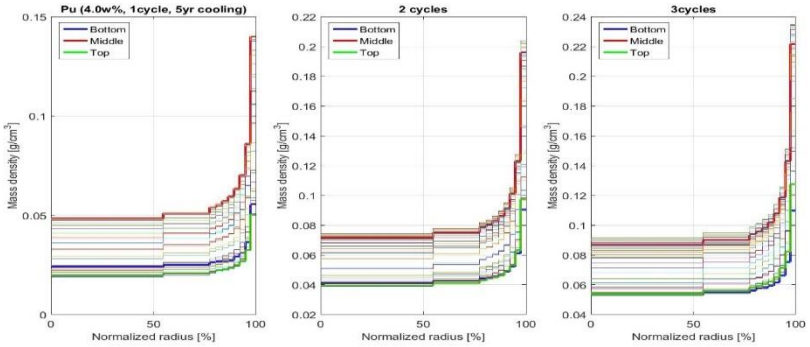

^{244}Cm for the 4.5w% enriched fuel rod

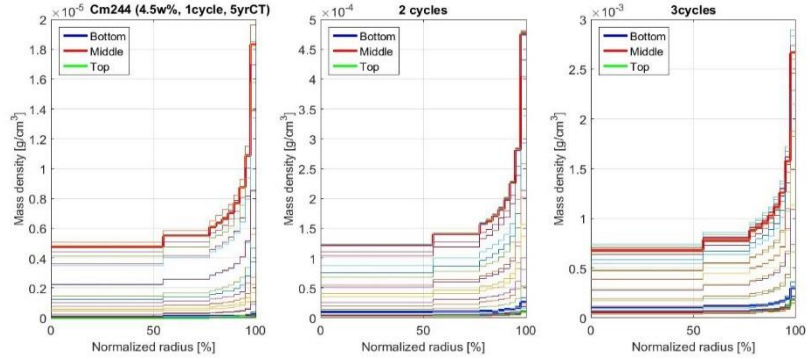

^{244}Cm for the 4.0w% enriched fuel rod

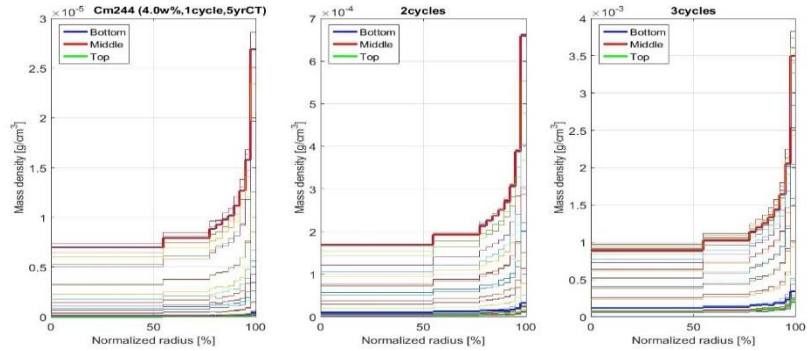

Figure 32 The radial distribution of Pu and ^{244}Cm for the 4.5 and 4.0w% enriched fuel rods in the Type-0 fuel assembly.

Pu for the 4.5w% enriched fuel rod

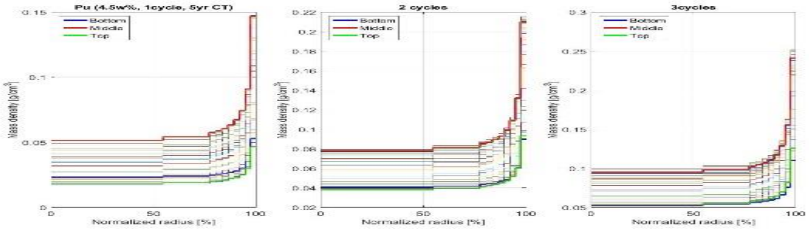

Pu for the 4.0w% enriched fuel rod

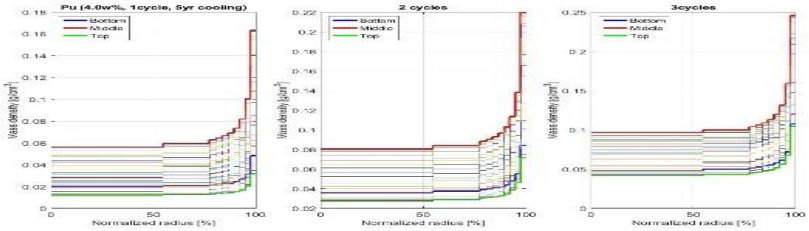

Pu for the GBF

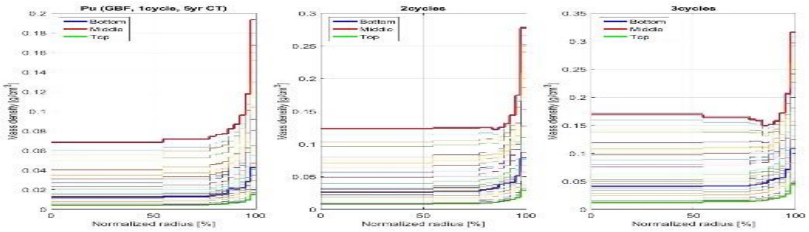

^{244}Cm for the 4.5w% enriched fuel rod

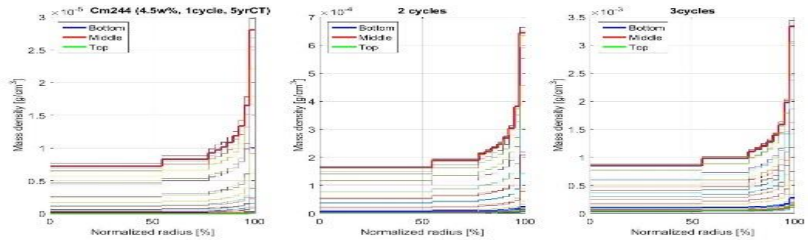

^{244}Cm for the 4.0w% enriched fuel rod

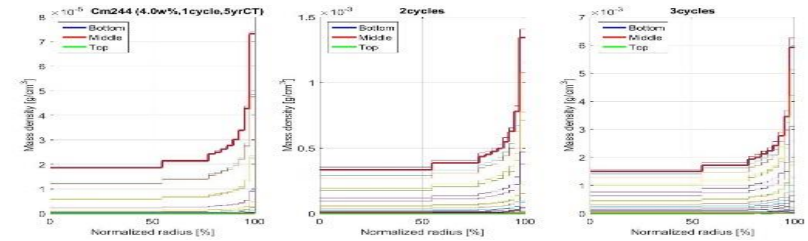

^{244}Cm for the GBF

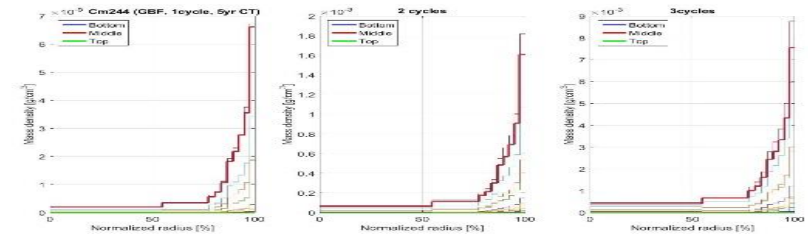

Figure 33 The radial Pu and ^{244}Cm distributions for the Type-1 fuel assembly.

Pu for the 4.5w% enriched fuel rod

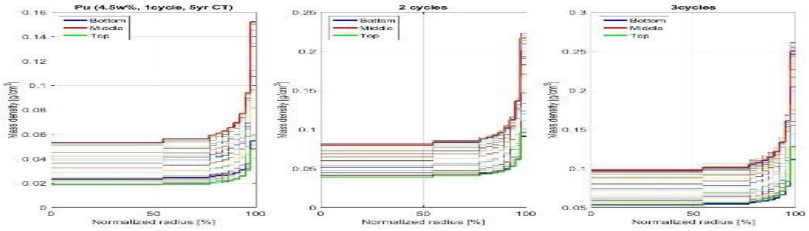

Pu for the 4.0w% enriched fuel rod

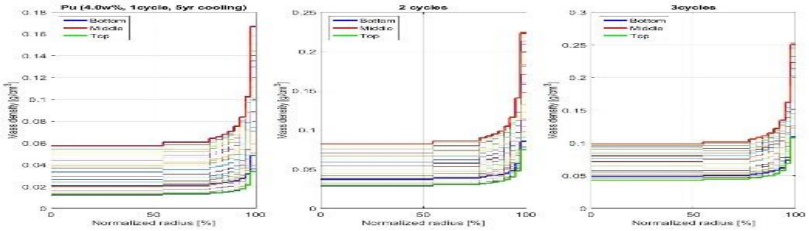

Pu for the GBF

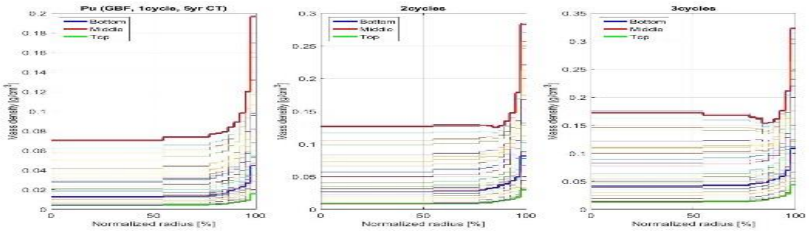

^{244}Cm for the 4.5w% enriched fuel rod

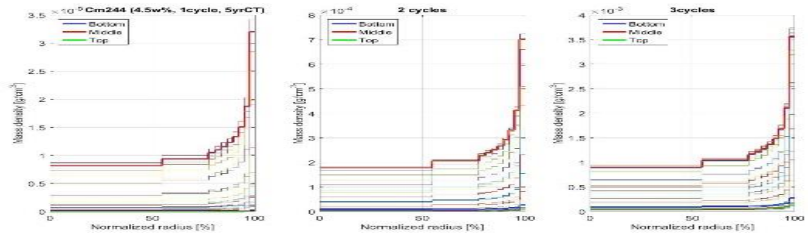

^{244}Cm for the 4.0w% enriched fuel rod

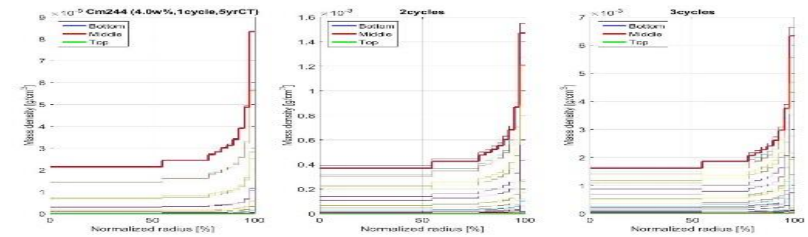

^{244}Cm for the GBF

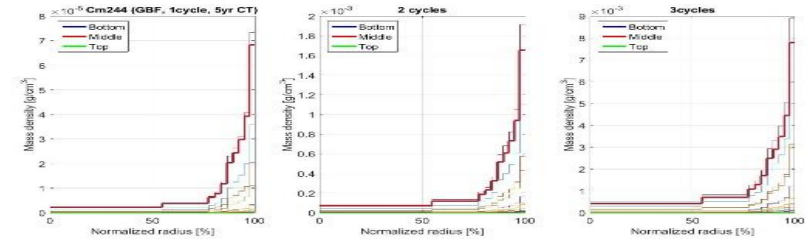

Figure 34 The radial Pu and ^{244}Cm distributions for the Type-2 fuel assembly.

The radial distributions for Pu and ^{244}Cm for each axial location of the normal and low enriched fuel rods and GBFs in the Type-1 and -2 fuel assembly are shown in Figure 33 and Figure 34. The radial distributions for the low and normal enriched fuel rods show similar trend to the results in the Type-0 fuel assembly case. However, the different shape of distribution can be observed in the radial Pu distribution for GBFs after 3cycles depletion. The highest mass density of Pu for GBFs are at the surface mesh. However, it dramatically decreases during second to fifth meshes from the surface. Then, it increases a little bit. In order to discuss on occurring this well shape distribution near the surface of high burnup GBFs, the radial distributions for two dominant reactions, the capture reaction of ^{238}U and the fission reaction rate of ^{239}Pu, are plotted in Figure 35. The capture reaction rate of ^{238}U dramatically decreases at the second mesh from the surface of GBF, however, the fission reaction rate of ^{239}Pu slightly decreases at the same location. That means that the production of ^{239}Pu is not relatively active at the second mesh from the surface, even though the consumption of ^{239}Pu is relatively active at that location. The fission reaction of ^{239}Pu is dominant with thermal neutrons, whereas that the capture reaction of ^{238}U is dominant with epithermal neutrons. The most of epithermal neutrons are captured in ^{238}U at the surface, however, thermal neutrons can travel a little deeper from the surface than epithermal neutrons, because the capture cross section of ^{238}U for thermal neutrons is smaller than that for epithermal neutrons. That alive thermal neutrons are absorbed in ^{239}Pu, and fission occurs. The higher concentration of ^{239}Pu leads greater reaction rate, therefore, the fission reaction of ^{239}Pu near the surface region is more active in GBFs after 3 cycle depletion than that after 1 or 2 cycles depletion. Therefore, the well shape distribution near the surface can be observed the result of GBF after 3cycles depletion.

Finally, the radial and axial non-uniformity of nuclide composition in spent fuel assemblies can be approximately achieved by decoupling between the result of axial and radial distributions as explained in Section 2.3.2.

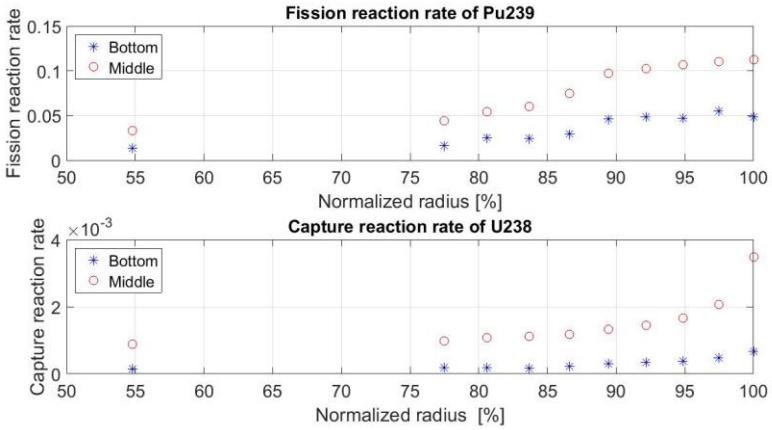

Figure 35 The radial distribution for the fission reaction rate of ^{239}Pu (top) and the capture reaction rate of ^{238}U (bottom) at the bottom (a star mark with the blue color) and middle (a circle mark with the red color) of GBF in the axial direction.

3.3 Statistical analysis for non-uniformity of nuclide composition in pyroprocess

3.3.1 Probabilistic distributions for Pu and ^{244}Cm concentrations in head-end process

3.3.1.1 Chopping process

The histograms of Pu (top) and ^{244}Cm (bottom) mass density in the chopped pieces 1-cm in length for the Type-0 (1st column), -1 (2nd column), and -2 (3rd column) fuel assemblies after 1 (blue bar), 2 (black bar), and 3 (red bar) cycles depletion are plotted in Figure 36. The statistical results of those is summarized in Table 16. First, the high peak bars are generated by the large size, 60.5 cm, of mesh for the middle of fuel rods, because it is assumed that the concentration within that large single mesh is uniform. In addition, the difference of mass densities between that largest mesh and adjacent meshes are smaller than that between the largest mesh and the top and bottom meshes. Second, the height of peaks, which represents the normalized frequency, decreases as increasing burnup. This would be caused by decreasing the axial non-uniformity of nuclide composition generally as increasing burnup as mentioned in the previous Section, if there is no GBFs in the spent fuel assembly. However, the increasing depletion cycles from 2 to 3 cycles for assemblies including GBFs shows increasing non-uniformity of Pu. Furthermore, the number of GBFs in the assembly could proportionally increase the non-uniformity of Pu and ^{244}Cm by comparing between the results of Type-1 and -2 fuel assembly. Third, the axial non-uniformity of ^{244}Cm is more significant than that of Pu. Fourth, the histograms for ^{244}Cm mass density for assemblies after 1 cycle depletion is invisible, because the mass density of ^{244}Cm of that is relatively smaller than the ^{244}Cm in assemblies after 2 and 3cycles depletion.

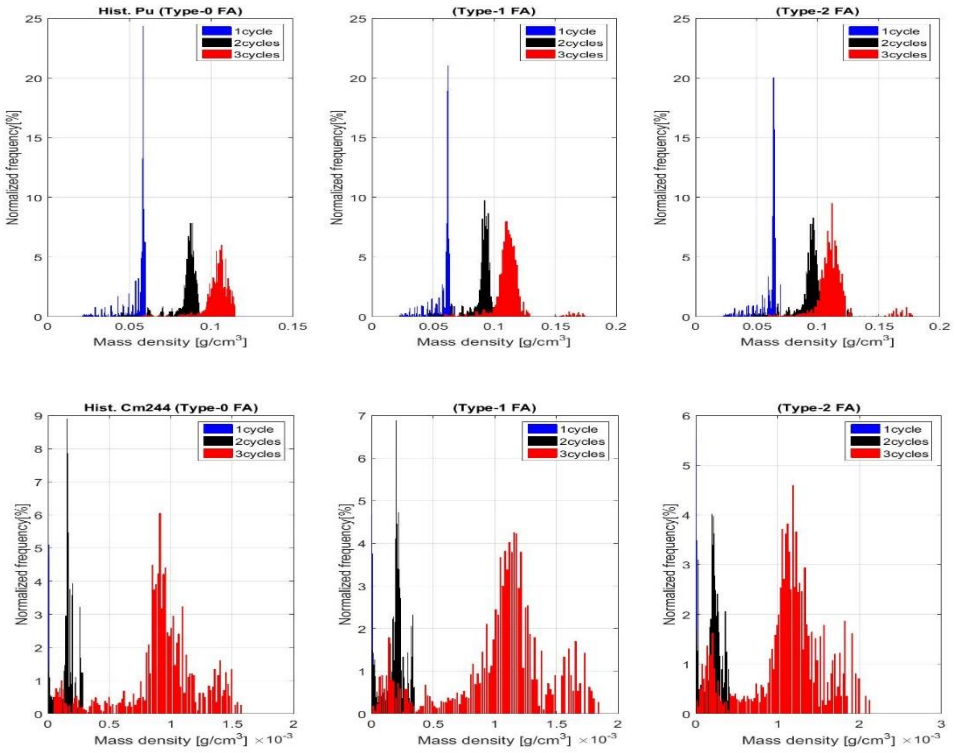

Figure 36 Histograms of Pu (top) and ^{244}Cm (bottom) mass density for the Type-0 (1st column), -1 (2nd column), and -2 (3rd column) fuel assemblies after 1 (blue bar), 2 (black bar), and 3 (red bar) cycles depletion.

Table 16 Statistical results for Pu and ^{244}Cm mass density histograms of chopped pieces for Type-0, -1, and -2 fuel assembly (SD: standard deviation, and CV: coefficient of variance).

FA Type	Depletion cycle	Pu mass density			^{244}Cm mass density		
		Mean [g/cm^3]	SD [g/cm^3]	CV [%]	Mean [g/cm^3]	SD [g/cm^3]	CV [%]
0	1	5.45E-02	7.98E-03	14.6	5.52E-06	2.95E-06	53.4
	2	8.49E-02	8.22E-03	9.68	1.60E-04	6.54E-05	40.9
	3	1.04E-01	8.42E-03	8.12	9.28E-04	3.17E-04	34.2
1	1	5.81E-02	8.69E-03	15.0	6.96E-06	3.95E-06	56.8
	2	9.09E-02	1.02E-02	11.2	1.89E-04	8.44E-05	44.7
	3	1.12E-01	1.33E-02	11.9	1.05E-03	4.02E-04	38.4
2	1	5.98E-02	9.05E-03	15.1	7.82E-06	4.72E-06	60.3
	2	9.39E-02	1.12E-02	12.0	2.06E-04	9.90E-05	48.1
	3	1.12E-01	1.54E-02	13.7	1.11E-03	4.62E-04	41.6

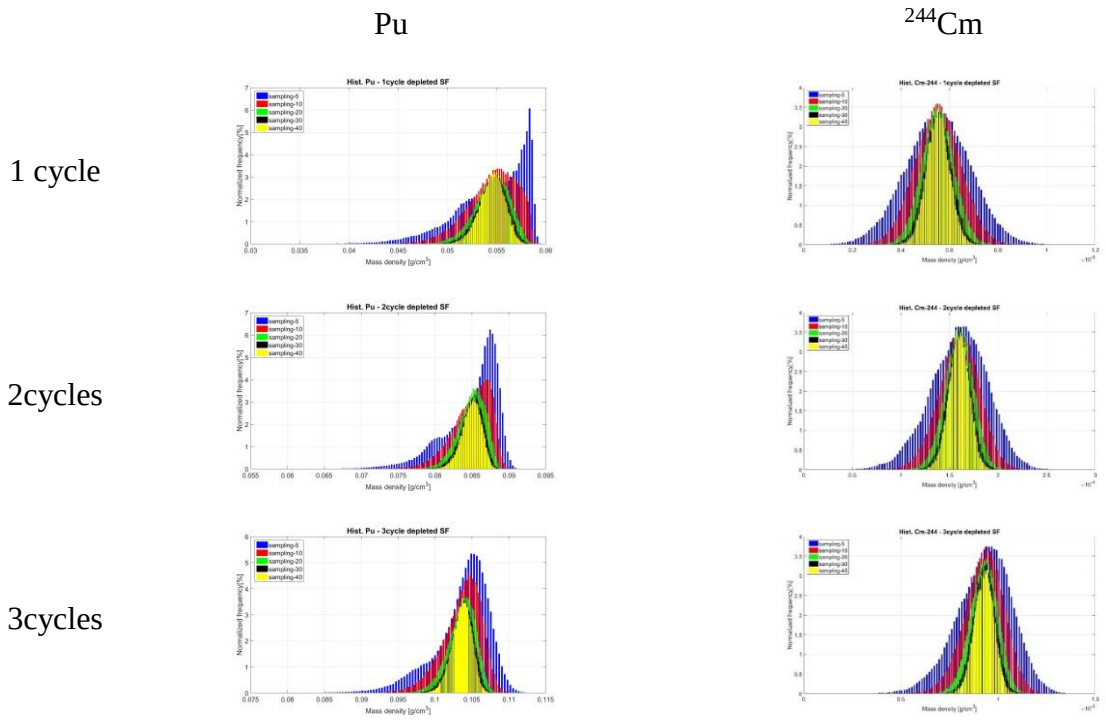

Figure 37 Histogram for sample means of chopped pieces using the simulation result of Type-0 fuel assembly (sample size 5: blue bar, 10: red bar, 20: green bar, 30: black bar, 40: yellow bar).

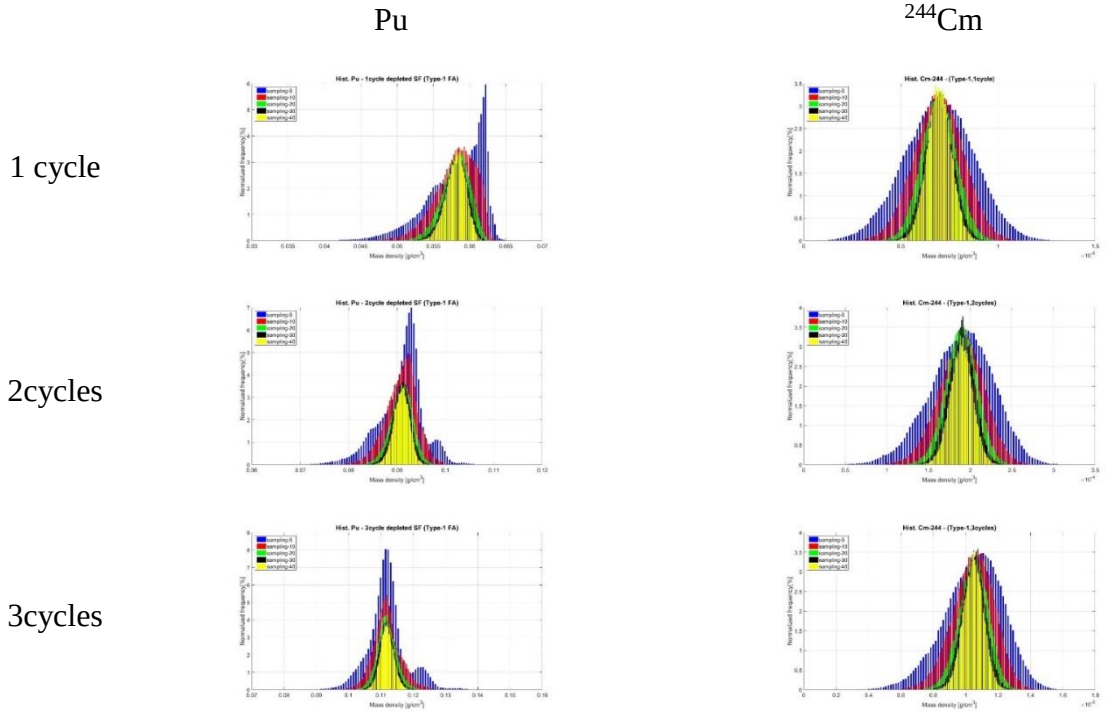

Figure 38 Histogram for sample means of chopped pieces using the simulation result of Type-1 fuel assembly (sample size 5: blue bar, 10: red bar, 20: green bar, 30: black bar, 40: yellow bar).

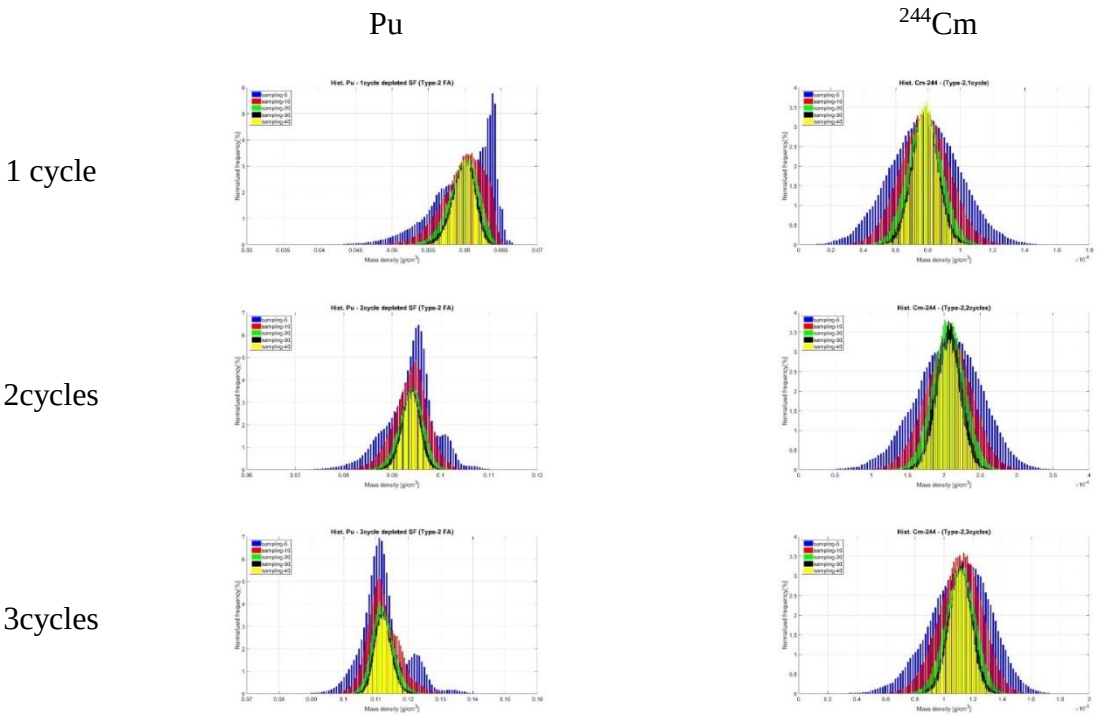

Figure 39 Histogram for sample means of chopped pieces using the simulation result of Type-2 fuel assembly (sample size 5: blue bar, 10: red bar, 20: green bar, 30: black bar, 40: yellow bar).

Table 17 Coefficient of variance for random sampling results.

FA Type	depletion cycle	Sample size									
		Pu [%]					^{244}Cm [%]				
		5	10	20	30	40	5	10	20	30	40
0	1	6.53	4.63	3.26	2.68	2.32	23.9	16.9	11.9	9.74	8.40
	2	4.33	3.06	2.17	1.77	1.54	18.3	13.0	9.15	7.52	6.48
	3	3.64	2.56	1.82	1.48	1.28	15.3	10.8	7.65	6.22	5.39
1	1	6.69	4.74	3.36	2.72	2.35	25.4	17.9	12.8	10.4	8.93
	2	5.04	3.55	2.53	2.06	1.77	20.0	14.1	9.98	8.13	7.08
	3	5.30	3.74	2.65	2.16	1.88	17.1	12.2	8.56	7.00	6.04
2	1	6.76	4.79	3.39	2.75	2.37	27.0	19.0	13.5	11.0	9.49
	2	5.36	3.78	2.68	2.19	1.88	21.5	15.2	10.7	8.74	7.65
	3	6.13	4.33	3.05	2.50	2.17	18.6	13.2	9.29	7.59	6.55

The histograms of sample means for Pu (1st column) and ^{244}Cm (2nd column) mass density with various sample sizes (5: blue bar, 10: red bar, 20: green bar, 30: black bar, 40: yellow bar) for the Type-0, -1, and -2 spent fuel assemblies after 1, 2, and 3cycles depletion are respectively shown in Figure 37, Figure 38, and Figure 39. The coefficient of variance for all cases is summarized in Table 17. As mentioned in the previous Section, it is necessary to test the normality of data to evaluate material accountancy, because the probability of Type-I error for the MUF, which is the performance metric is, can be calculated based on the random variable, MUF, following the normal distribution as mentioned in the methodology Section. In order to discuss the normality of data, the two normality methods, the Q-Q plot as a graphical method and JB test as a statistical method, are applied. First, the Q-Q plots for various sampling cases are shown in Figure 40, Figure 41, and Figure 42. Each cell includes 5 Q-Q plots. The sample size for the Q-Q plot shown in the top left each cell is 5. The top middle is the Q-Q plot when sample size is 10. The Q-Q plot for 20 sample size case is shown the top right. The bottom left and middle are the Q-Q plots when sample sizes are 30 and 40, respectively. Each plot shows the diagonal red dot line as a reference index and the thick blue line evaluated based on the obtained data. The linearity of the blue line along the red reference dot line means that the obtained data are normally distributed. First, we can see the blue lines are getting close to the red linear line as increasing the sample size for all cases. Second, the sample mean data for ^{244}Cm by the random sampling method would be more normally distributed than that for Pu, particularly, the small sample size cases. Even though the normality could be visually discussed, the quality for normality would not be assured. Hence, the normality test has been applied by the JB test as a statistical method. The skewness (circle mark), kurtosis (cross mark), and the JB test values (x mark) for Pu (1st column) and ^{244}Cm (2nd column) of Type-0, -1, and -2 fuel assemblies depleted 1cycle (red), 2 cycles (blue), and 3 cycles (black) with respect to the sample size (x-axis) have been plotted in Figure 43. The skewness of data is a measure of asymmetry for a histogram. The negative value of that means the left-side tail of histogram is longer than the right-side tail. The positive value is the opposite case of the negative value. The zero skewness means a symmetric histogram. The kurtosis for normal distribution is three. Therefore, as the value of skewness and kurtosis approach zero and three, it can be said the data is more normally distributed. Based on this, we can observe that the skewness and kurtosis are close to zero and three by increasing the sample size. The normality test is finally conducted by comparing between evaluated JB test values shown in Table 18 and the 5% and 10% significant levels shown in Table 10 depending on the sample size. The values evaluated by the JB test for the obtained data are smaller than the 5% significant levels, when the sample size is greater than 20. It would not be available to obtain significant levels when the sample sizes are 5 and 10, however, we could see the JB values for those cases are small. By this observation, we could accept that the obtained data by the random sampling method after the chopping process are normally distributed at least the sample size is great than 20. However, the coefficient of variance for Pu and ^{244}Cm mass densities for all random sampling cases would not be in the range of acceptance. It could be concluded the random sampling to evaluate the Pu-to-^{244}Cm-ratio after the chopping process is not appropriate due to a large uncertainty of Pu and ^{244}Cm mass densities in samples.

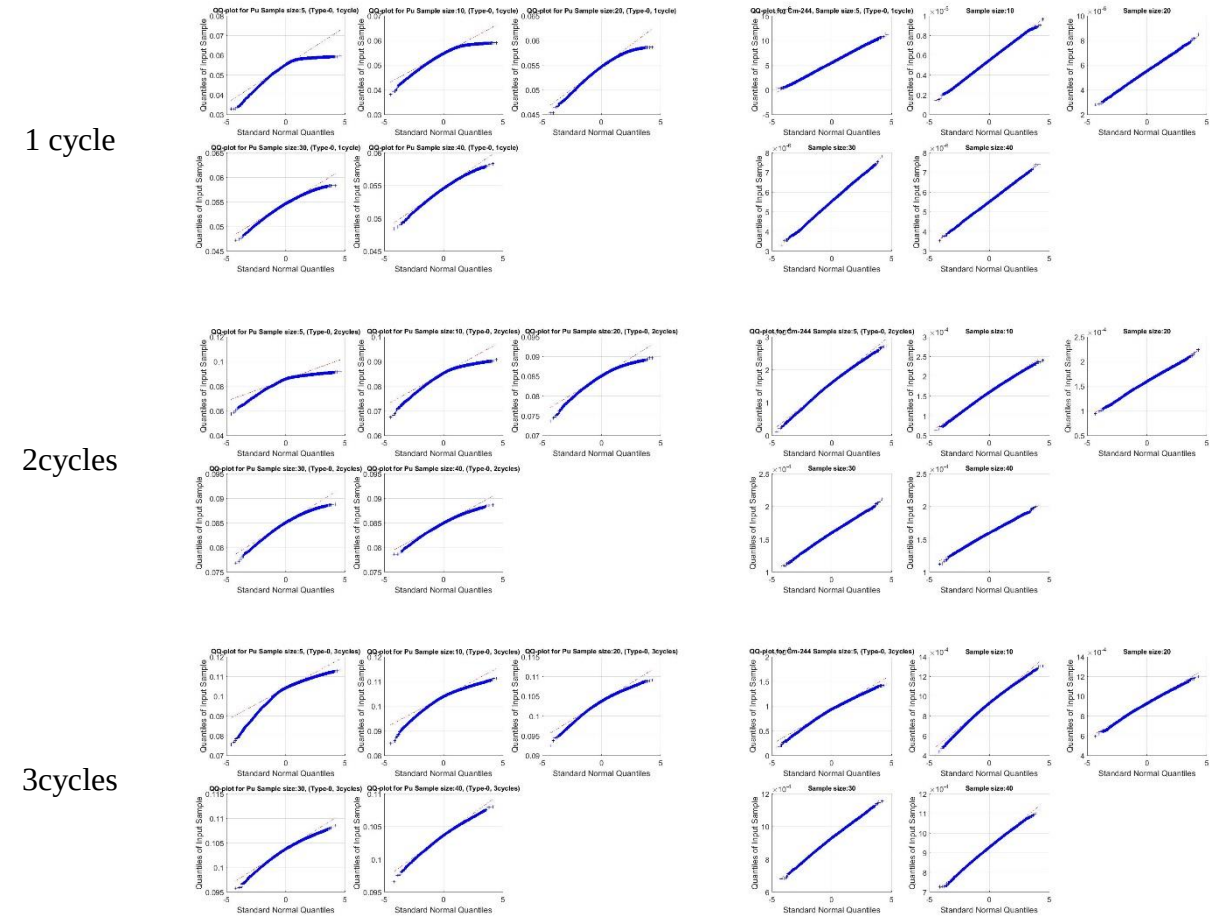

Figure 40 Q-Q plots for the sample size 5 (top left), 10 (top middle), 20 (top right), 30 (bottom left), and 40 (bottom middle) using the simulation results of the Type-0 fuel assembly after 1, 2, and 3 cycles depletion.

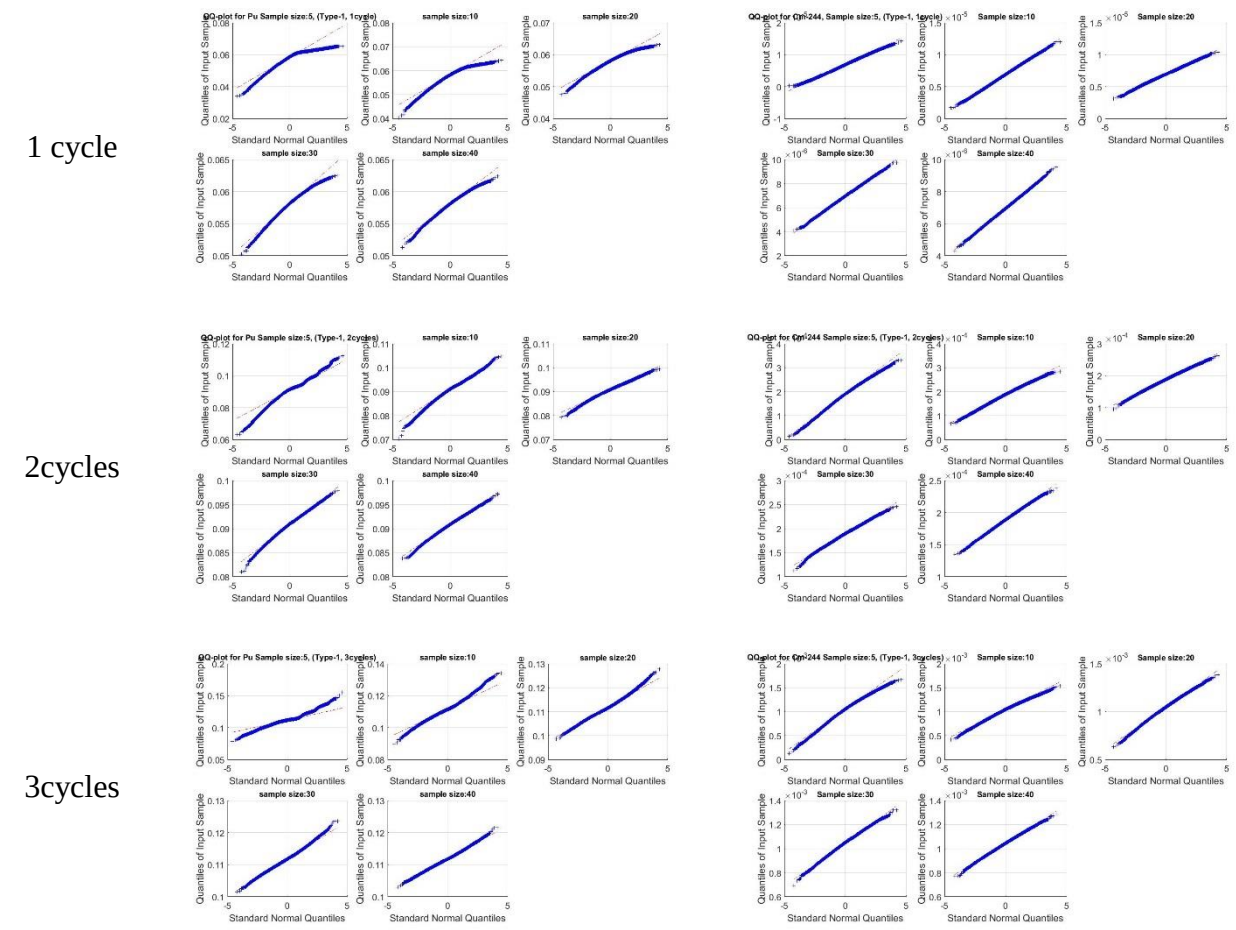

Figure 41 Q-Q plots for the sample size 5 (top left), 10 (top middle), 20 (top right), 30 (bottom left), and 40 (bottom middle) using the simulation results of the Type-1 fuel assembly after 1, 2, and 3 cycles depletion.

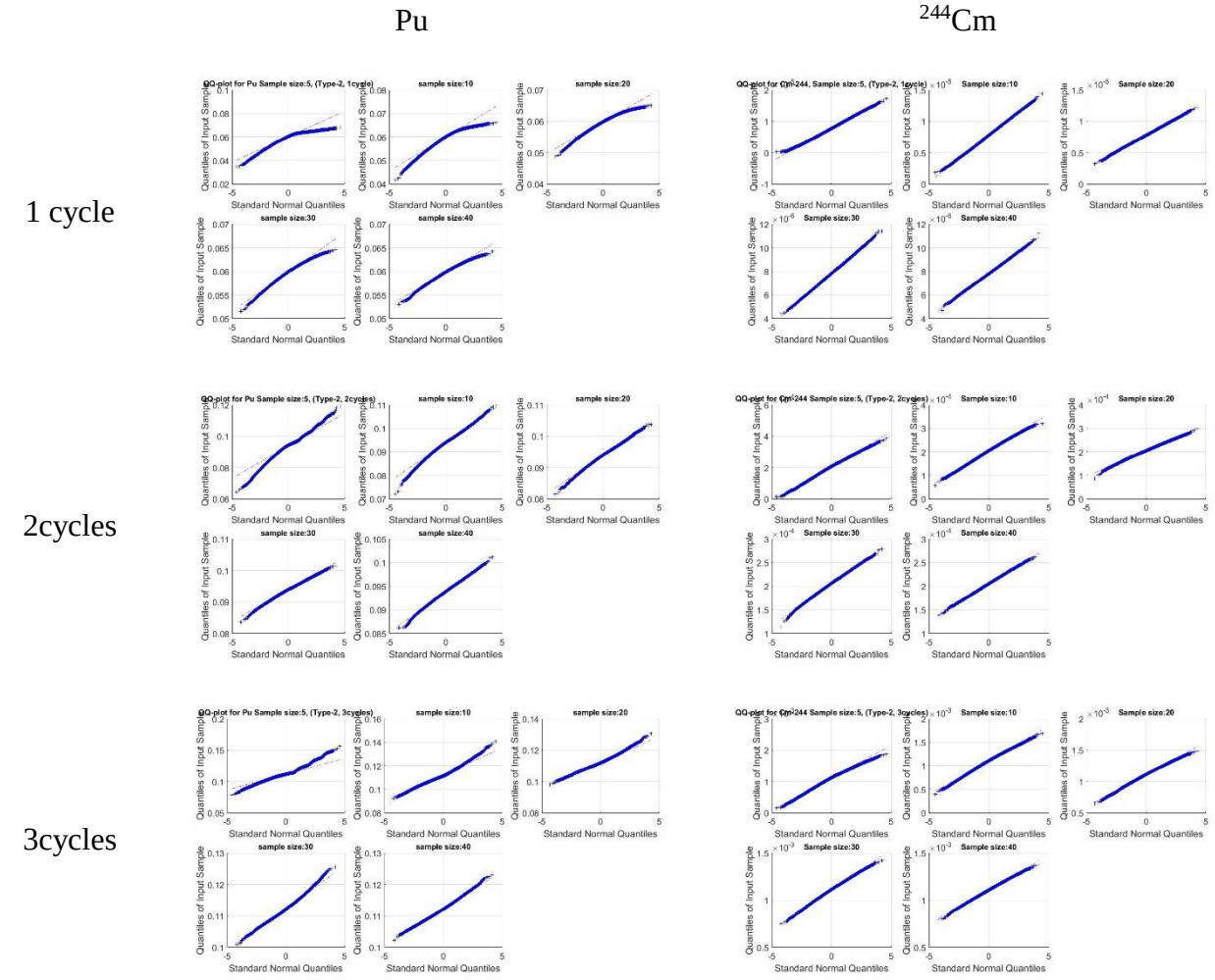

Figure 42 Q-Q plots for the sample sizes, 5 (top left), 10 (top middle), 20 (top right), 30 (bottom left), and 40 (bottom middle) using the simulation results of the Type-2 fuel assembly after 1, 2, and 3 cycles depletion.

FA Type	Pu	^{244}Cm
0	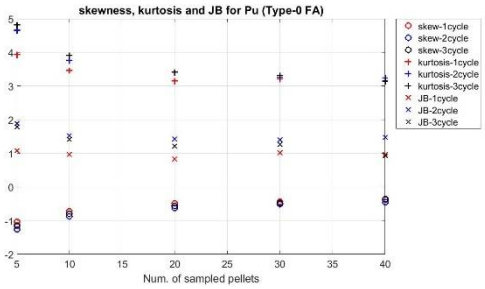	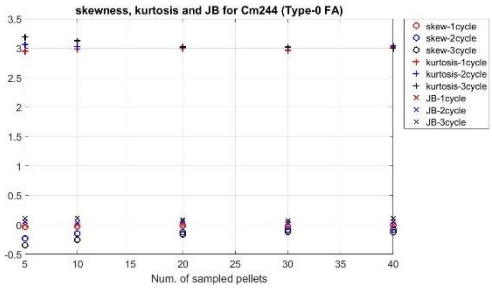
1	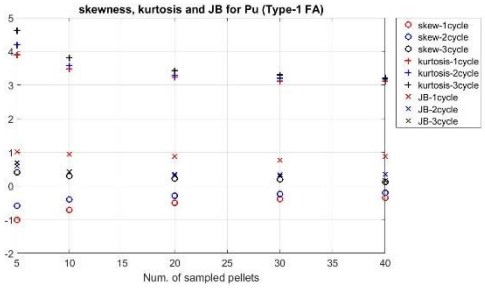	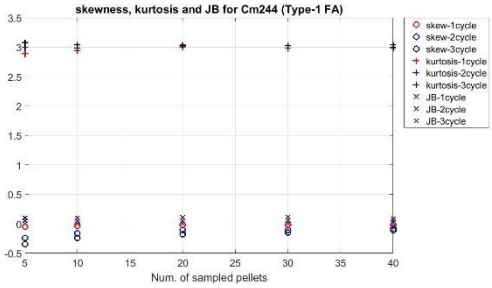
2	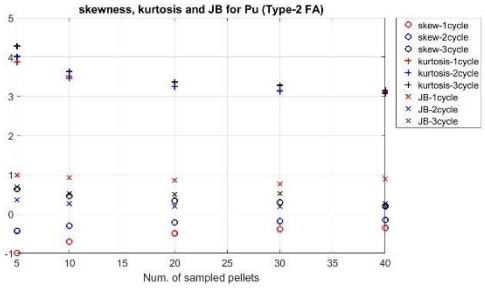	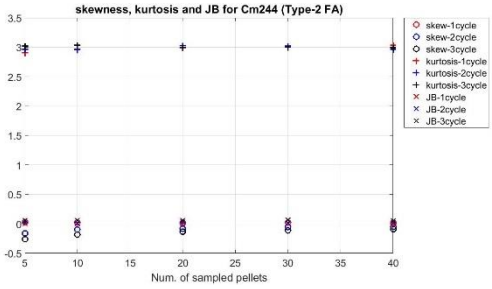

Figure 43 Skewness (circle mark), kurtosis (cross mark), and JB (x mark) test results for Pu (1st column) and ^{244}Cm (2nd column) sample means of Type-0 (1st row), -1 (2nd row), -2 (3rd row) fuel assemblies by the random sampling (red: 1cycle, blue: 2cycles, and black: 3 cycles depletion).

Table 18 JB test results for the random sampling of chopped pieces.

FA Type	depletion cycle	Sample size									
		Pu					^{244}Cm				
		5	10	20	30	40	5	10	20	30	40
0	1	1.07	0.96	0.83	1.01	0.97	0.00	0.00	0.00	0.00	0.00
	2	1.89	1.52	1.43	1.40	1.47	0.05	0.04	0.06	0.04	0.05
	3	1.78	1.42	1.21	1.26	0.92	0.11	0.11	0.09	0.07	0.11
1	1	1.01	0.94	0.88	0.77	0.87	0.00	0.00	0.00	0.00	0.01
	2	0.59	0.41	0.35	0.34	0.35	0.05	0.04	0.04	0.06	0.05
	3	0.69	0.42	0.31	0.29	0.16	0.10	0.10	0.11	0.11	0.09
2	1	0.99	0.92	0.86	0.77	0.89	0.00	0.00	0.00	0.00	0.00
	2	0.36	0.26	0.20	0.19	0.19	0.02	0.02	0.03	0.02	0.02
	3	0.69	0.51	0.50	0.52	0.27	0.06	0.06	0.06	0.06	0.05

3.3.1.2 Voloxidation

After taking into account the radial non-uniformity for each chopped piece, the Pu and ^{244}Cm concentration data after the chopping process can be appropriately converted into the data for the voloxidation process. The histograms for Pu and ^{244}Cm mass densities in powders are plotted for three different fuel assembly types and three different depletion schemes as shown in Figure 44. Their statistical results are summarized in Table 19. Visually, a major difference between the distributions after the chopping and voloxidation process is the direction of tails. The histograms for the product of chopping process show the left-side tail, because the large number of chopped pieces originally located at the middle of fuel rods show the great mass density, whereas the relatively small number of pieces located at the top and bottom of fuel rods show low mass density. The trend has changed by the radial non-uniformity. The radial non-uniformity shows the great mass density at the perimeter region, approximately, one to three meshes from the surface of fuel rods in the radial direction, and the small mass density in the rest of radial meshes. Therefore, the direction of long tail changes to the right-hand side as shown in Figure 44. Furthermore, the coefficient of variance of Pu and ^{244}Cm for the chopped pieces can be escalated by taking into account radial non-uniformities of each piece in all representative spent fuel assemblies as shown in Table 16 and Table 19.

Table 19 Statistical results for Pu and ^{244}Cm mass density for powders after the voloxidation process.

FA Type	Depletion cycle	Pu mass density			^{244}Cm mass density		
		Mean [g/cm^3]	SD [g/cm^3]	CV [%]	Mean [g/cm^3]	SD [g/cm^3]	CV [%]
0	1	5.45E-02	2.05E-02	37.7	5.52E-06	4.13E-06	74.9
	2	8.49E-02	2.88E-02	33.9	1.60E-04	1.04E-04	65.1
	3	1.04E-01	3.20E-02	30.9	9.28E-04	5.58E-04	60.2
1	1	5.81E-02	2.22E-02	38.2	6.96E-06	5.44E-06	78.2
	2	9.09E-02	3.15E-02	34.6	1.89E-04	1.30E-04	68.6
	3	1.12E-01	3.62E-02	32.4	1.05E-03	6.68E-04	63.7
2	1	5.98E-02	2.30E-02	38.5	7.82E-06	6.39E-06	81.7
	2	9.39E-02	3.28E-02	35.0	2.06E-04	1.47E-04	71.6
	3	1.12E-01	3.72E-02	33.2	1.11E-03	7.38E-04	66.4

FA ype Pu ^{244}Cm

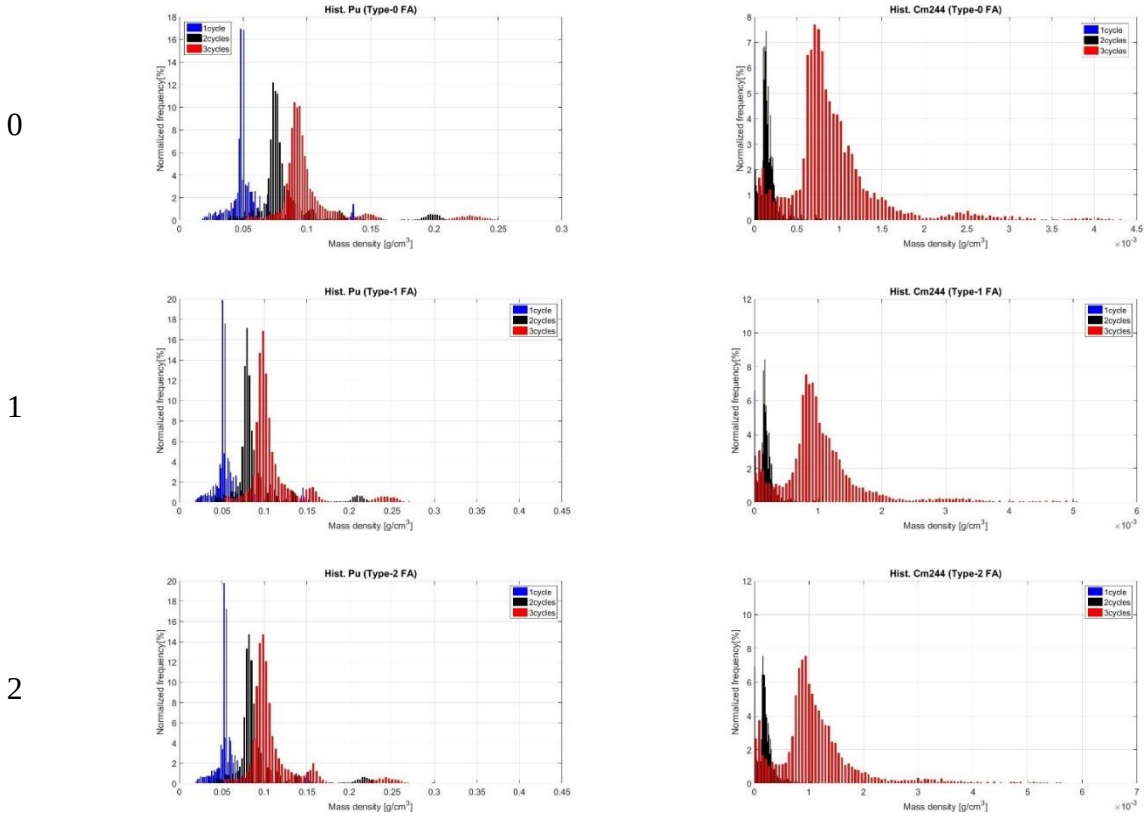

Figure 44 Histograms of Pu (1st column) and ^{244}Cm (2nd column) mass densities in powders for the Type-0 (1st row), -1 (2nd row), and -2 (3rd row) fuel assemblies after 1 (blue bar), 2 (black bar), and 3 (red bar) depletion cycles.

3.3.1.3 Granulation

The single granule in the pretreatment process is made of multiple powders after the voloxidation process. Even though the size of powder and granule in the product of processes are varied, it is assumed that the size of spherical powders and granules are identical, respectively. If the sizes of powder and granule are determined, a number of powder particles to be the single granule can be evaluated. Then, that number would be applied as a sample size for one granule. As mentioned in the previous, the range of size for powders and granules are the μm and mm scale, respectively. Therefore, the sample size (n) could be a large number so that the central limit theorem is applied as shown below,

$$\sigma_{\text{Pu or }^{244}\text{Cm in one granule}} = \frac{\sigma_{\text{Pu or }^{244}\text{Cm in total powders}}}{\sqrt{\text{Sample size (number of powders in a granule)}}}, \qquad (3.17)$$

where $\sigma_{\text{Pu or }^{244}\text{Cm in total powders}}$ is the standard deviation of Pu or ^{244}Cm for all powders after voloxidation, and $\sigma_{\text{Pu or }^{244}\text{Cm in one granule total}}$ is the standard deviation of Pu or ^{244}Cm for sampling of the single granule. In this study, the range of radius for powder and granule are 10 to 100μm and 0.5 to 3mm. Using this, the mean and standard deviation of Pu and ^{244}Cm for sampling of the single granule can be evaluated. The results of that are shown by the contour plot for the coefficient of variance [%] which is evaluated by the standard deviation to the mean of a random variable (Pu and ^{244}Cm mass density) as shown in Figure 45, Figure 46, and Figure 47. The x- and y-axis are the radius of granule and powder, respectively. First, the CV of Pu and ^{244}Cm mass density is increasing as increasing the powder size and decreasing the granule size, because the number of powder particles in the single granule is getting decreased. Second, the more significant non-uniformity of ^{244}Cm mass density in chopped pieces and powders than that of Pu continuously leads the greater CV for ^{244}Cm in the granule than that for Pu. The CV for ^{244}Cm and Pu are less than 8% and 4%. The CVs can decrease by increasing the number of granule sample. Since the non-uniformity becomes less significant as increasing burnup, the CV is generally decreasing as increasing depleted cycles.

cycle	Pu	^{244}Cm
1	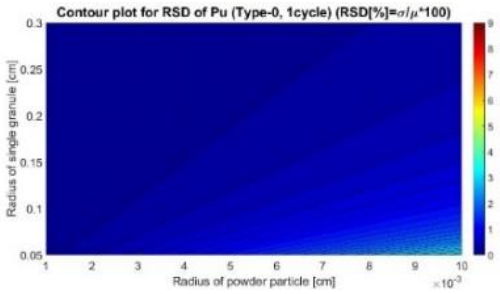	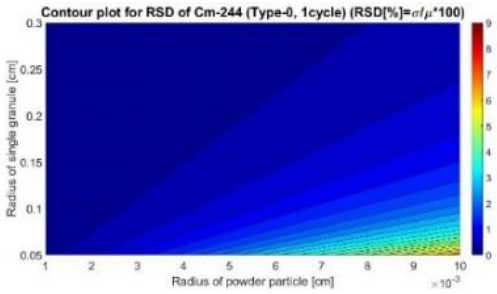
2	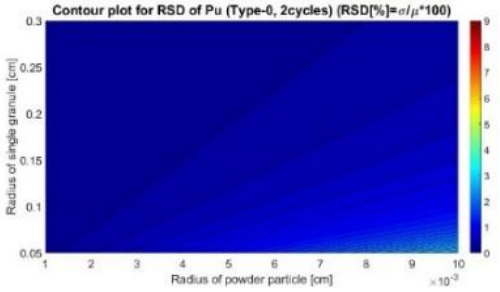	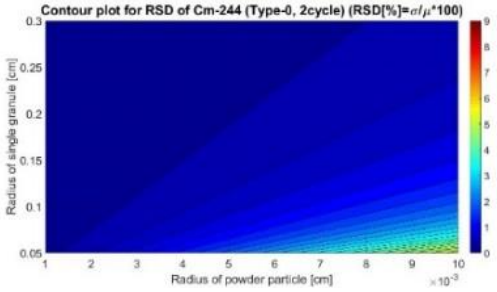
3	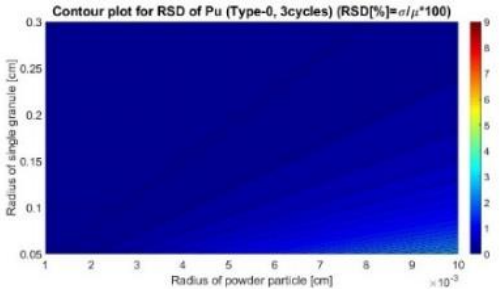	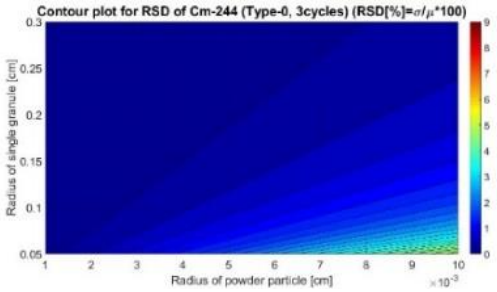

Figure 45 Coefficient of variance for Pu (1st column) and ^{244}Cm (2nd column) in the single granule sampled from the Type-0 fuel assembly after 1, 2, and 3 cycles depletion.

cycle	Pu	^{244}Cm
1	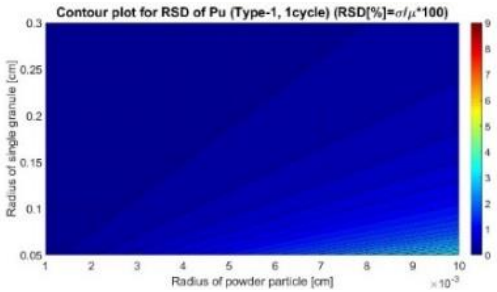	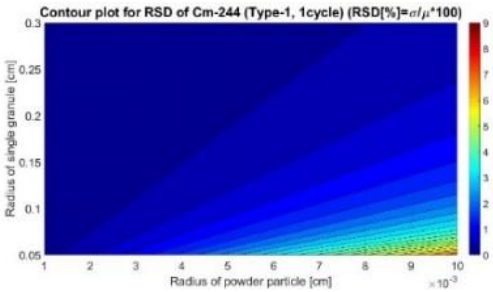
2	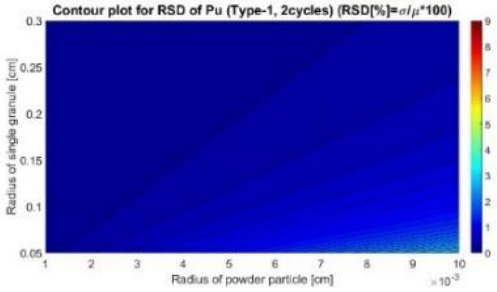	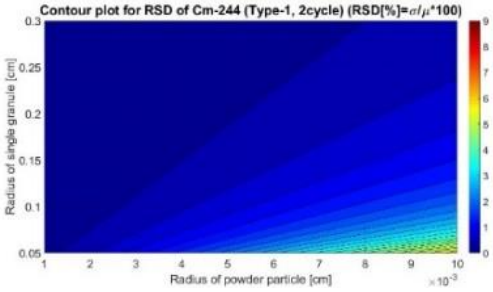
3	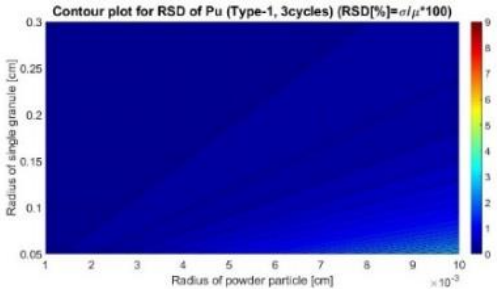	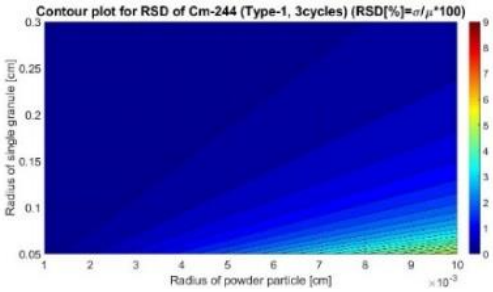

Figure 46 Coefficient of variance for Pu (1st column) and ^{244}Cm (2nd column) in the single granule sampled from the Type-1 fuel after 1, 2, and 3 cycles depletion.

cycle Pu ^{244}Cm

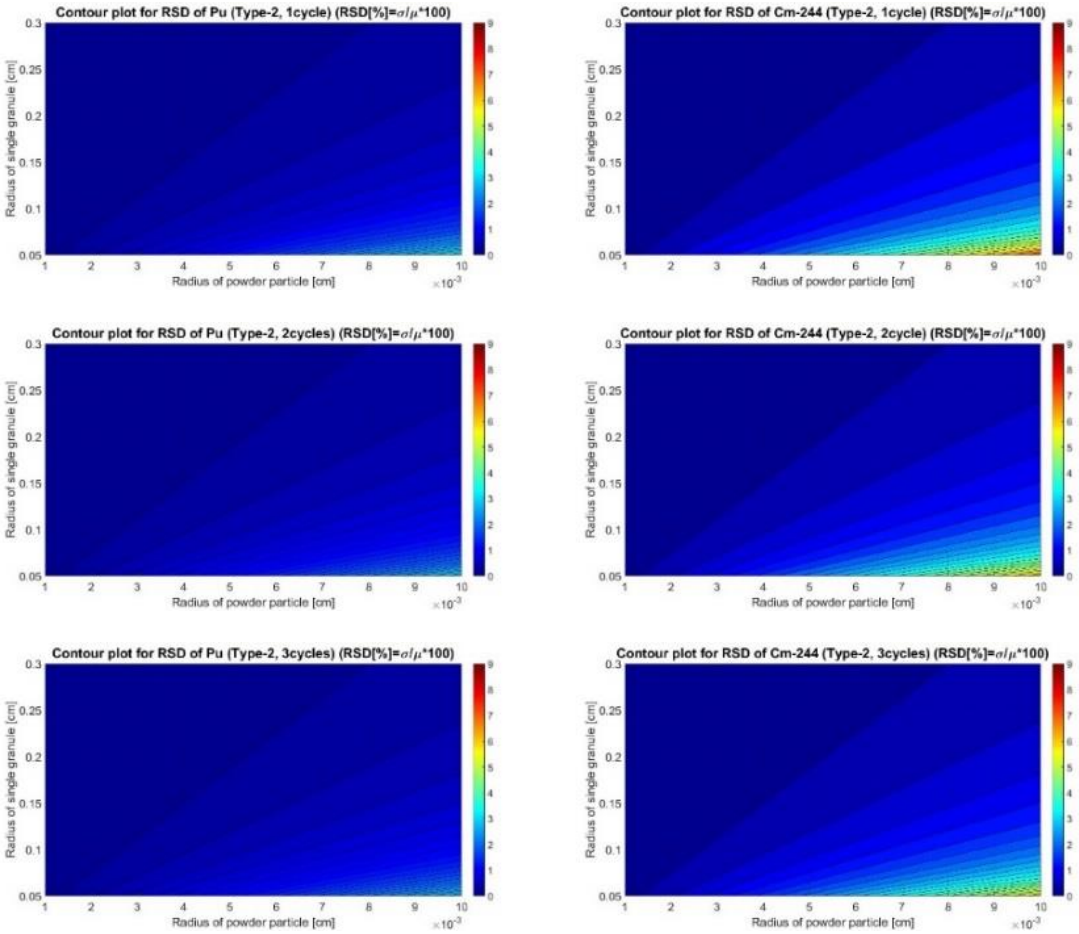

Figure 47 Coefficient of variance for Pu (1st column) and ^{244}Cm (2nd column) in the single granule sampled from the Type-2 fuel assembly depleted after 1, 2, and 3 cycles depletion.

These results are substituted into the formulation for the GH transformation shown in Eq. 2.8. By that, the statistical mean for the random variable, the Pu-to-^{244}Cm-ratio, which is approximately following the normal distribution can be achieved as shown in Figure 48. Because the range of ratios depending on the fuel assembly type and depletion cycle lengths is remarkably varied, the scale of the colormap in contour plots are different for each plot.

The true ratios for the Type-0 assembly depleted 1, 2, and 3 cycles are 9880, 532, and 112, respectively. The maximum ratios evaluated by the GH transformation are 11500, 594, and 123. The difference from the true value is around 16.0%, 11.6%, and 9.77% when the radius of granule and powder are 0.5 mm and 100 μm. The maximum difference of ratios for the Type-1 fuel assembly shows 17.7%, 13.1%, and 11.1% for the 1, 2, and 3cycles depletion cases. In the simulation case for the Type-2 fuel assembly, the maximum difference of ratios is 19.7%, 14.4%, and 12.2% with respect to 1, 2, and 3cycles depletion scheme. In contrast, when the large size of single granule consisting of small size powders is taken as a sample to evaluate the ratio, the

evaluated ratio shows very good agreement with the true ratio, for example, the red color area in Figure 48. The difference between the calculated and true ratio has increased as decreasing the depletion length and as increasing number of loaded GBFs in the assembly. As shown in the previous statistical results, the non-uniformity represented by a standard deviation of ^{244}Cm is more significant than that of Pu in every process stages, therefore, the uncertainty for evaluating the ratio is strongly affected by the ^{244}Cm non-uniformity in spent fuel assemblies.

Based on the difference of ratii, we can calculate a number of assemblies to be 1SQ Pu (8 kg) difference between the true and evaluated Pu mass. The results of that is plotted in Figure 49. In this calculation, the uncertainty of ^{244}Cm mass measuring by a neutron counting rate is neglected to focus on the influence of non-uniformity in determination of the ratio. The colormap on the log10 scale is applied, for example, the orange color region (1 in the index of the colormap) means that there is possibility we can meet the 1 SQ Pu difference after processing of 10 fuel assemblies. According the KAPF+ conceptual mode [11], the around 4.6 assemblies is treated per a day. Therefore, it would be claimed that the sampling should be carefully conducted to establish material accountancy for pyroprocess, even though the current analysis is based on the single granule as a sample as a conservative case.

FA Type	1 cycle	2 cycles	3 cycles
0	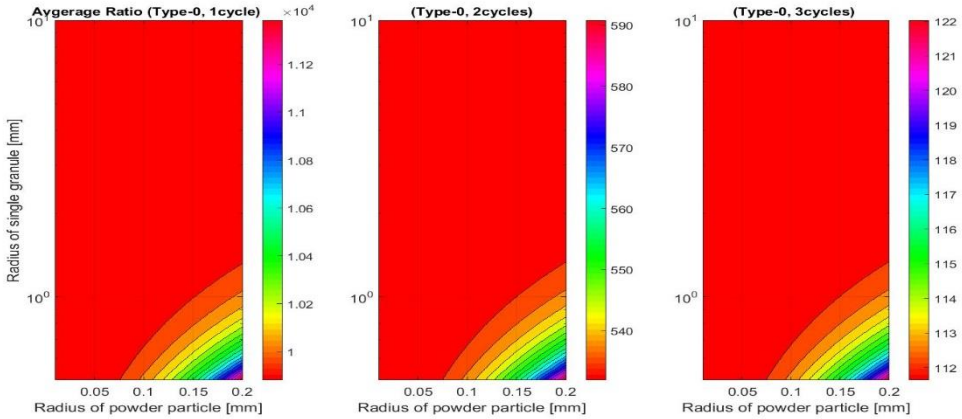		
1	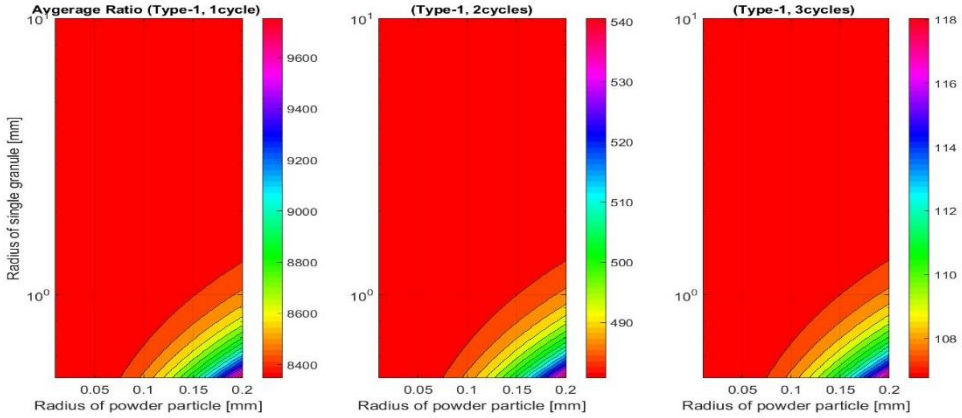		
2	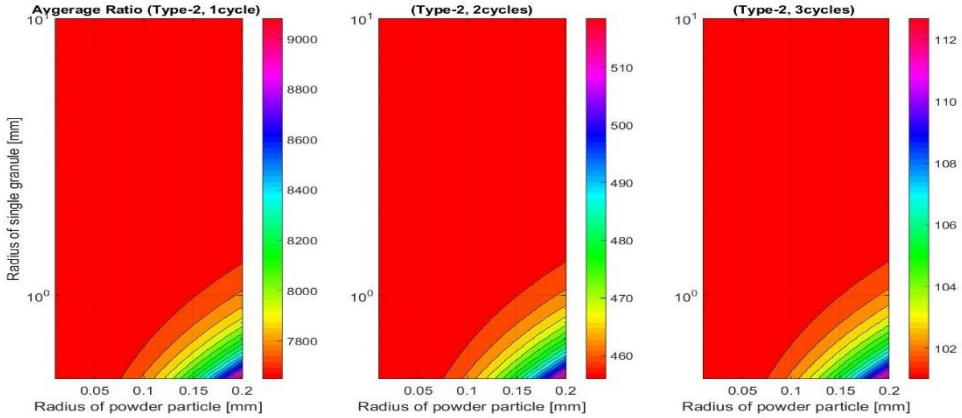		

Figure 48 Evaluated Pu-to-^{244}Cm-ratios by the GH transformation for the Type-0 (1st row), -1 (2nd row), and -2 (3rd row) fuel assemblies after 1 (1st column), 2 (2nd column), and 3 (3rd column) cycles depletion.

FA Type	1 cycle	2 cycles	3 cycles
0	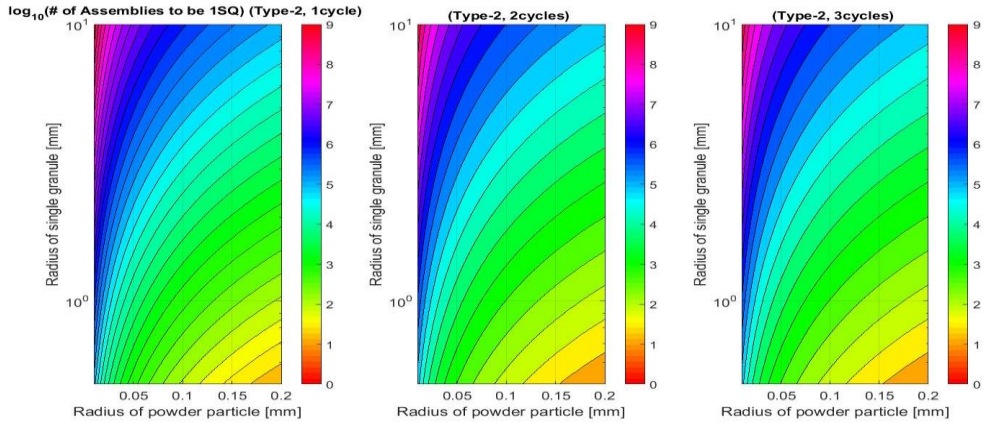		
1	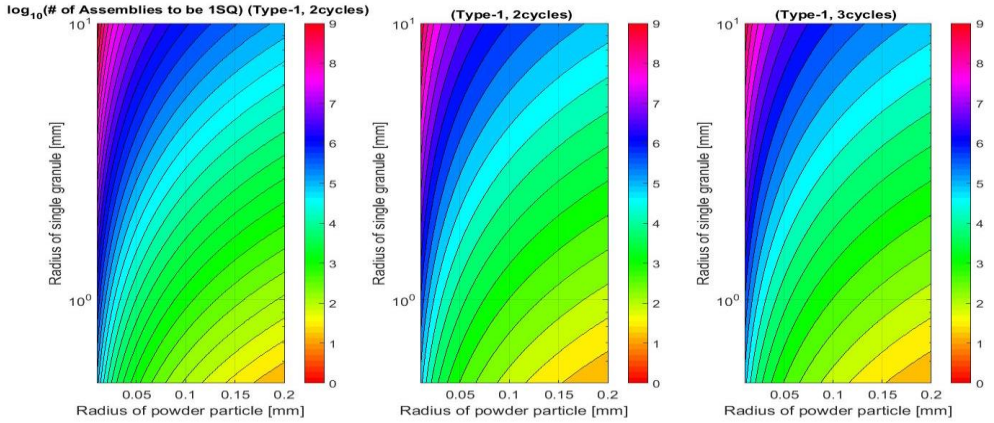		
2	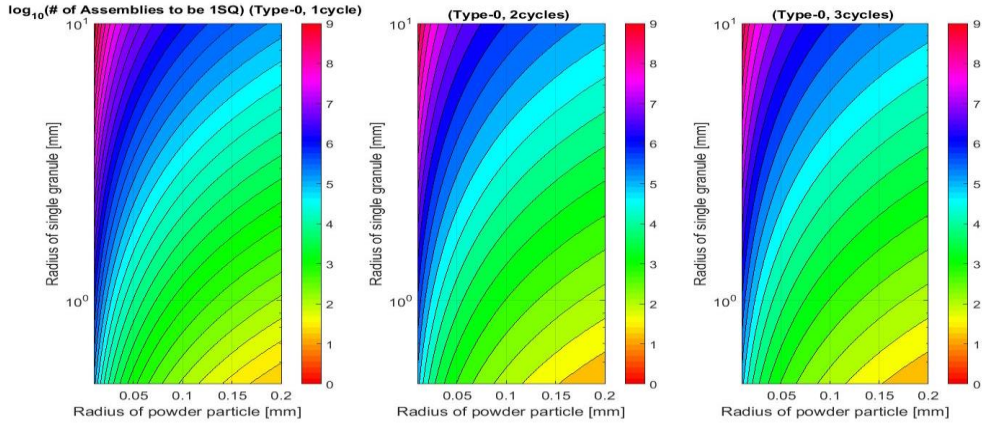		

Figure 49 Number of assembly necessary for the difference of Pu between the evaluated Pu and the true Pu to be 8kg (1SQ) for the Type-0 (1st row), -1 (2nd row), and -2(3rd row) fuel assemblies after 1 (1st column), 2 (2nd column), and 3 (3rd column) cycles depletion.

3.3.2 Error propagation through key-pyroprocess

In this section, the propagation of uncertainty for determing the ratio through the key-pyroprocess system is evaluated using the MUF. The MBA considered in this study is the key-pyroprocess. The feed for that is the product of the head-end process, granules. The KMPs for the system are the feed and the dross of the electrolytic-reduction process, the U-deposit at the cathod of the electro-refining, the TRUs in the LCC and the salts from the electro-winning process as shown in Figure 50.

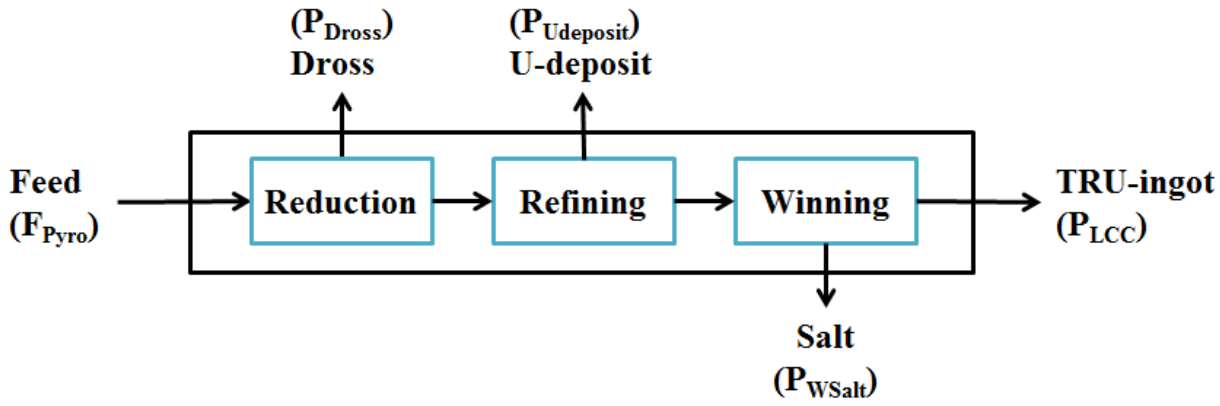

Figure 50 Schematic layout for MBA of key-pyroprocess.

Based on this MBA, the MUF in Eq. 2.10 can be revised as below,

$$MUF_{Pyro} = (F_{Pyro}) - (P_{Dross}) - (P_{Udeposit}) - (P_{LCC}) - (P_{WSalt}), \tag{3.18}$$

where MUF_{Pyro} is the MUF for the key-pyroprocess, F_{pyro} is the feed into the key-pyroprocess, P_{Dross} is the dross from the electrolytic-reduction process, $P_{Udeposit}$ is the product at the cathod which is the U-deposit in the electro-refining process, P_{LCC} is the product in the LCC, and P_{WSalt} is the waste product from the electro-winning process. All parameters are random variables due to all measured values. The expectation (E) and the standard deviation (σ) of MUF for the key-pyrprocess can be fomulated as below,

$$E[MUF_{Pyro}] = E[F_{pyro}] - E[P_{Dross}] - E[P_{Udeposit}] - E[P_{LCC}] - E[P_{WSalt}], \tag{3.19}$$

$$\sigma_{MUF_{Pyro}} = \sqrt{(\sigma_{F_{pyro}})^2 + (\sigma_{P_{Dross}})^2 + (\sigma_{P_{Udeposit}})^2 + (\sigma_{P_{LCC}})^2 + (\sigma_{P_{WSalt}})^2}\ . \tag{3.20}$$

In this study, we are interested in the Pu MUF, therefore, each term can be more specifically defined as the Pu mass measurement at each KMP. That Pu mass is measured by the Pu-to-^{244}Cm-ratio method, therefore, Eq. (3.18) can be rewritten by replacing the Pu mass term into the ratio times the ^{244}Cm mass as following,

$$\begin{aligned}\mathrm{PuMUF_{Pyro}} &= \left(\mathrm{PuF_{Pyro}}\right)-\left(\mathrm{PuP_{Dross}}\right)-\left(\mathrm{PuP_{Udeposit}}\right)-\left(\mathrm{PuP_{LCC}}\right)-\left(\mathrm{PuP_{WSalt}}\right)\\ &= \left(\mathrm{Ratio}\times{}^{244}\mathrm{CmF_{Pyro}}\right)-\left(\mathrm{Ratio}\times{}^{244}\mathrm{CmP_{Dross}}\right)-\left(\mathrm{Ratio}\times{}^{244}\mathrm{CmP_{Udeposit}}\right)\\ &\quad -\left(\mathrm{Ratio}\times{}^{244}\mathrm{CmP_{LCC}}\right)-\left(\mathrm{Ratio}\times{}^{244}\mathrm{CmP_{WSalt}}\right),\end{aligned} \tag{3.21}$$

where $\mathrm{PuMUF_{Pyro}}$ is the Pu MUF in the key-pyroprocess, $\mathrm{PuF_{Pyro}}$ is the Pu mass in the feed of the key-pyroprocess, $\mathrm{PuP_{Dross}}$ is the Pu mass in the dorss of the electrolytic-reduction process, $\mathrm{PuP_{Udoposit}}$ is the Pu mass in the U-deposit at the cathod in the electro reduction process, $\mathrm{PuP_{LCC}}$ is the Pu mass in the LCC of the electro-winning process, $\mathrm{PuP_{WSalt}}$ is the Pu mass in the salt from the electro-winning process, Ratio is the Pu-to-^{244}Cm-ratio, and the ^{244}Cm mass at each step is represented by replacing the text 'Pu' into '^{244}Cm'. Straighforwadly, the expection and standart deviation of Pu MUF in the key-pyroprocessing can be also reformulated as,

$$\begin{aligned}\mathrm{E}\left[\mathrm{PuMUF_{Pyro}}\right] &= \mathrm{E}\left[\mathrm{Ratio}\times{}^{244}\mathrm{CmF_{Pyro}}\right]-\mathrm{E}\left[\mathrm{Ratio}\times{}^{244}\mathrm{CmP_{Dross}}\right]-\mathrm{E}\left[\mathrm{Ratio}\times{}^{244}\mathrm{CmP_{Udeposit}}\right]\\ &\quad -\mathrm{E}\left[\mathrm{Ratio}\times{}^{244}\mathrm{CmP_{LCC}}\right]-\mathrm{E}\left[\mathrm{Ratio}\times{}^{244}\mathrm{CmP_{WSalt}}\right],\end{aligned} \tag{3.22}$$

$$\begin{aligned}\sigma_{\mathrm{PuMUF_{Pyro}}} &= \sqrt{\left(\sigma_{\mathrm{Ratio}}\sqrt{{}^{244}\mathrm{CmF_{Pyro}}}\right)^2+\left(\sigma_{\mathrm{Ratio}}\sqrt{{}^{244}\mathrm{CmP_{Dross}}}\right)^2+\left(\sigma_{\mathrm{Ratio}}\sqrt{{}^{244}\mathrm{CmP_{Udeopsit}}}\right)^2}\\ &\quad \sqrt{+\left(\sigma_{\mathrm{Ratio}}\sqrt{{}^{244}\mathrm{CmP_{LCC}}}\right)^2+\left(\sigma_{\mathrm{Ratio}}\sqrt{{}^{244}\mathrm{CmP_{WSalt}}}\right)^2}\\ &= \sigma_{\mathrm{Ratio}}\sqrt{{}^{244}\mathrm{CmF_{Pyro}}+{}^{244}\mathrm{CmP_{Dross}}+{}^{244}\mathrm{CmP_{Udeopsit}}+{}^{244}\mathrm{CmP_{LCC}}+{}^{244}\mathrm{CmP_{WSalt}}}.\end{aligned} \tag{3.23}$$

In order to develop the mass flow chart for the key-pyproprocess, the yield and effcieny of each process are referred by the previous study [13]. In addition to that, It is assumed that there is no loss during the head-end process. The assumed efficiencies and yields of each process are folloing;

- Electro-reduction:
    - TRU in the metal product is 99.5%,
    - TRU in the dross is 0.5%,
- Electro-refining:
    - TRU in salts is 99%,
    - TRU in the U-deposit is 1%,
- Electro-winning:
    - TRU in the LCC is 99%,
    - TRU in the salt is 1%.

Finally, the mass flow diagram for Pu and ^{244}Cm for the Type-0, -1, and -2 fuel assemblies after 1, 2, and 3cycles depletion is developed in Figure 51. The KMP and MBA are marked by the black solid circle filled with the red color and the red dot line in the figure.

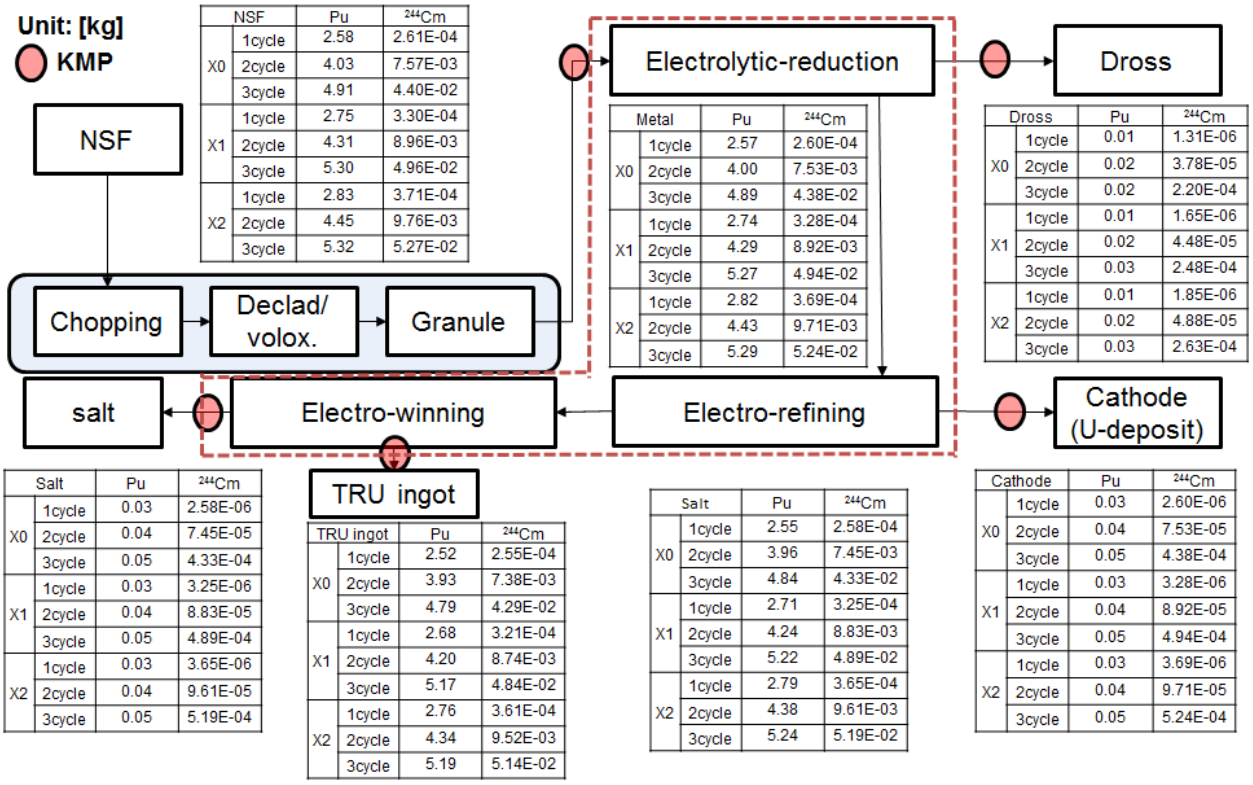

NSF		Pu	^{244}Cm
X0	1cycle	2.58	2.61E-04
	2cycle	4.03	7.57E-03
	3cycle	4.91	4.40E-02
X1	1cycle	2.75	3.30E-04
	2cycle	4.31	8.96E-03
	3cycle	5.30	4.96E-02
X2	1cycle	2.83	3.71E-04
	2cycle	4.45	9.76E-03
	3cycle	5.32	5.27E-02

Metal		Pu	^{244}Cm
X0	1cycle	2.57	2.60E-04
	2cycle	4.00	7.53E-03
	3cycle	4.89	4.38E-02
X1	1cycle	2.74	3.28E-04
	2cycle	4.29	8.92E-03
	3cycle	5.27	4.94E-02
X2	1cycle	2.82	3.69E-04
	2cycle	4.43	9.71E-03
	3cycle	5.29	5.24E-02

Dross		Pu	^{244}Cm
X0	1cycle	0.01	1.31E-06
	2cycle	0.02	3.78E-05
	3cycle	0.02	2.20E-04
X1	1cycle	0.01	1.65E-06
	2cycle	0.02	4.48E-05
	3cycle	0.03	2.48E-04
X2	1cycle	0.01	1.85E-06
	2cycle	0.02	4.88E-05
	3cycle	0.03	2.63E-04

Salt		Pu	^{244}Cm
X0	1cycle	0.03	2.58E-06
	2cycle	0.04	7.45E-05
	3cycle	0.05	4.33E-04
X1	1cycle	0.03	3.25E-06
	2cycle	0.04	8.83E-05
	3cycle	0.05	4.89E-04
X2	1cycle	0.03	3.65E-06
	2cycle	0.04	9.61E-05
	3cycle	0.05	5.19E-04

TRU ingot		Pu	^{244}Cm
X0	1cycle	2.52	2.55E-04
	2cycle	3.93	7.38E-03
	3cycle	4.79	4.29E-02
X1	1cycle	2.68	3.21E-04
	2cycle	4.20	8.74E-03
	3cycle	5.17	4.84E-02
X2	1cycle	2.76	3.61E-04
	2cycle	4.34	9.52E-03
	3cycle	5.19	5.14E-02

Salt		Pu	^{244}Cm
X0	1cycle	2.55	2.58E-04
	2cycle	3.96	7.45E-03
	3cycle	4.84	4.33E-02
X1	1cycle	2.71	3.25E-04
	2cycle	4.24	8.83E-03
	3cycle	5.22	4.89E-02
X2	1cycle	2.79	3.65E-04
	2cycle	4.38	9.61E-03
	3cycle	5.24	5.19E-02

Cathode		Pu	^{244}Cm
X0	1cycle	0.03	2.60E-06
	2cycle	0.04	7.53E-05
	3cycle	0.05	4.38E-04
X1	1cycle	0.03	3.28E-06
	2cycle	0.04	8.92E-05
	3cycle	0.05	4.94E-04
X2	1cycle	0.03	3.69E-06
	2cycle	0.04	9.71E-05
	3cycle	0.05	5.24E-04

Figure 51 The mass flow chart [g/cm^3] for Pu and ^{244}Cm in the key-pyroprocess (X0: Type-0 fuel assembly, X1: Type-1 fuel assembly, and X2: Type-2 fuel assembly).

Based on Eqs. 3.22 and 3.23, the hypothesis testing introduced in Section 2.5 is conducted. The assumptions necessary for testing are i) the null hypothesis is that the expectation of Pu MUF is zero, ii) the alternative hypothesis is that the expectation of Pu MUF is 8kg, iii) the significant threshold value (S) is 4kg, and iv) the only uncertainty caused by the non-uniformity of nuclide composition is considered. The probability of Type-I error for various spent fuel assemblies are shown in Figure 52. The red color area means 5% or more than 5% Type-I error. The rich blue is the probability of Type-I error is close to 0%. First, the area of red color regions increases as increasing the burnup cycles. Since the significant non-uniformity is observed in the low burnup spent fuel, the uncertainty for computing ratios is great for the low burnup case. However, the probability of Type-I error is also influenced the absolute mass of Pu and ^{244}Cm mass as shown in Eq. 3.23. By increasing the burnup cycles, the mass of ^{244}Cm and Pu are increased. Therefore, the probability of Type-I error is escalated as increasing the burnup cycle, even though the uncertainty of ratio is decreasing. Second, the number of GBFs has the proportional relationship with the probability of Type-I error, because it increases not only the non-uniformity of Pu and ^{244}Cm but also the production of Pu and ^{244}Cm.

Those results are based on processing of the single assembly. The reporting of MUF for MBA would be conducted after each campaign which would be defined multiple processing of spent fuel assemblies. Therefore, the error propagation through cycles and processing of assemblies should be considered. Figure 53 shows a number of spent assemblies for the Type-I error to be 5%. The log10 scale for colormap is applied, for instance, the rich red color (numbering with 0 in the colormap) and the green color (numbering with 3 in the colormap) means one assembly and one thousand assemblies. As mentioned above, the several assemblies would be treated during one campaign. Therefore, the red and orange regions could be considered as a crucial situation to develop material accountancy for pyroprocess. The trend of results shows that a number of assemblies to be the 5% Type-I error decreases by increasing the depletion period and a number of GBFs in the assembly.

FA Type	1 cycle	2 cycles	3 cycles
0	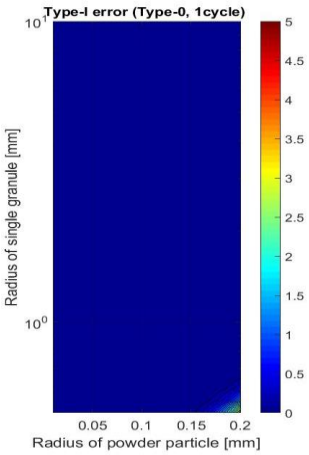	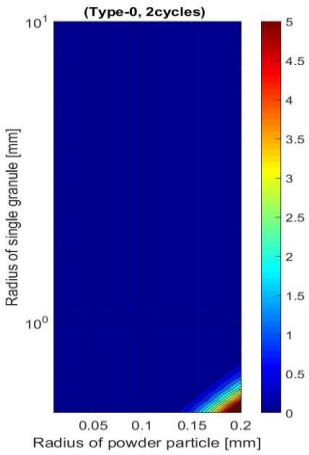	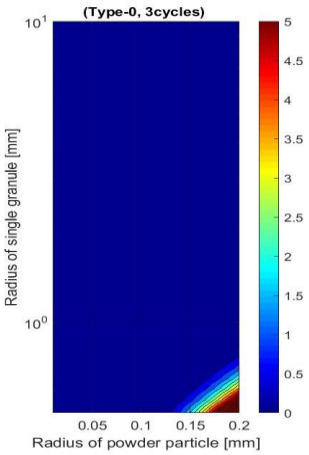
1	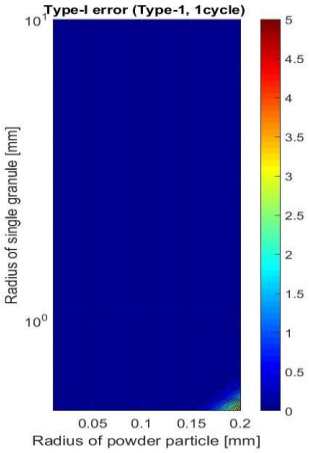	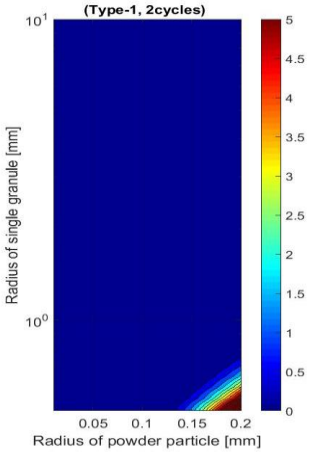	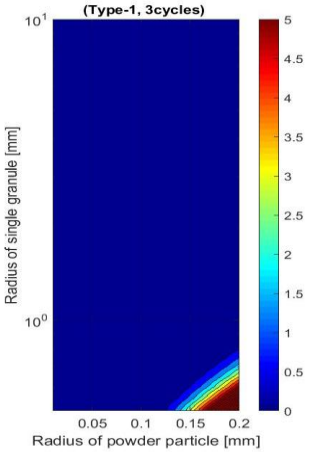
2	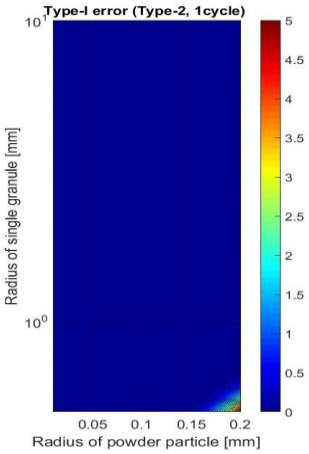	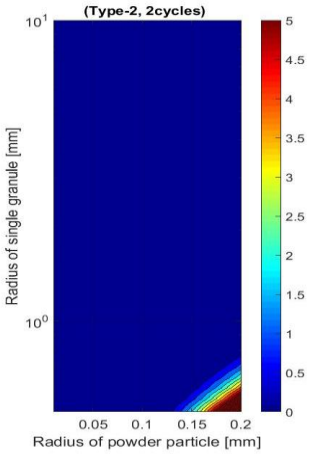	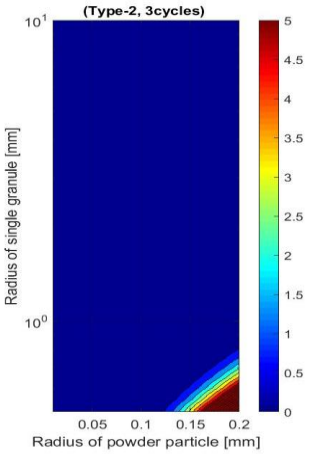

Figure 52 Probability of Type-I error for Pu MUF in spent fuel assemblies.

FA Type	1 cycle	2 cycles	3 cycles
0	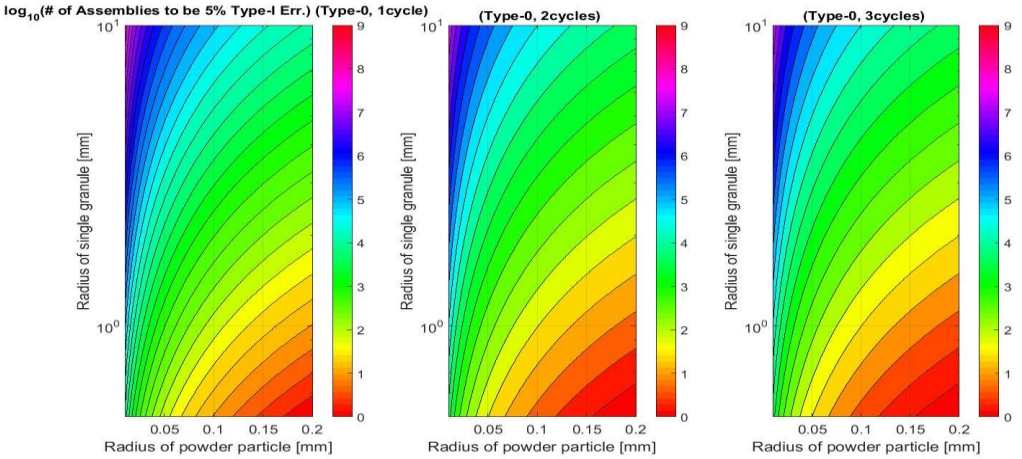		
1	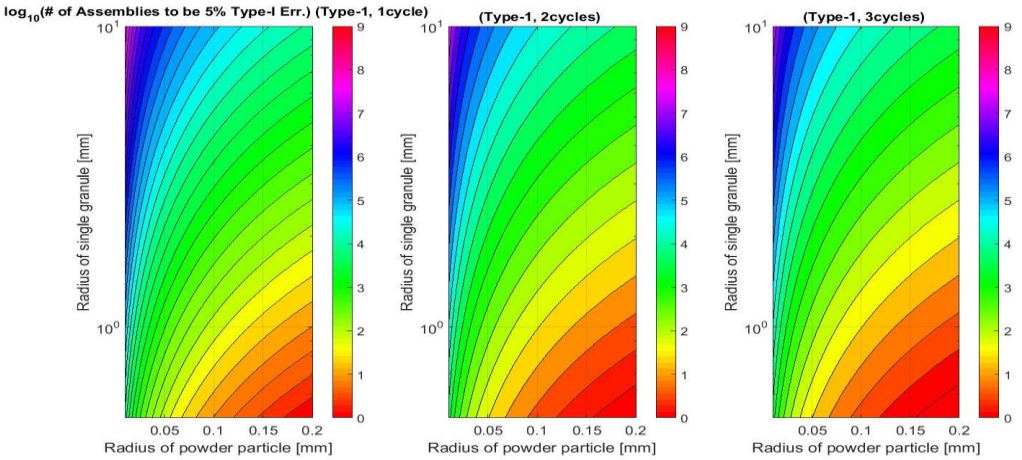		
2	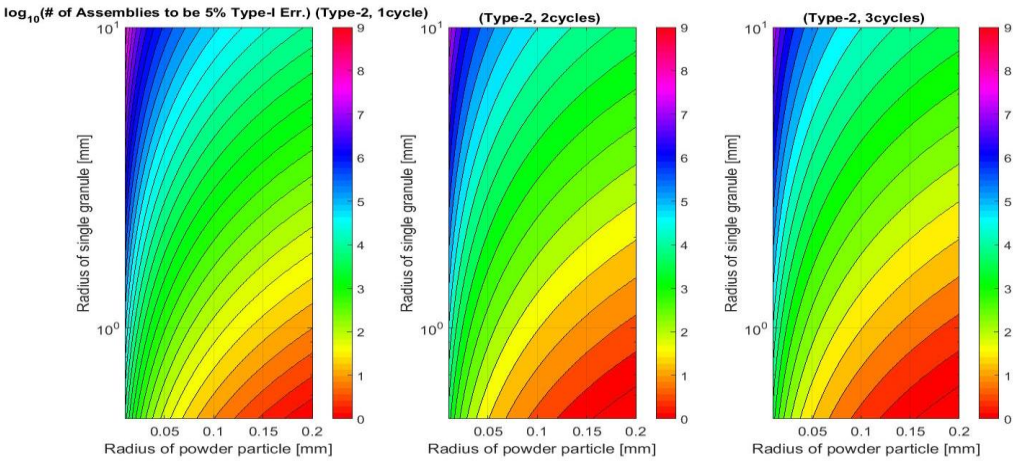		

Figure 53 Number of assemblies necessary for the Type-I error to be 5% (log_{10} scale for the colormap).

3.3.3 Hypothesis testing for the Loss of Pu (LOPu) scenario

The MUF is the used to analyze the material balance within the defined MBA. For this scope it would not be appropriate to study the probability of detection at the single KMP. Let us define a new random variable named Loss of Pu (LOPu) evaluated by the difference of the original Pu mass (Pu_{Org}) and the Pu mass after missing (Pu_{Loss}) as shown below,

$$\mathrm{LOPu} = \mathrm{Pu}_{\mathrm{Org}} - \mathrm{Pu}_{\mathrm{Loss}}. \tag{3.24}$$

Eq. 3.24 can be rewritten as,

$$\mathrm{LOPu} = \left(\mathrm{Ratio}_{\mathrm{Org}} \times {}^{244}\mathrm{Cm}_{\mathrm{Org}}\right) - \left(\mathrm{Ratio}_{\mathrm{Loss}} \times {}^{244}\mathrm{Cm}_{\mathrm{Loss}}\right), \tag{3.25}$$

where $\mathrm{Ratio}_{\mathrm{Org}}$ is the original Pu-to-^{244}Cm-ratio, $^{244}\mathrm{Cm}_{\mathrm{Org}}$ is the original ^{244}Cm mass, and $\mathrm{Ratio}_{\mathrm{Loss}}$ and $^{244}\mathrm{Cm}_{\mathrm{Loss}}$ is the Pu-to-^{244}Cm-ratio and ^{244}Cm mass after missing materials. Those two random variables, Pu_{Org} and Pu_{Org}, are measured values using the Pu-to-^{244}Cm-ratio method. It can be reasonably assumed they are following the normal distribution, therefore, the LOPu also follows the normal distribution expressed as following,

$$\begin{aligned} \mathrm{Pu}_{\mathrm{Org}} &\sim N\left(\mu_{\mathrm{Pu}_{\mathrm{Org}}}, \sigma^2_{\mathrm{Pu}_{\mathrm{Org}}}\right), \\ \mathrm{Pu}_{\mathrm{Loss}} &\sim N\left(\mu_{\mathrm{Pu}_{\mathrm{Loss}}}, \sigma^2_{\mathrm{Pu}_{\mathrm{Loss}}}\right), \\ \Rightarrow \mathrm{LOPu} &\sim N\left(\mu_{\mathrm{LOPu}}, \sigma^2_{\mathrm{LOPu}}\right). \end{aligned} \tag{3.26}$$

The expectation of LOPu can be evaluated as,

$$\mathrm{E}[\mathrm{LOPu}] = \mathrm{E}\left[\mathrm{Ratio}_{\mathrm{Org}} \times {}^{244}\mathrm{Cm}_{\mathrm{Org}}\right] - \mathrm{E}\left[\mathrm{Ratio}_{\mathrm{Loss}} \times {}^{244}\mathrm{Cm}_{\mathrm{Loss}}\right]. \tag{3.27}$$

It is ignored that the uncertainty for measuring ^{244}Cm by a neutron counting rate, therefore, Eq. 3.27 can be written as,

$$\mathrm{E}[\mathrm{LOPu}] = \mathrm{E}\left[\mathrm{Ratio}_{\mathrm{Org}}\right] \times {}^{244}\mathrm{Cm}_{\mathrm{Org}} - \mathrm{E}\left[\mathrm{Ratio}_{\mathrm{Loss}}\right] \times {}^{244}\mathrm{Cm}_{\mathrm{Loss}}. \tag{3.28}$$

After processing N assemblies, the expectation (μ) of LOPu is evaluated by

$$\mu^{\mathrm{N}}_{\mathrm{LOPu}} = \mu_{\mathrm{LOPu},1} + \mu_{\mathrm{LOPu},2} + \mu_{\mathrm{LOPu},3} + \cdots + \mu_{\mathrm{LOPu,N}} = \mu_{\mathrm{LOPu}} \times N. \tag{3.29}$$

Using the property of variance for the linear combination of two independent random variables, the standard deviation of LOPu at the single KMP is evaluated by below,

$$\sigma_{\mathrm{LOPu}} = \sqrt{\left(\sigma_{\mathrm{Ratio}_{\mathrm{Org}}} \times {}^{244}\mathrm{Cm}_{\mathrm{Org}}\right)^2 + \left(\sigma_{\mathrm{Ratio}_{\mathrm{Loss}}} \times {}^{244}\mathrm{Cm}_{\mathrm{Loss}}\right)^2}. \tag{3.30}$$

The uncertainty is propagated through N assemblies as below,

$$\sigma_{\mathrm{LOPu}}^{\mathrm{N}} = \sqrt{\left(\sigma_{\mathrm{LOPu},1}\right)^2 + \left(\sigma_{\mathrm{LOPu},2}\right)^2 + \left(\sigma_{\mathrm{LOPu},3}\right)^2 + \cdots + \left(\sigma_{\mathrm{LOPu,N}}\right)^2} = \sigma_{\mathrm{LOPu}}\sqrt{\mathrm{N}}\,. \tag{3.31}$$

The probability of Type-II error (β) for LOPu can be formulated by modifying Eq. (2.15) as shown below,

$$\beta = \mathrm{Prob}\left\{\frac{\mathrm{LOPu} - \mu_{\mathrm{LOPu}}^{\mathrm{N}}}{\sigma_{\mathrm{LOPu}}^{\mathrm{N}}} \le \frac{\mathrm{S} - \mu_{\mathrm{LOPu}}^{\mathrm{N}}}{\sigma_{\mathrm{LOPu}}^{\mathrm{N}}} \middle| \mathrm{H_a}\right\} = \Phi\left\{\frac{\mathrm{S} - \mu_{\mathrm{LOPu}}^{\mathrm{N}}}{\sigma_{\mathrm{LOPu}}^{\mathrm{N}}}\right\}. \tag{3.32}$$

Therefore, the probability of detection for LOPu at the single KMP is

$$1-\beta = \Phi\left\{\frac{\mu_{\mathrm{LOPu}}^{\mathrm{N}} - \mathrm{S}}{\sigma_{\mathrm{LOPu}}^{\mathrm{N}}}\right\}. \tag{3.33}$$

In order to develop the missing scenario, it is assumed that they miss the material right after chopping process. Hence, the object of missing material is chopped pieces. The different cases are considered as below;

- Case 1: 1 Piece missing/rod,
- Case 2: 3 Pieces missing/rod,
- Case 3: 5 Pieces missing/rod,
- Case 4: 10 Pieces missing/rod.

The length of pieces is 1 cm, therefore, the 381cm single fuel rod can produce 381 pieces. One assembly has 236 fuel rods. The total generated pieces by the chopping process for the single fuel rod is 89,916 pieces. A number of missing pieces for four cases are 236 (case 1), 703 (case 2), 1180 (case 3), and 2360 (case 4) pieces/assembly. The missing chopped pieces are intentionally selected pieces originally located at the middle of fuel rods before the chopping process, because the Pu mass for those pieces is generally greater than the Pu mass of other pieces. For example, for the 5 pieces missing per rod case (Case 3), the missing pieces are selected that originally located at the 190 cm, 189 cm, 188 cm, 187 cm, and 186 cm height from the bottom of the fuel rod. The case for 3 pieces missing per rod is the intentionally selected the missing pieces originally located at the 190 cm, 189 cm, and 188 cm height. After 4 missing pieces cases, the Pu mass for each spent fuel assembly is summarized in Table 20. The third column named 'No missing' is the original Pu mass with any missing. The fourth to seventh columns show the Pu mass after 1, 3, 5, and 10 pieces missing per rod. The difference between the original Pu mass and the Pu mass after missing in the single assembly is not statistically significant to detect, because the significant threshold value (S) is set as 4 kg. In the previous section, the alternative hypothesis is the Pu MUF is equal to 8 kg (1SQ). Therefore, the moment considered in this study is when the Pu mass missing becomes 8 kg. In other words, a number of assemblies for the LOPu to be 8 kg is interesting. The number of assemblies should be integer; therefore, the ceiling function is applied to count shown in

Table 21. The LOPu after processing those assemblies is slightly greater than 8 kg. Those data are utilized as the N values in Eqs. 3.29 and 3.31. Using the GH transformation, the expected ratio and

its standard deviation for 4 cases can be calculated as shown in Figure 54 (Type-0 fuel assembly after 1cycle depletion), Figure 55 (Type-0 fuel assembly after 2cycles depletion),Figure 56 (Type-0 fuel assembly after 3cycles depletion), Figure 57 (Type-1 fuel assembly after 1cycle depletion), Figure 58 (Type-1 fuel assembly after 2cycles depletion), Figure 59 (Type-1 fuel assembly after 3cycles depletion), Figure 60 (Type-2 fuel assembly after 1cycle depletion), Figure 61 (Type-2 fuel assembly after 2cycles depletion), andFigure 62 (Type-2 fuel assembly after 3cycles depletion). The difference between those ranges from 0 to 10%. The difference of ratios among four missing cases for each spent fuel assembly shows similarly, because the ratios among four cases are still too close to visually show that difference.

Table 20 Pu mass for spent fuel assemblies after missing pieces after the chopping process.

FA Type	Cycle	Pu mass for cases [kg]				
		No missing	1P/rod	3 P/rod	5 P/rod	10 P/rod
Type-0	1	2.58	2.58	2.56	2.55	2.51
	2	4.03	4.01	3.99	3.97	3.92
	3	4.91	4.90	4.87	4.84	4.78
Type-1	1	2.75	2.74	2.73	2.71	2.67
	2	4.31	4.30	4.27	4.25	4.19
	3	5.30	5.29	5.26	5.23	5.16
Type-2	1	2.83	2.83	2.81	2.79	2.75
	2	4.45	4.44	4.41	4.39	4.33
	3	5.32	5.30	5.28	5.25	5.17

Table 21 Number of assemblies for the LOPU to be 8kg.

FA Type	Cycle	Number of assemblies for LOPu to be 8kg				
		No missing	1P/rod	3 P/rod	5 P/rod	10 P/rod
Type-0	1	-	1098	366	220	110
	2	-	737	245	146	73
	3	-	615	204	122	61
Type-1	1	-	1030	343	206	103
	2	-	689	229	137	68
	3	-	569	188	113	56
Type-2	1	-	999	333	200	100
	2	-	666	221	132	66
	3	-	568	188	112	56

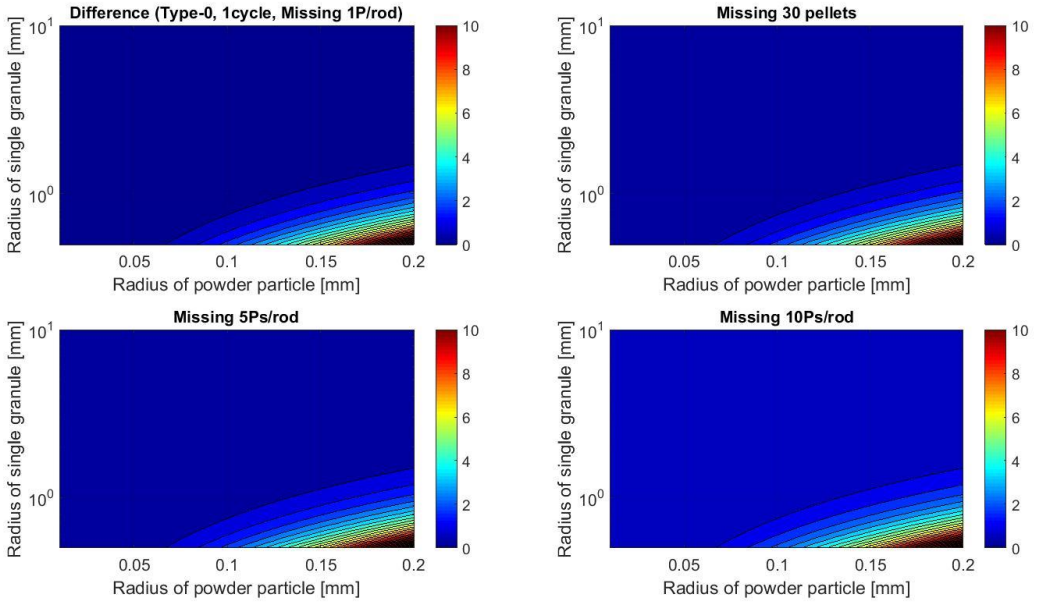

Figure 54 Difference of ratios between the case nothing missing and the 4 missing cases for the Type-0 assembly after 1 cycle depletion.

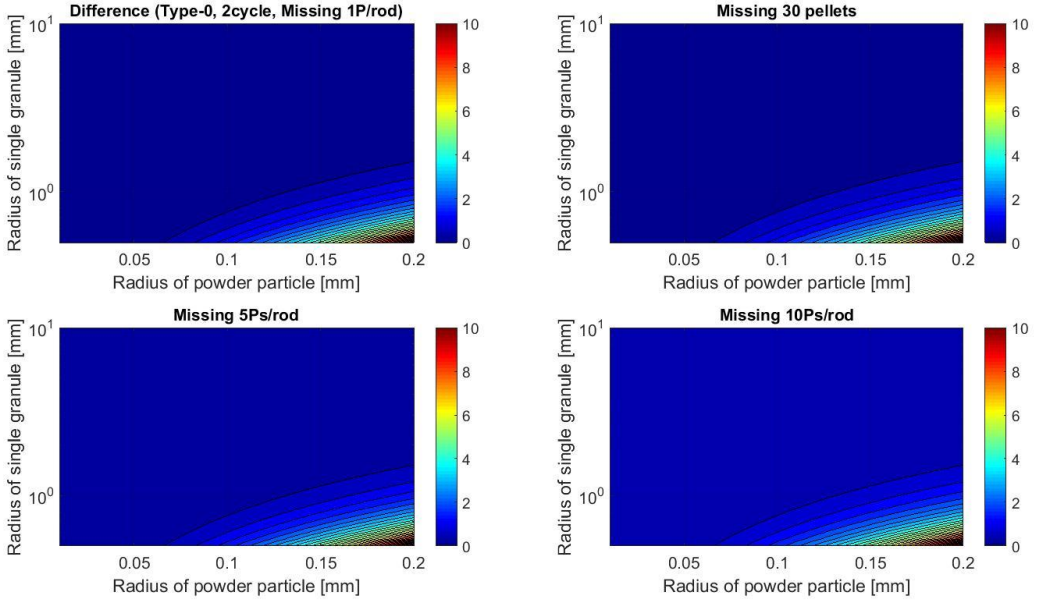

Figure 55 Difference of ratios between the nothing missing case and the 4 missing cases for the Type-0 assembly after 2 cycles depletion.

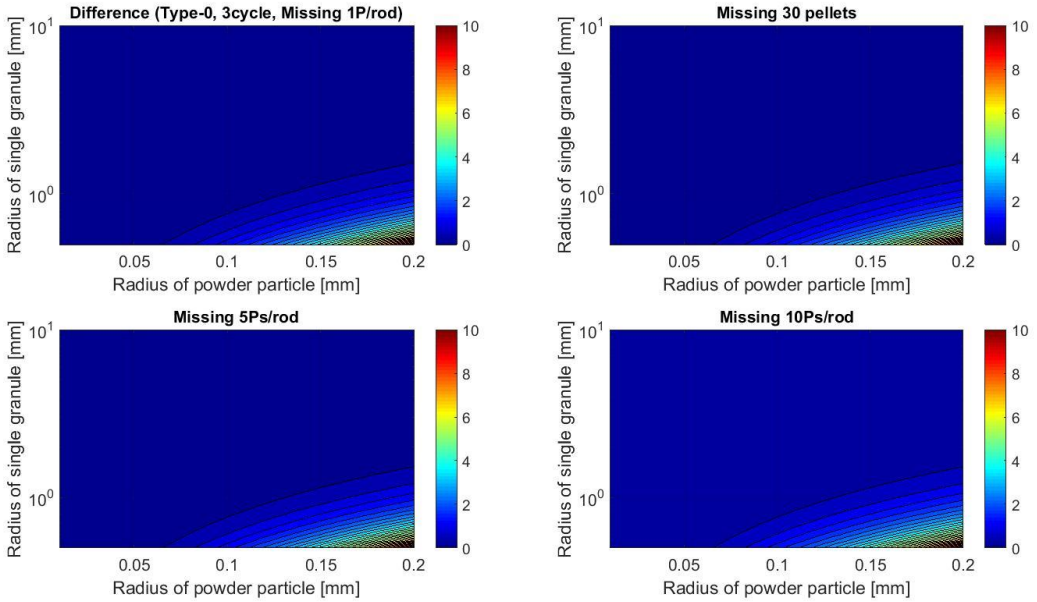

Figure 56 Difference of ratios between the nothing missing case and the 4 missing cases for the Type-0 assembly after 3 cycles depletion.

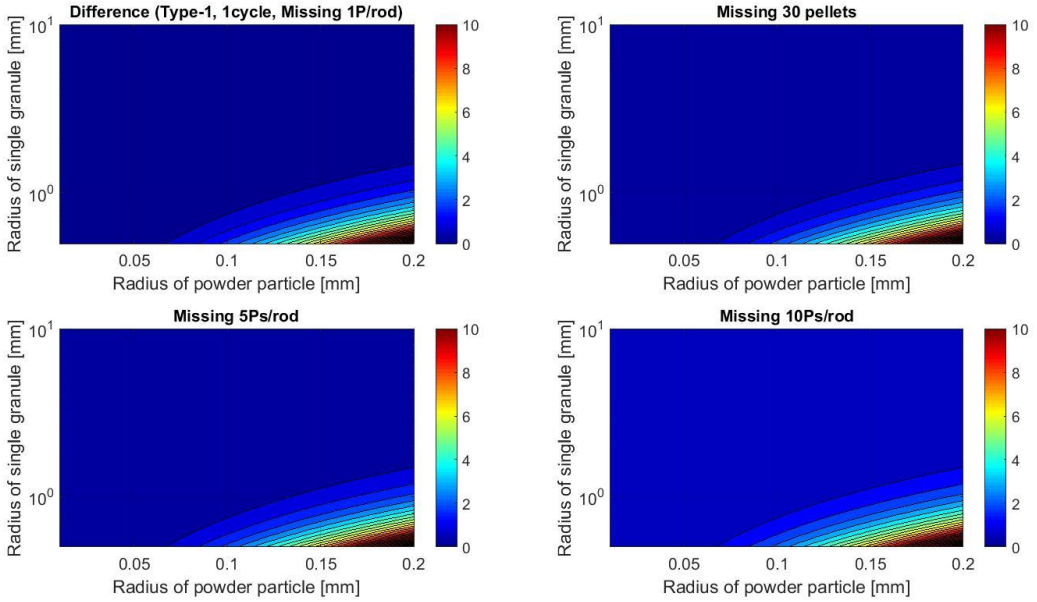

Figure 57 Difference of ratios between the nothing missing case and the 4 missing cases for the Type-1 assembly after 1 cycle depletion.

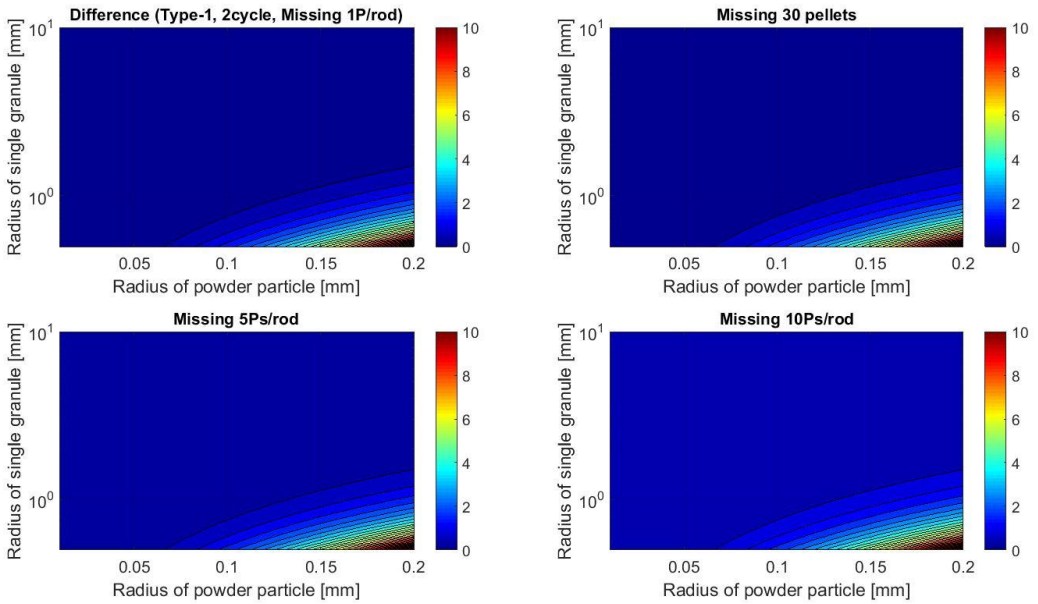

Figure 58 Difference of ratios between the nothing missing case and the 4 missing cases for the Type-1 assembly after 2 cycles depletion.

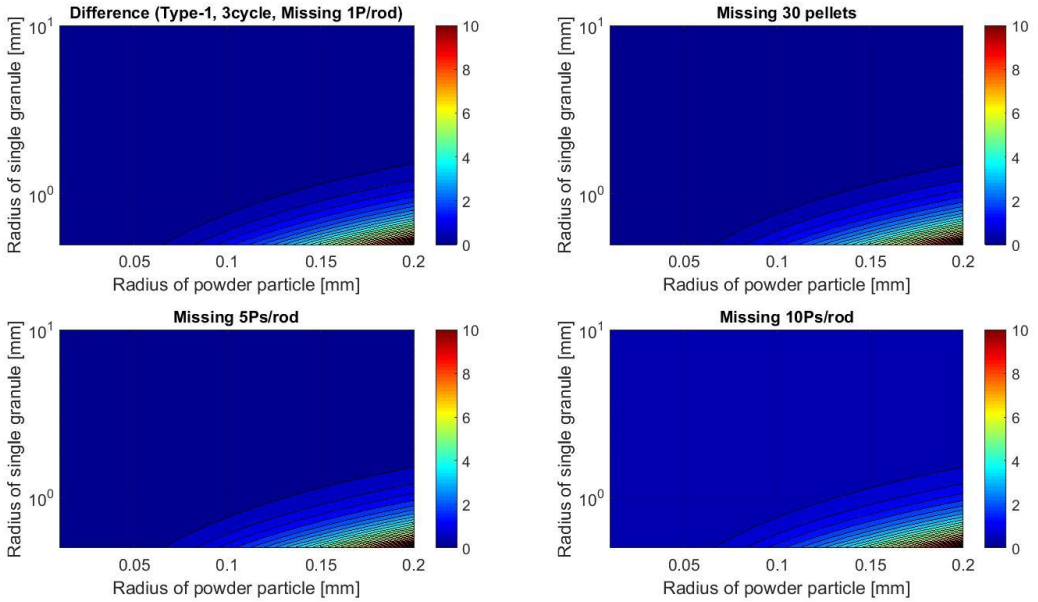

Figure 59 Difference of ratios between the nothing missing case and the 4 missing for the Type-1 assembly after 3 cycles depletion.

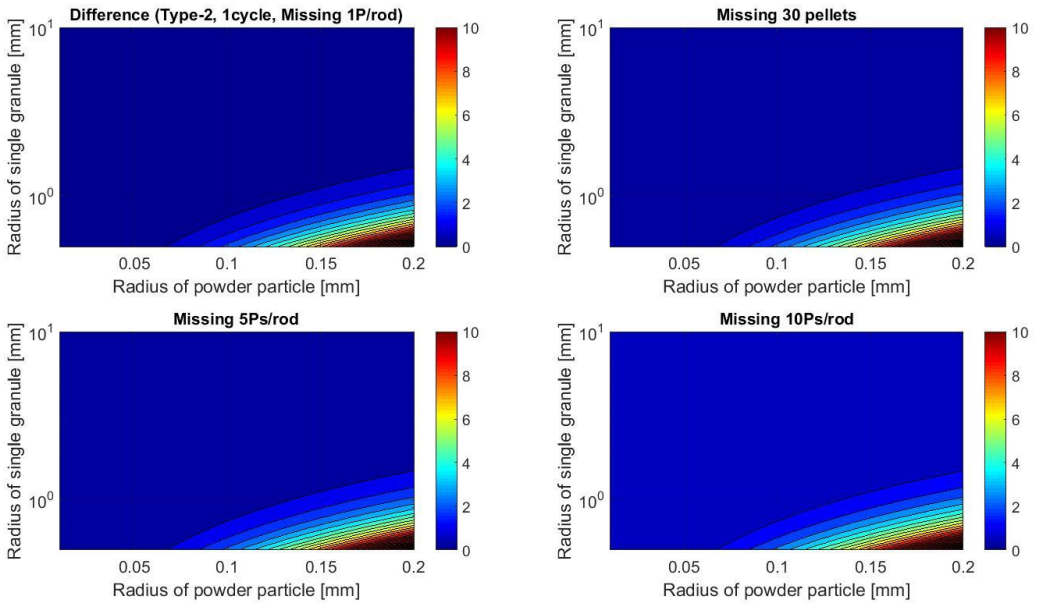

Figure 60 Difference of ratios between the nothing missing case and the 4 missing cases for the Type-2 fuel assembly after 1 cycle depletion.

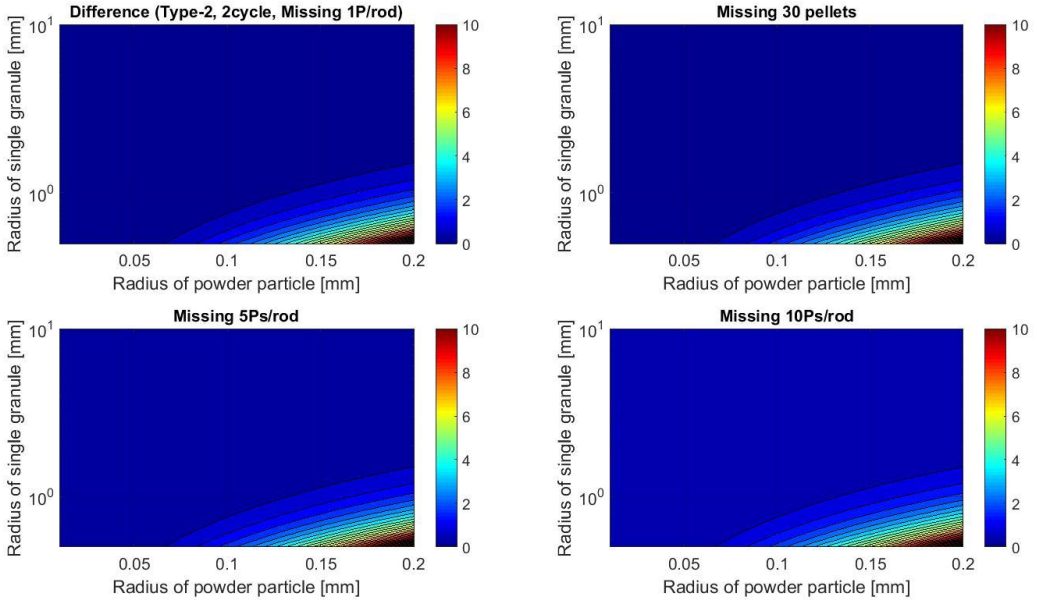

Figure 61 Difference of ratios between the nothing missing case and the 4 missing cases for the Type-2 fuel assembly after 2 cycles depletion.

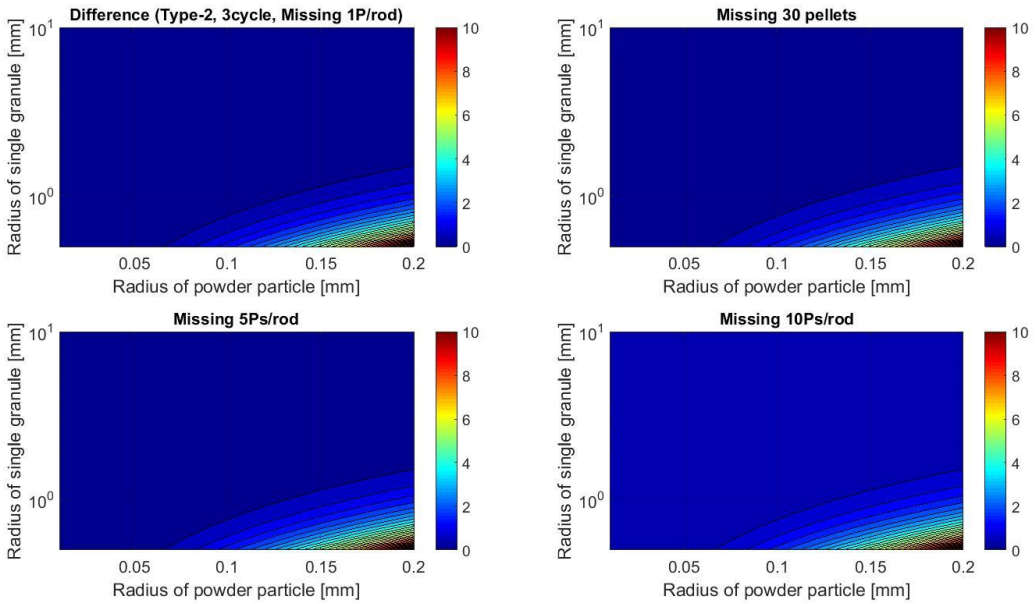

Figure 62 Difference of ratios between the nothing missing case and the 4 missing cases for the Type-2 fuel assembly after 3 cycles depletion.

The probability of detection for the LOPu explained above is to evaluate the probability at the single KMP. Since the key-pyroprocess has 5 KMPs shown in Figure 50, the probability of detection for the entire system can be computed by the event tree analysis developed in Figure 63. The total probability of detection for the LOPu in the system is the summation of all possible pathways as formulated below,

$$\text{Total Prob. of detection} = \text{Prob}\{\text{D-1}\} + \text{Prob}\{\text{D-2}\} + \text{Prob}\{\text{D-3}\} + \text{Prob}\{\text{D-4}\} + \text{Prob}\{\text{D-5}\}. \quad (3.34)$$

The results for the total probability of detection for the 4 LOPu cases using different spent fuel assemblies are plotted as a function the radius of a granule and a powder particle as shown in Figure 64 (Type-0 assembly after 1cycle depletion), Figure 65 (Type-0 assembly after 2cycles depletion), Figure 66 (Type-0 assembly after 3cycles depletion), Figure 67 (Type-1 assembly after 1cycle depletion), Figure 68 (Type-1 assembly after 2cycles depletion), Figure 69 (Type-1 depleted 3cycles spent fuel assembly), Figure 70 (Type-2 assembly after 1cycle depletion), Figure 71 (Type-2 assembly after 2cycles depletion), and Figure 72 (Type-2 assembly after 3cycles depletion). The current criteria for material accountancy is the probability of detection should be greater than 95% [4], which is corresponding to the orange color area in those figures. We can observe the high possibility of detection probability for the LOPu less than 95%. The area for detection probability less than 95% is getting smaller as increasing the number of missing pieces by comparing among the case 1 to 4 for each spent fuel assembly. The case of stealing clandestinely a large amount of material would be easier to be detected than that of stealing a small amount of material. The detecting probability for the LOPu decreases as increasing burnup, even though the non-uniformity of nuclide composition decreases. This could be caused by the

increasing absolute mass of ^{244}Cm with respect to the depletion length escalates proportionally the standard deviation of LOPu as shown in Eq. 3.30. This tendency is also shown by comparing the results among the Type-0, -1, and -2 assemblies. The Type-2 spent fuel assembly holding the greatest ^{244}Cm mass among 3 assembly types shows the smallest detecting probabilities for the LOPu. By this observation, the capacity of throughput in the system would significantly affect material accountancy.

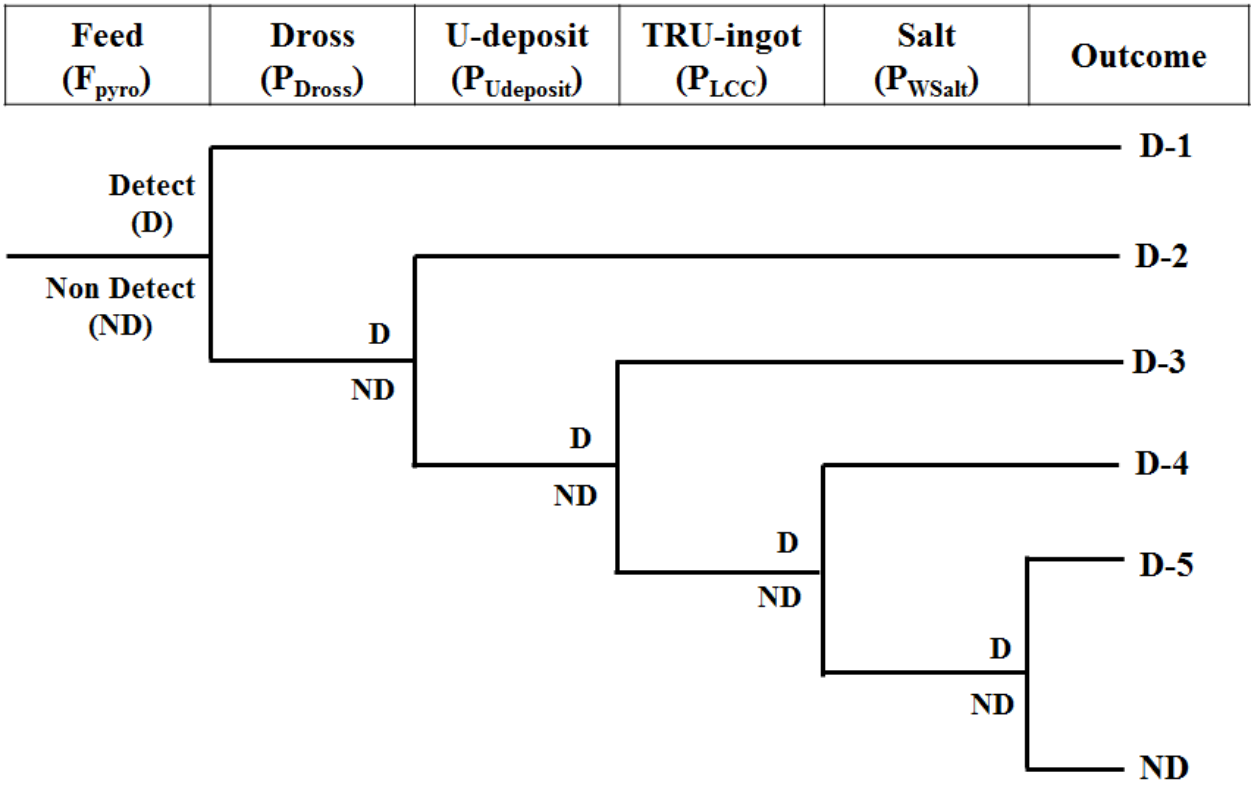

Figure 63 Event tree for the probability of detection for the LOPu scenario.

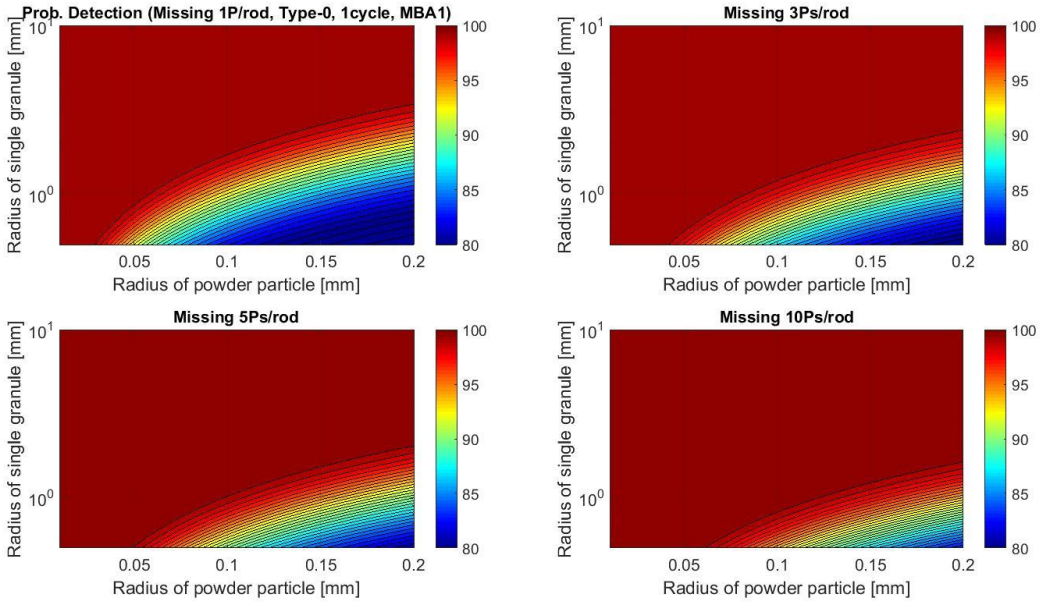

Figure 64 Probability of detection for the LOPu in the key-pyroprocess for the Type-0 assembly after 1cycle depletion.

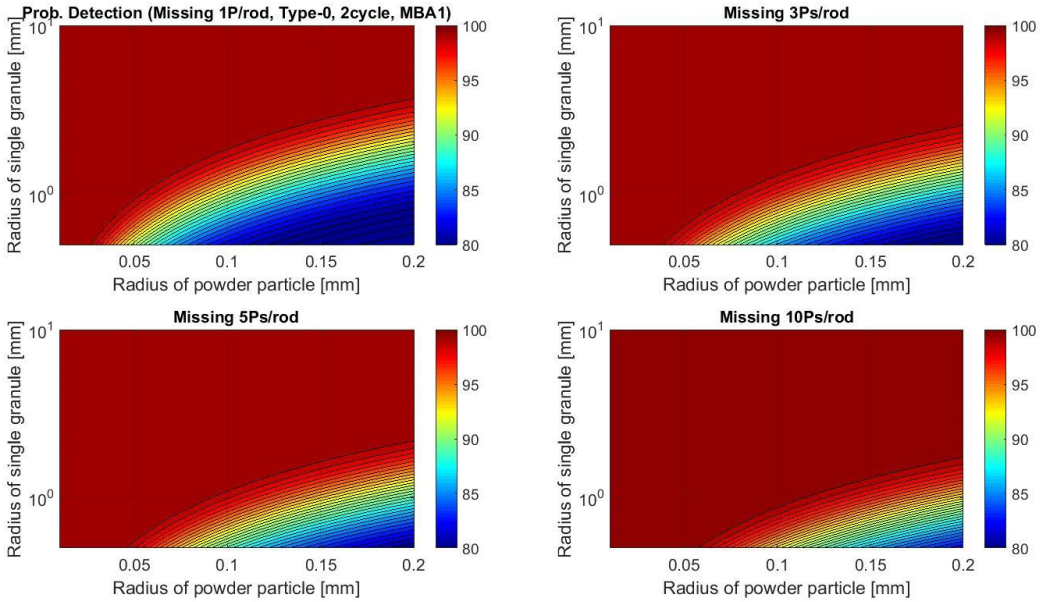

Figure 65 Probability of detection for the LOPu in the key-pyroprocess for the Type-0 assembly after 2cycles depletion.

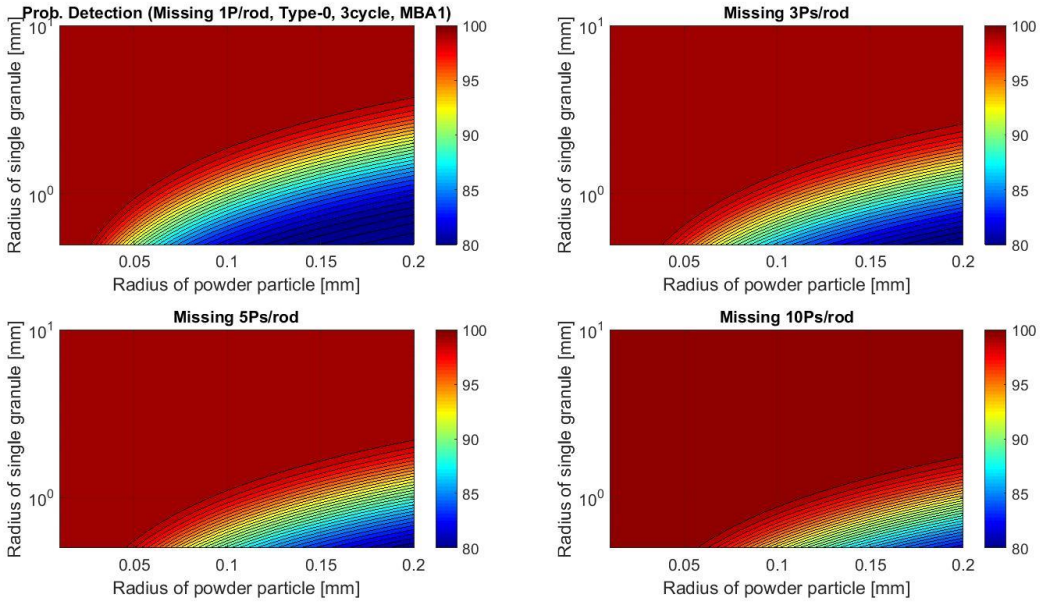

Figure 66 Probability of detection for the LOPu in the key-pyroprocess for the Type-0 assembly after 3cycles depletion.

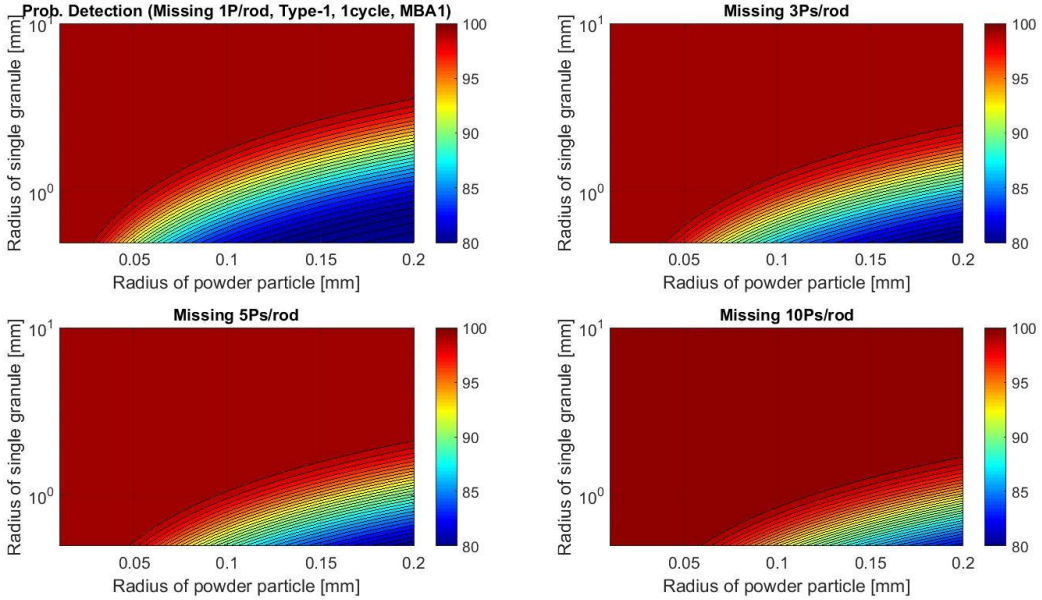

Figure 67 Probability of detection for the LOPu in the key-pyroprocess for the Type-1 assembly after 1cycle depletion.

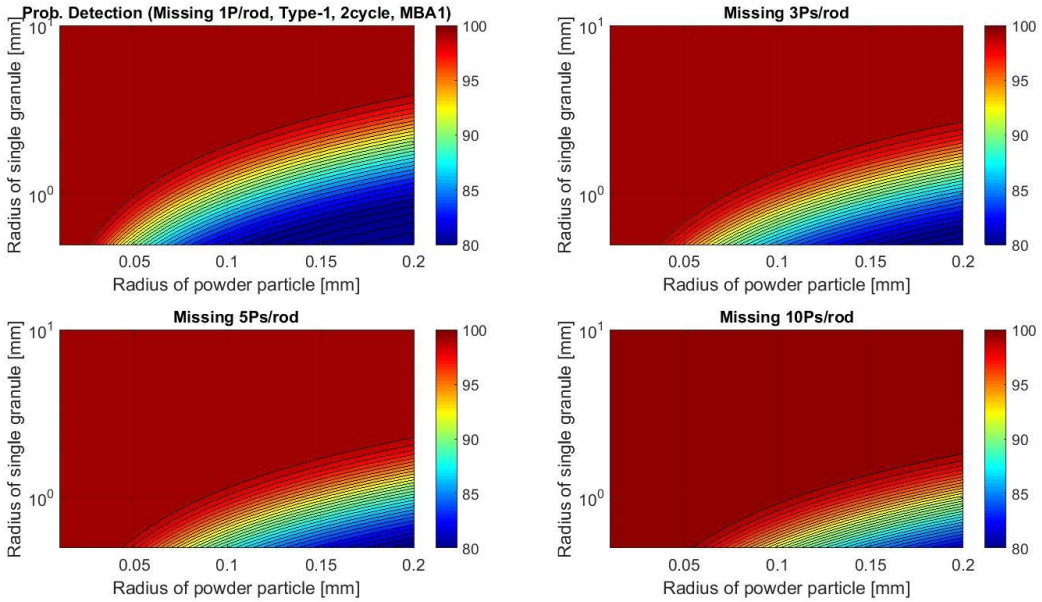

Figure 68 Probability of detection for the LOPu in the key-pyroprocess for the Type-1 assembly after 2cycles depletion.

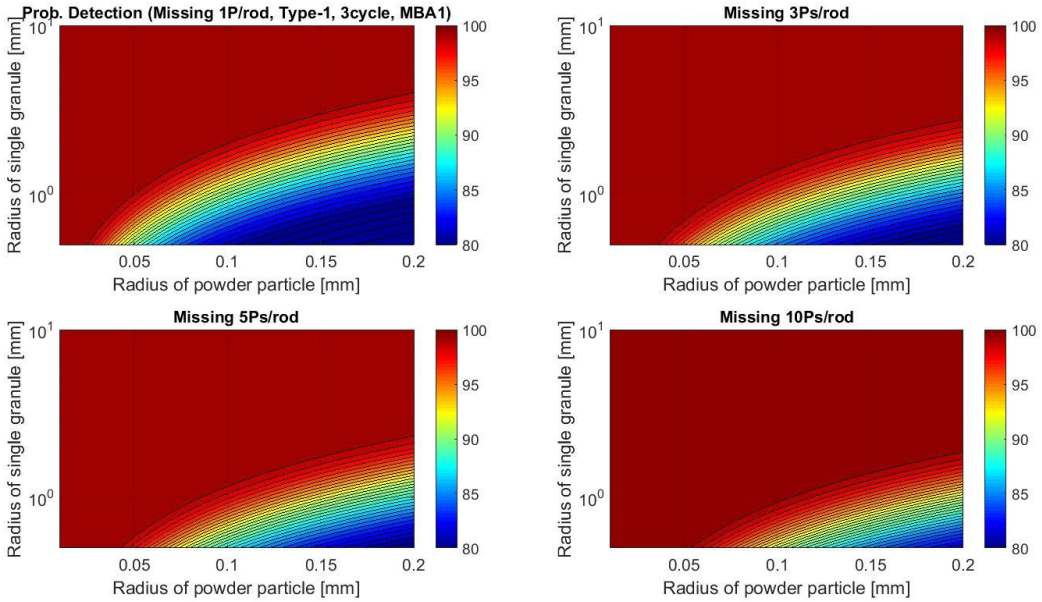

Figure 69 Probability of detection for the LOPu in the key-pyroprocess for the Type-1 assembly after 3cycles depletion.

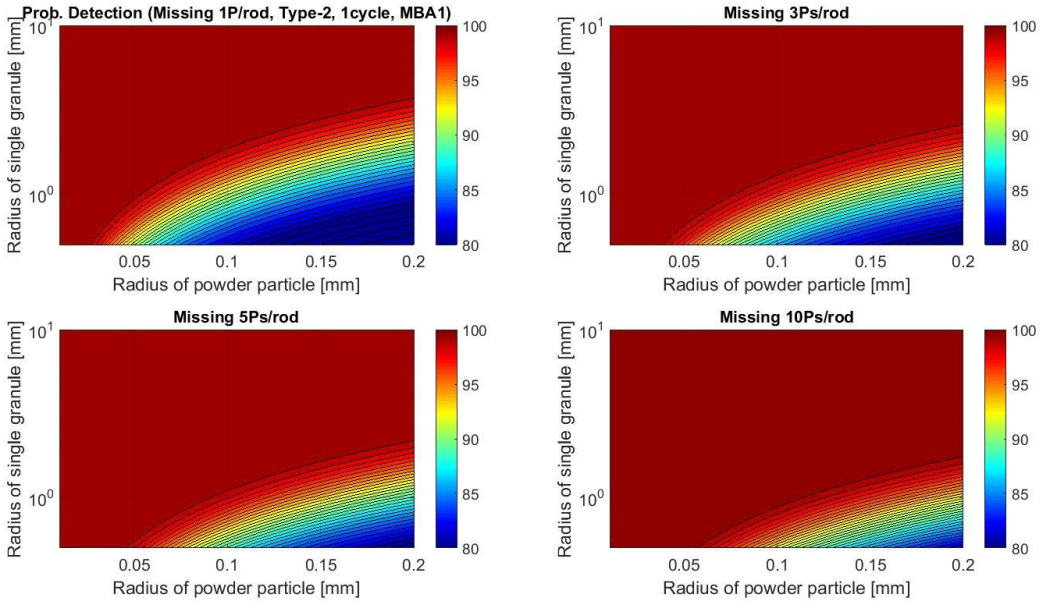

Figure 70 Probability of detection for the LOPu in the key-pyroprocess for the Type-2 assembly after 1cycle depletion.

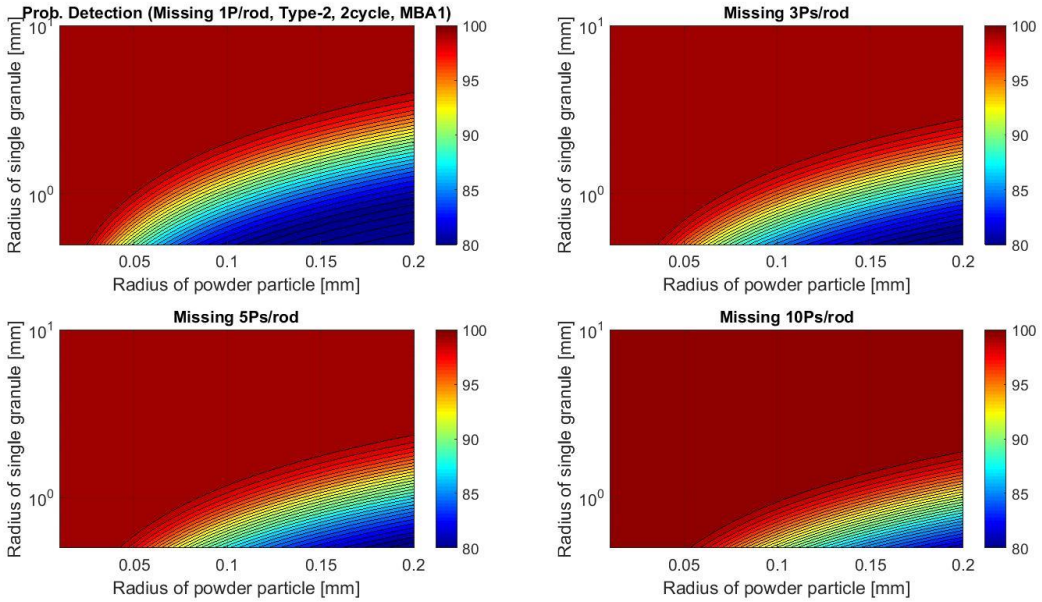

Figure 71 Probability of detection for the LOPu in the key-pyroprocess for the Type-2 assembly after 2cycles depletion.

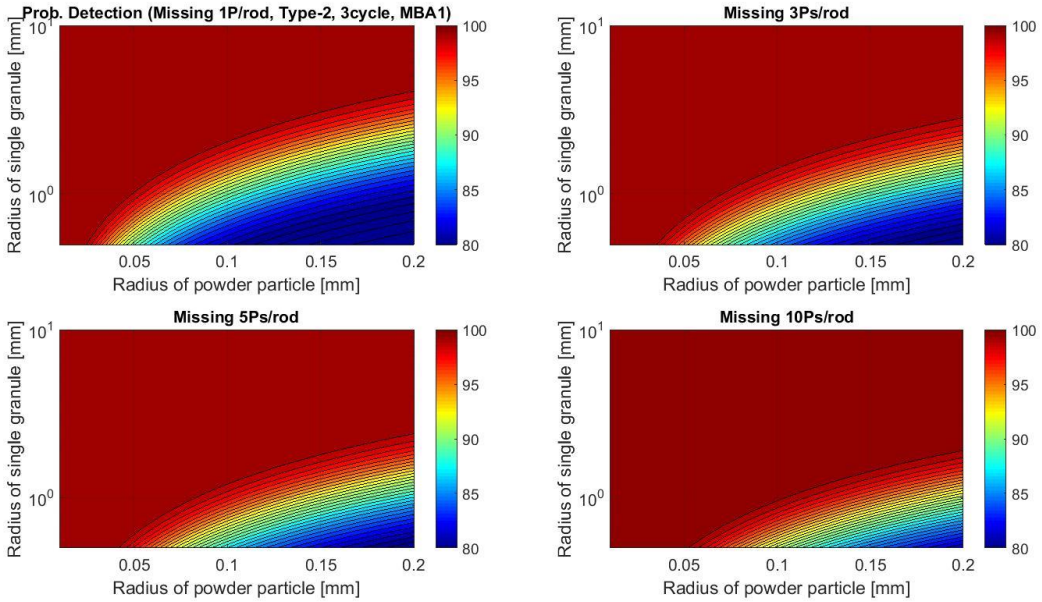

Figure 72 Probability of detection for the LOPu in the key-pyroprocess for the Type-2 assembly after 3cycles depletion.

In order to enhance the probability of detection for the LOPu, the two approaches, i) increasing KMPs by modifying the MBA, and ii) increasing sampling granules to decrease the uncertainty of ratio, have been tried in this section.

The current simplified MBA for pyroprocess having 5 KMPs is shown Figure 50 Schematic layout for MBA of key-pyroprocess. However, a new MBA model for the key-pyroprocess consists of 3 sub-MBAs with 9 KMPs as shown in Figure 73. The black boxes and red circles mean the MBA and the KMP, respectively. Based on this model, the event tree is modified as Figure 74. The probability of detection in the key-pyroprocess consisting of 3 sub-MBAs and 9 KMPs can be calculated by

$$\begin{aligned}\text{Total Prob. of detection} = {} & \text{Prob}\{D-1\} + \text{Prob}\{D-2\} + \text{Prob}\{D-3\} + \text{Prob}\{D-4\} + \text{Prob}\{D-5\} \\ & + \text{Prob}\{D-6\} + \text{Prob}\{D-7\} + \text{Prob}\{D-8\} + \text{Prob}\{D-9\}.\end{aligned} \quad (3.35)$$

The probabilities of detection for the LOPu based on the new MBA model using different spent fuel assemblies have been plotted in Figure 75 (Type-0 fuel assembly after 1cycle depletion), Figure 76 (Type-0 fuel assembly after 2cycles depletion), Figure 77 (Type-0 fuel assembly after 3cycles depletion), Figure 78 (Type-1 fuel assembly after 1cycle depletion), Figure 79 (Type-1 fuel assembly after 2cycles depletion), Figure 80 (Type-1 fuel assembly after 3cycles depletion), Figure 81 (Type-2 fuel assembly after 1cycle depletion), Figure 82 (Type-2 fuel assembly after 2cycles depletion), and Figure 83 (Type-2 fuel assembly after 3cycles depletion). The range of colormap for all figures are 99 to 100%. It shows that the probability of detection for all cases are greater than 99%. The significant increasing of results is observed by the modifying MBAs and

KMPs for the key-pyroprocess, even though the only single granule is taken as a sample to evaluate the ratio. Furthermore, this approach could be utilized as a methodology to design a MBA for nuclear facilities.

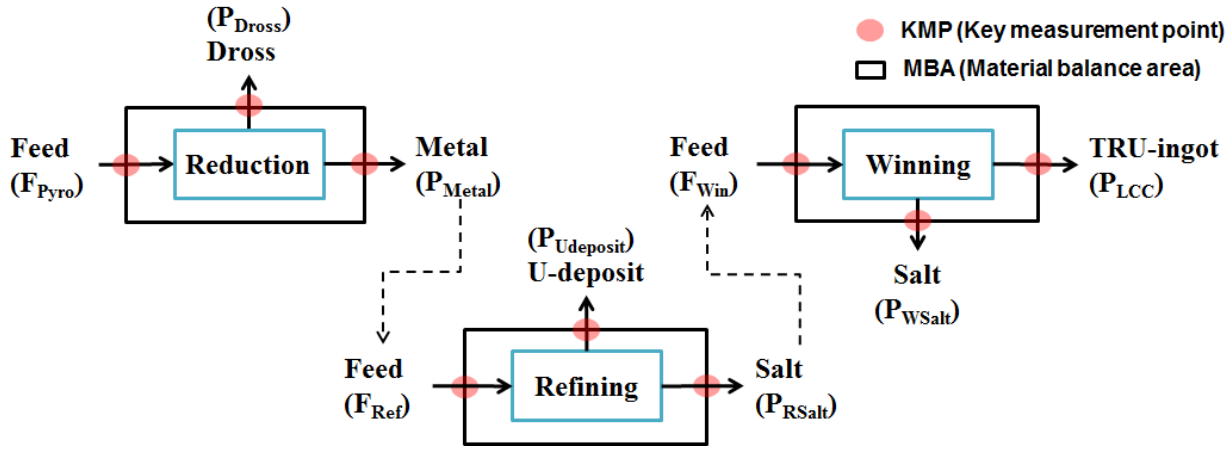

Figure 73 New modeling of MBA and KMP for the key-pyroprocess.

Electrolytic-reduction			Electro-refining			Electro-winning			Outcome
Feed (P_{Pyro})	Dross (P_{Dross})	Metal (P_{Metal})	Feed (P_{Ref})	U-deposit ($P_{Udeposit}$)	Salt (P_{RSalt})	Feed (P_{Win})	TRU-ingot (P_{LCC})	Salt (P_{WSalt})	

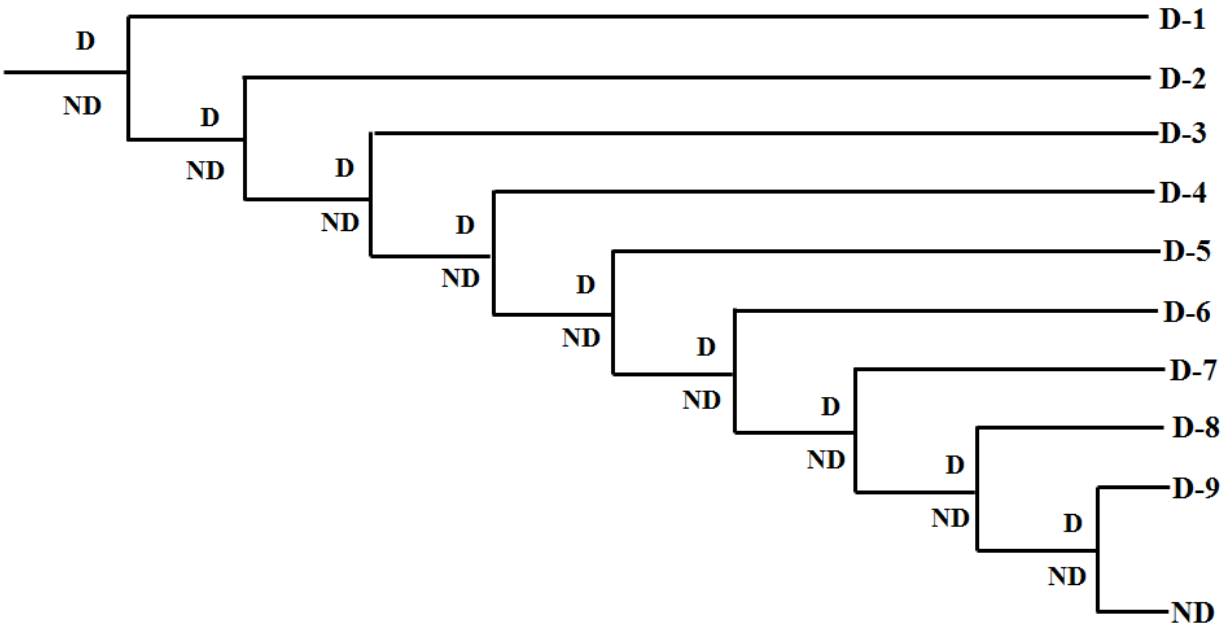

Figure 74 Event tree for a new MBA model.

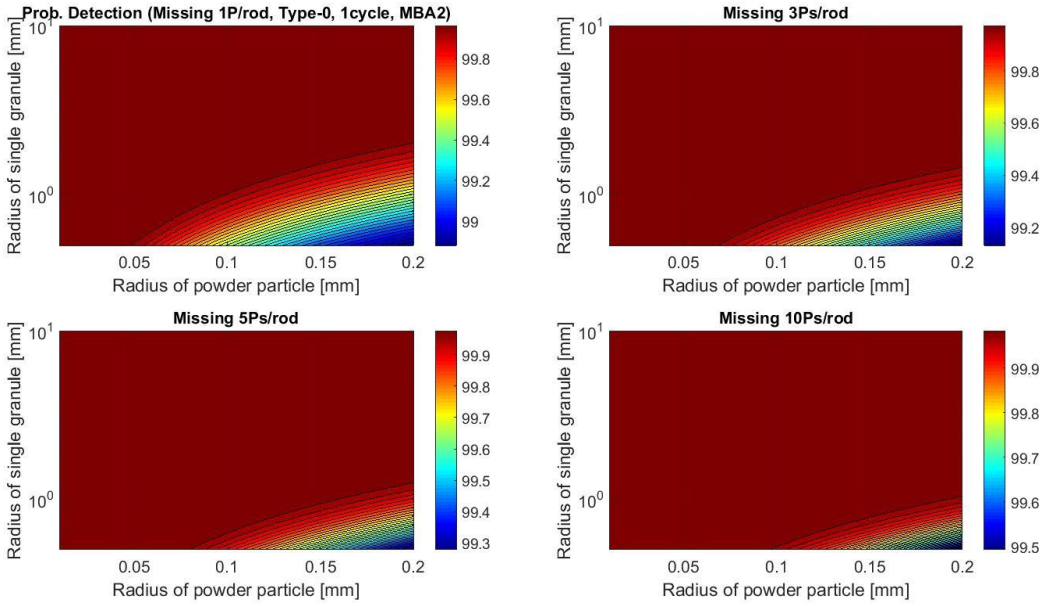

Figure 75 Probability of detection for the LOPu using the Type-0 assembly after 1cycle depletion in the new MBA model.

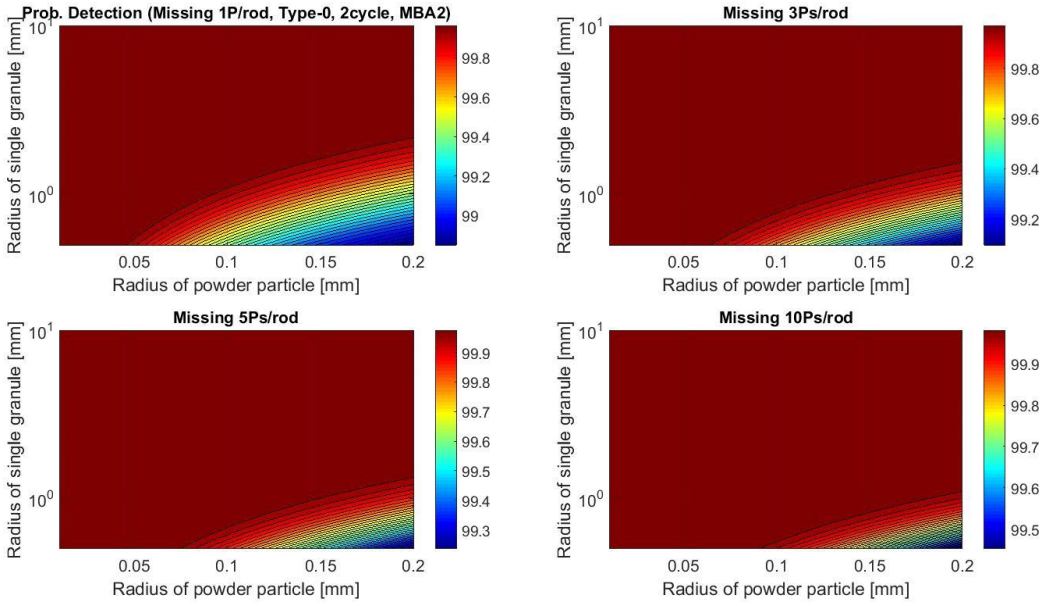

Figure 76 Probability of detection for the LOPu using the Type-0 assembly after 2cycles depletion in the new MBA model.

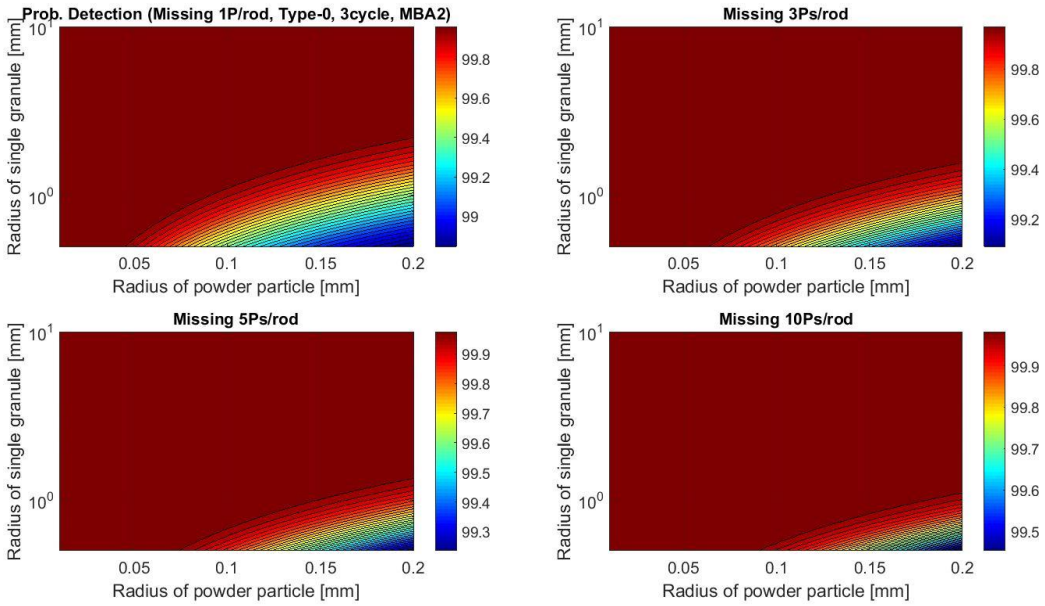

Figure 77 Probability of detection for the LOPu using the Type-0 assembly after 3cycles depletion in the new MBA model.

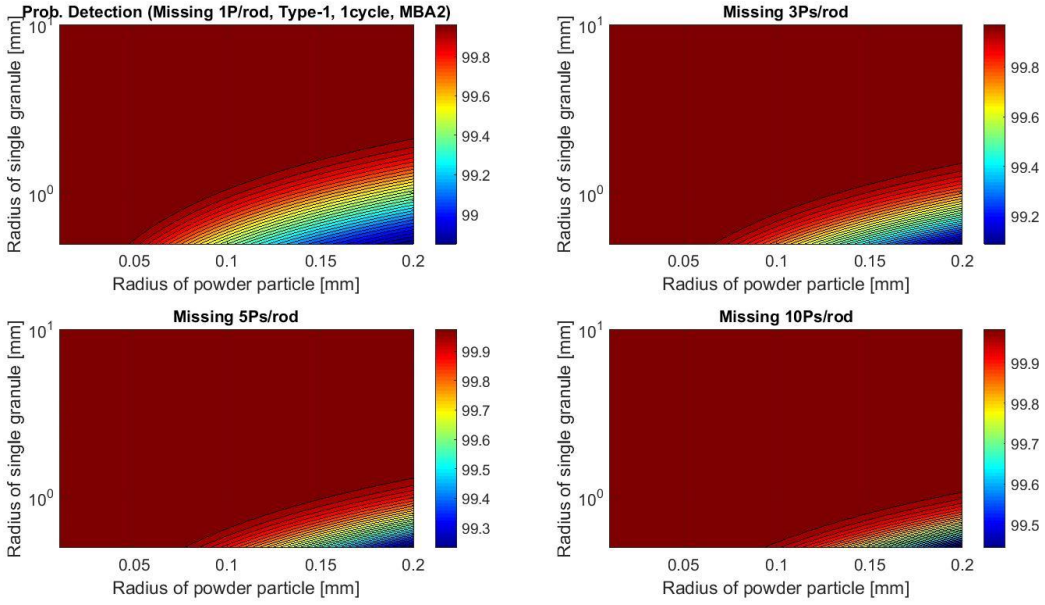

Figure 78 Probability of detection for the LOPu using the Type-1 assembly after 1cycle depletion in the new MBA model.

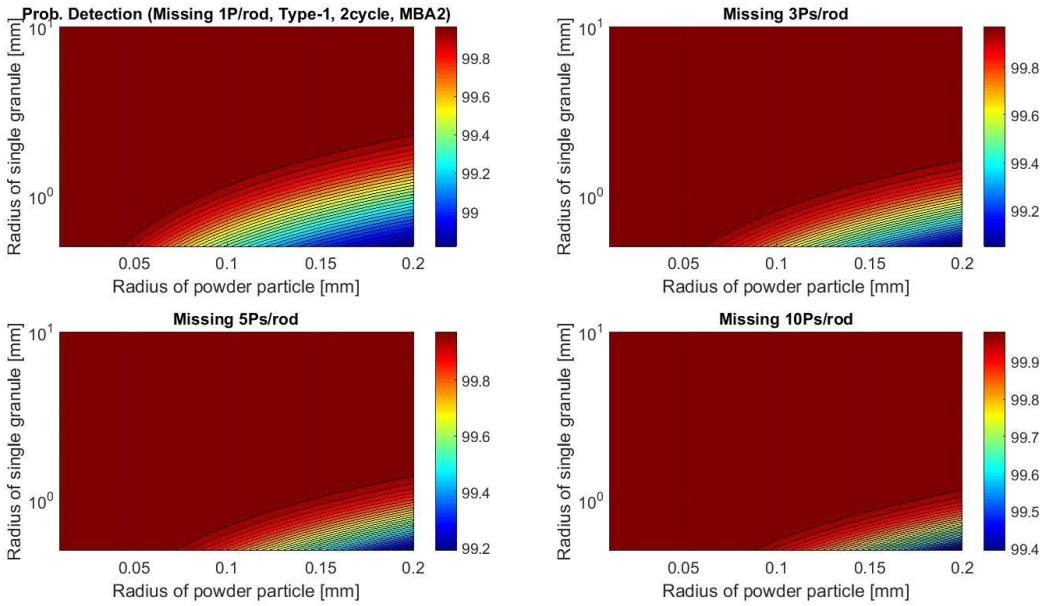

Figure 79 Probability of detection for the LOPu using the Type-1 assembly after 2cycles depletion in the new MBA model.

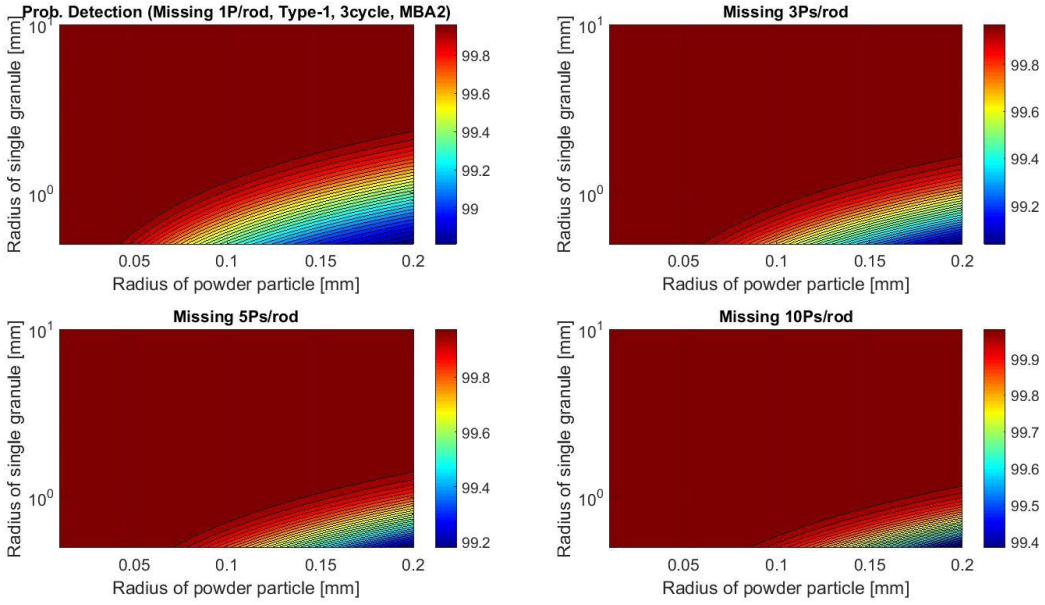

Figure 80 Probability of detection for the LOPu using the Type-1 assembly after 3cycles depletion in the new MBA model.

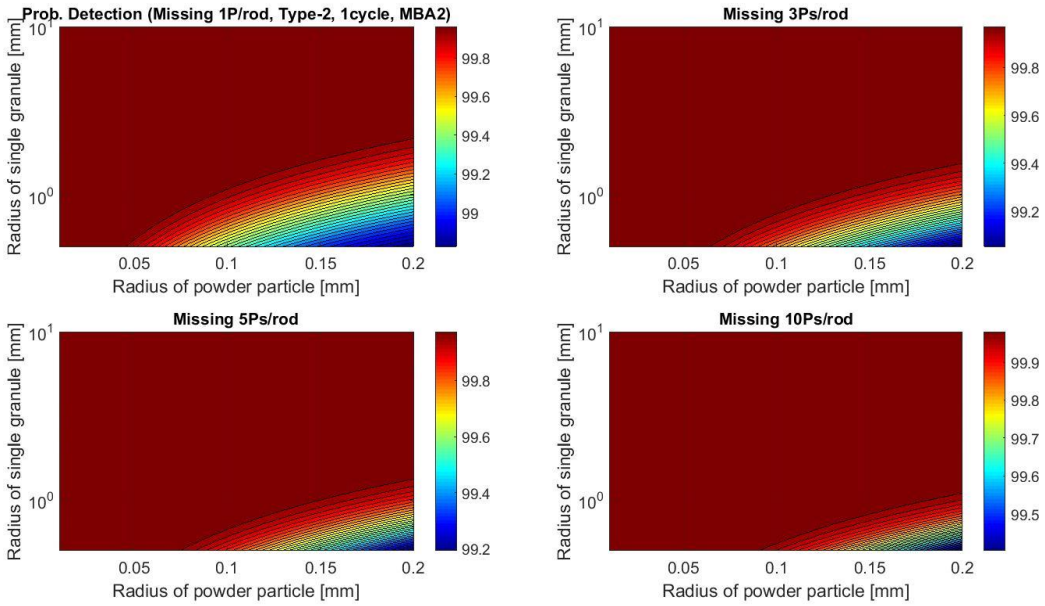

Figure 81 Probability of detection for the LOPu using the Type-2 assembly after 1cycle depletion in the new MBA model.

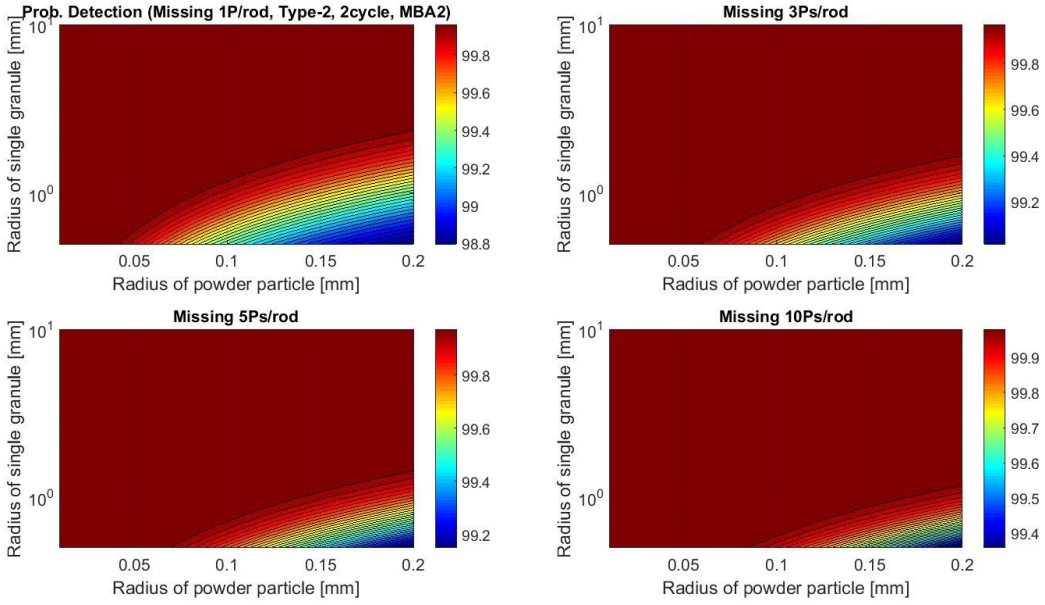

Figure 82 Probability of detection for the LOPu using the Type-2 assembly after 2cycles depletion in the new MBA model.

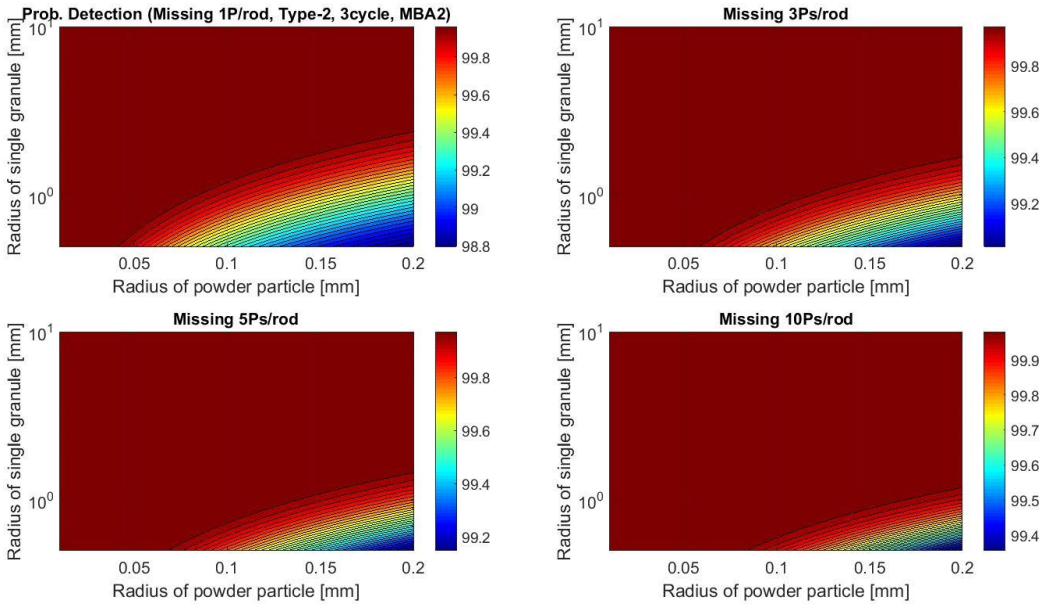

Figure 83 Probability of detection for the LOPu using the Type-2 assembly after 3cycles depletion in the new MBA model.

Secondly, in order to discuss the effect of increasing sample sizes, the probability of detection for the LOPu using the Type-0 spent fuel assembly after 1 cycle depletion based on 1, 3 and 10 granules sample size cases have been plotted in Figure 64, Figure 84, and Figure 85, respectively. The results of 3 granules case shows increasing the area of detection probability greater than 95%. That area significantly increases when the granule sample size is increased to 10. However, the probability of detection for the 1 piece missing case shows still many possibilities of the probability less than 95%. The number of assemblies necessary for the LOPu to be 8 kg for that case is approximately 1000 as shown in Table 21. The 4.6 assemblies are planned to be treated in the KAPF+ system. By that, it would take 218 days for processing of 1,000 Type-0 spent fuel assemblies. The multiple campaign could be scheduled during such long days. After every campaign, the close inspection should be conducted by both operators and inspectors. Those inspection and verification works would decrease reaching of the 8kg LOPu. Even though that would be a kind of practical view point, the probability of detection for missing material in the system should be kept as high as possible.

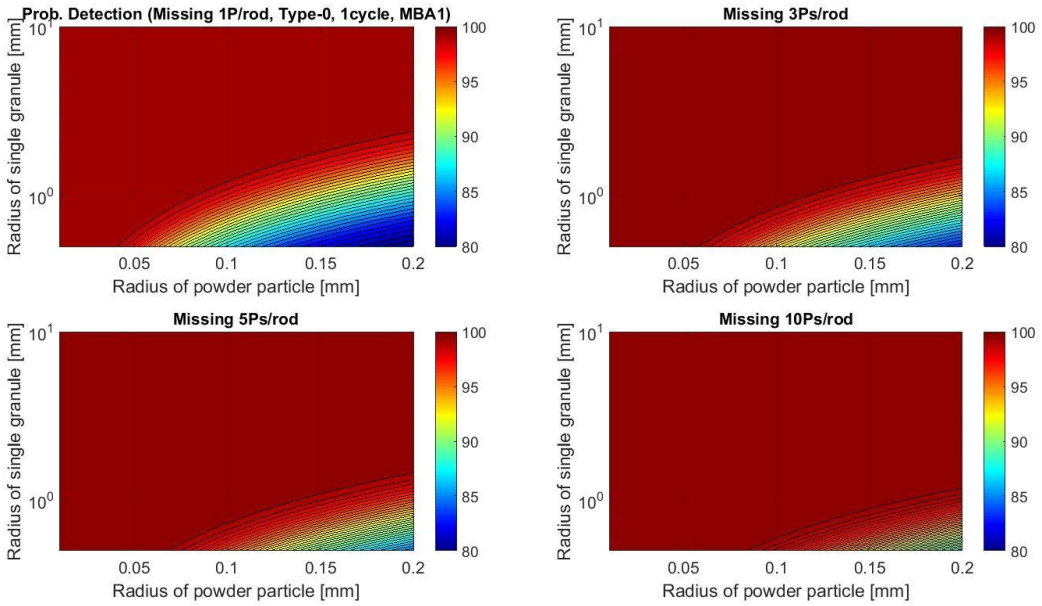

Figure 84 Probability of detection for the LOPu using the Type-0 assembly after 1cycle depletion based on the 3 granules sample size.

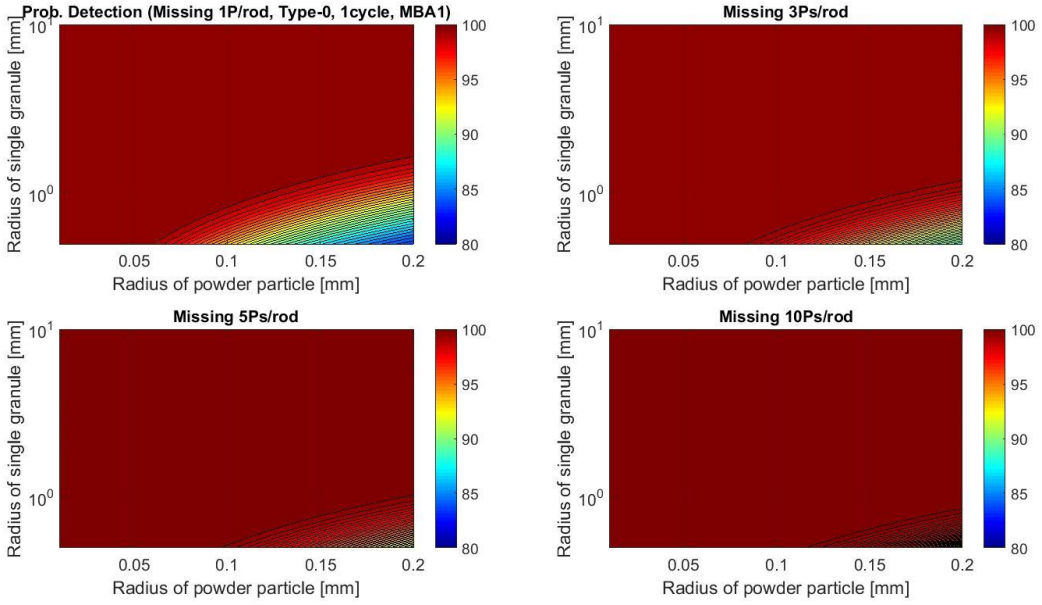

Figure 85 Probability of detection for the LOPu using the Type-0 assembly after 1cycle depletion based on the 10 granules sample size.

Chapter 4

Summary and Conclusions

A methodology to evaluate material accountability in pyroprocess has been developed. Among several uncertainty sources for material accounting in the system, this study focused on how the non-uniform nuclide composition in spent fuel assemblies could affect material accounting.

First, numerical recipes for high-fidelity depletion simulations were developed using SERPENT. Due to a lack of information for benchmarking simulations and verification of simulation results, options for neutronic simulation and the depletion simulations were compared to determine which conditions should be taken into account to achieve the reliable nuclide composition in spent fuel. The four main options were considered; 1) the length of burnup step, 2) Xe-equilibrium calculation, 3) the axial moderator temperature variation, and 4) the axial resolution. A thorough analysis concluded that in order to improve accuracy of the nuclide composition distribution: short burnups step, 25 days or less, and 30 axial meshes or less, are preferable; Xe-equilibrium calculation and axial should be applied.

From the simulation results, analytical solutions for simplified depletion equations has been suggested in order to address the non-uniformity of nuclide composition in spent fuel. Obviously, the cosine shape of the axial neutron flux distribution dominates the axial non-uniformity of the nuclide composition. In addition, cross section and time influence the axial non-uniformity, because the exponential term in the analytical solution consists of the neutron flux, cross section and time. Among those three, only the cross section varies depending on nuclides. For example, the axial concentration distribution for a nuclide having the small cross section could be steeper than that for another nuclide having larger cross section because the axial flux distribution is weighted by the cross section in the exponential term of the solution. Similarly, the non-uniformity becomes flatter with increasing burnup, because the time term in the exponential term increases. These effects could be utilized to better understand how the non-uniform nuclide composition in spent fuel is generated.

Based on the developed numerical recipes, the axial composition distributions were obtained for the representative spent nuclear fuel assemblies, the Type-0, -1, and -2 assemblies after 1, 2, and 3 depletion cycles. Furthermore, the normalized radial concentration distributions for normal-enriched fuel rods, low-enriched fuel rods, and GBFs are predetermined as a function of the axial location. The decoupling of two independent simulation results was conducted by matching axial height of fuel rods. These obtained data were appropriately modified to depict processing for materials in the head-end process of pyroprocess such as the chopping, voloxidation and granulation processes. The expectation and standard deviation of Pu-to-^{244}Cm-ratio in the single granule was evaluated by the central limit theorem and the GH transformation. Then, the

uncertainty propagation through the key-pyroprocess was applied to analyze the MUF in that system. Finally, the Type-I error for the Pu MUF was evaluated for spent fuel assemblies with respect the size of granules and powders. It was found that: (1) the probabilities of Type-I error for Pu MUF are partially greater than 5% which is the recommendation for material accountancy by IAEA, when the sizes of granule and powder particles are small and great; (2) the possibility of Type-I error greater than 5% increases by increasing the depletion period, because the increasing production of Pu and ^{244}Cm as burnup would more propagate the uncertainty through the system; (3) the major contributor to the uncertainty of the ratio is the non-uniformity of ^{244}Cm; (4) more Pu is generated in the Type-2 spent fuel assemblies due to more GBFs loading in the assembly, therefore, the area indicting the probability of Type-I error greater than 5% is the widest among the figures for the Type-0 and -1 spent fuel assemblies.

The random variable, LOPu, was defined as the original Pu mass minus the Pu mass after missing materials. This random variable can be more useful that the MUF for analyzing the probability of detection at the single KMP. The probability of detection for the 8 kg LOPu in the system is evaluated with respect the size of granule and powder using the event tree analysis and the hypothesis testing method. We can observe there are possible cases showing the probability of detection for the LOPu less than 95%. In order to enhance the detection rate, the new MBA model with increasing KMPs for the key-pyroprocess has been newly designed. The probabilities of detection for all spent fuel types based on the new MBA model are greater than 99%. As a second approach to enhance the detecting probability, increasing granules sample sizes for evaluating the ratio after the granulation process was discussed. When the sample size increases from 1 to 10 granules, the probability of detection for the LOPu is significantly increased. Based on these observations, even though the material accountability could be affected by the non-uniformity of nuclide composition, that could be surmounted by decreasing the uncertainty of ratio by increasing the sample size and modifying the MBAs and KMPs.

In summary, the main contributions of this study can be summarized as follows;

- Development of the numerical recipes for the high-fidelity depletion simulation to achieve the reliable nuclide composition data in spent fuel,
- Development of the methodology to evaluate the expectation of MUF and the probability of Type-I error for MUF in the pyroprocessing system,
- Development of the new methodology to evaluate the probability of detection for the 8 kg LOPu in pyroprocess,
- Optimal modeling of MBAs and KMPs as a function of detection probability.

As mentioned earlier, there are other uncertainty sources applicable the Pu-to-^{244}Cm-ratio method, for example, the uncertainty of measuring ^{244}Cm by counting neutrons emitted from spent fuel. Those factors would impact on the Pu material accountancy when the ratio method is being applied.

The half-life of ^{244}Cm is 18.1 years. Some of spent fuel assemblies have been stored more than 18 years after discharging. The suitability of the ratio method for those assembly in pyroprocess should be addressed. Moreover, the inaccuracy terms in determination of the ratio, for example, the uncertainty of nuclear data, or instrument errors, should be also addressed in the future.

Bibliography

[1] Y.I. Chang, The Integral Fast Reactor, Nucl. Technol. 88 (1988) 129–139.

[2] H. Lee, G. Il Park, K.H. Kang, J.M. Hur, J.G. Kim, D.H. Ahn, et al., Pyroprocessing technology development at KAERI, Nucl. Eng. Technol. 43 (2011) 317–328. doi:10.5516/NET.2011.43.4.317.

[3] E.H. Kim, Current status on development of P&T in Korea, in: Actin. Fission Prod. Partitioning Transmutat. Ninth Inf. Exch. Meet., Nimes, France, 2006: pp. 45–56.

[4] H.L. Chang, F.X. Gao, W.I. Ko, H.D. Kim, S.Y. Lee, Evaluation of Sigma-MUF (Material Unaccounted For) for the Conceptually Designed Korea Advanced Pyroprocess Facility, J. Korean Phys. Soc. 59 (2011) 1418. http://www.kps.or.kr/jkps/abstract_view.asp?articleuid=2CE51503-81A2-439E-A1C2-5C0C9E7D2531.

[5] W. Il Ko, H.H. Lee, S. Choi, S.K. Kim, B.H. Park, H.J. Lee, et al., Preliminary conceptual design and cost estimation for Korea Advanced Pyroprocessing Facility Plus (KAPF+), Nucl. Eng. Des. 277 (2014) 212–224.

[6] M.A. Williamson, J.L. Willit, Pyroprocessing flowsheets for recycling used nuclear fuel, Nucl. Eng. Technol. 43 (2011) 329–334.

[7] IAEA, Status of the Treatment of Irradiated LWR Fuel, IAEA-TECDOC-333, 1985.

[8] S. Jeon, J. Lee, J. Lee, S. Kang, K. Lee, Y. Cho, et al., Fabrication of UO2 Porous Pellets on a Scale of 30 kg-U / Batch at the PRIDE Facility, Adv. Mater. Sci. Eng. 2015 (2015).

[9] J. Lee, Y. Yun, Y. Kim, K. Cho, H. Park, G. Park, et al., Thermal granulation of U 3 O 8 powder using a rotary voloxidizer, Ceram. Int. 41 (2015) 10810–10817. doi:10.1016/j.ceramint.2015.05.020.

[10] S.C. Jeon, J.W. Lee, S.J. Kang, J.H. Lee, J.W. Lee, G. Park, et al., Temperature dependences of the reduction kinetics and densification behavior of U3O8 pellets in Ar atmosphere, Ceram. Int. 41 (2015) 657–662. doi:10.1016/j.ceramint.2014.08.118.

[11] S.K. Kim, W.I. Ko, S.R. Youn, R. Gao, Cost analysis of a commercial pyroprocess facility on the basis of a conceptual design in Korea, Ann. Nucl. Energy. 80 (2015) 28–39.

[12] J. Kim, S. Park, S. Hwang, Y. Kang, S. Lee, H. Lee, The Development of U-recovery by Continuous Electrorefining, J. Korean Radioact. Waste Soc. 8 (2010) 71–76.

[13] J.H. Yoo, C.S. Seo, E.H. Kim, H.S. Lee, A conceptual study of pyroprocessing for recovering actinides from spent oxide fuels, Nucl. Eng. Technol. 40 (2008) 581–592.

[14] IAEA, IAEA SAFEGUARDS 2001 Edition, IAEA, Vienna, Austria, 2001.

[15] N. Miura, H.O. Menlove, The use of curium neutrons to verify plutonium in spent fuel and reprocessing wastes, LA-12774-MS, 1994.

[16] M.L. Fensin, S.J. Tobin, N.P. Sandoval, M.T. Swinhoe, S.J. Thompson, A Monte Carlo linked depletion spent fuel library for assessing varied nondestructive asseay techniques for nuclear safeguards, in: Adv. Nucl. Fuel Manag. IV, LaGrange Park, IL, USA, 2009.

[17] H.D. Kim, H.R. Cha, W. Il Ko, H.Y. Kang, D.Y. Kim, S. Hong, et al., Technology Development on the DUPIC Safeguards System,LA-UR-01-0938, 2001.

[18] T.H. Lee, H.O. Menlove, S.Y. Lee, H.D. Kim, Development of the ACP safeguards neutron counter for PWR spent fuel rods, Nucl. Instruments Methods Phys. Res. Sect. A. 589 (2008) 57–65. doi:10.1016/j.nima.2008.02.054.

[19] R.A. Borrelli, Use of curium spontaneous fission neutrons for safeguardability of remotely-handled nuclear facilities: Fuel fabrication in pyroprocessing, Nucl. Eng. Des. 260 (2013) 64–77. doi:10.1016/j.nucengdes.2013.03.025.

[20] J.G. Richard, M.L. Fensin, S.J. Tobin, M.T. Swinhoe, J. Baciak, H.O. Menlove, Characterization of the neutron source term and muliplicity of a spent fuel assembly in support of NDA safeguards of spent nuclear fuel, LA-UR-10-03927, in: Inst. Nucl. Mater. Manag. 51st Annu. Meet., Baltimore, MD, USA, 2010.

[21] R.N. Bratton, M. Avramova, K. Ivanov, OECD/NEA Benchmark for Uncertainty Analysis in Modeling (UAM) for LWRs-Summary and Discussion of Neutronics cases (Phase I), Nucl. Eng. Technol. 46 (2014) 313–342.

[22] Y. Ando, K. Nishihara, H. Takano, Estimation of spent fuel compositions from Light Water Reactors, J. Nucl. Sci. Technol. 37 (2000) 924–933.

[23] T.-H. Lee, Y.-S. Kim, T.-J. Kwon, H.-S. Shin, H.-D. Kim, Determination of the Plutonium Mass and Curium Ratio of Spent Fuel Assemblies for Input Nuclear Material Accountancy of Pyroprocessing, and Analysis of Their Errors, Nucl. Technol. 179 (2012) 196–204.

[24] L. Zhang, Evaluation of high power density annular fuel application in the Korean OPR-1000 reactor, MIT, 2009.

[25] J. Leppänen, Serpent–a continuous-energy Monte Carlo reactor physics burnup calculation code, 2013.

[26] J.J. Duderstadt, L.J. Hamilton, Nuclear reactor analysis, JOHN WILEY & SONS, 2012.

[27] C.Y. Lee, C.H. Shin, W.K. In, Pressure drop in dual-cooled annular and cylindrical solid fuel assemblies for pressurized water reactor, Nucl. Eng. Des. 250 (2012) 287–293.

[28] H. Yu, Low-Boron OPR1000 core based on the BigT burnable absorber, KAIST, 2014.

[29] Y. Kim, K. Kim, J. Jung, B. Park, J. Yoon, H. Lee, Design of Remotely Operated Vol-oxidizer for Hot-cell Application, in: IEEE Int. Symp. Assem. Manuf., Suwon, Korea,

2009: pp. 393–397.

[30] Y.H. Kim, H.J. Lee, J.K. Lee, J.H. Jung, B.S. Park, J.S. Yoon, et al., Engineering Design of a High-Capacity Vol-Oxidizer for Handling UO2 Pellets of Tens of Kilogram, J. Nucl. Sci. Technol. 45 (2008) 617–624.

[31] S. Klinke, Dara structures for computational statistics, Springer-Verlag Berlin Heidelberg GmbH, 1997.

[32] W.G. Gilchrist, Statistical modeliing with quantile functions, CHAPMAN & HALL/CRC, 2000.

[33] C.M. Jarque, A.K. Bera, Efficient tests for normality, homoscedasticity and serial independence of regression resiguals, Econ. Lett. 6 (1980) 255–259.

[34] C.M. Jarcque, A.K. Bera, A test for normality of observations and regression residuals, Int. Stat. Rev. 55 (1987) 163–172.

[35] J.A. Johnson, Studies of reaction processes for voloxidation methods, University of Tennessee, Knoxville, 2013.

[36] S.M. Jeong, J.M. Hur, H. Lee, Kinetic modeling study of a voloxidation for the production of U3O8 powder from a UO2 pellet, Nucl. Eng. Technol. 41 (2009) 1073–1078.

[37] K.C. Song, G. IL Park, J.W. Lee, J.J. Park, Fractional release behavior of volatile and semivolatile fission products during a voloxidation and oreox treatment of spent PWR fuel, Nucl. Technol. 162 (2008) 158–168.

[38] B. Han, H. Shin, H. Kim, Analysis of Measurement Uncertainty of Material Unaccounted for in the Reference Pyroprocessing Management Technical Note, Nucl. Technol. 182 (2013).

[39] S. Ahn, H. Shin, H. Kim, Safeguardability analysis for an engineering scale pyroprocess facility, J. Nucl. Sci. Technol. 49 (2012) 632–639.

[40] S.M. Jeong, J.M. Hur, S.S. Hong, D.S. Kang, M.S. Choung, C.S. Seo, et al., An Electrochemical Reduction of Uranium Oxide in the Advanced Spent-Fuel Conditioning Process, Nucl. Technol. 162 (2008) 184–191.

[41] J.M. Hur, I.K. Choi, S.H. Cho, S.M. Jeong, C.S. Seo, Preparation and melting of uranium from U3O8, J. Alloys Compd. 452 (2008) 23–26. doi:10.1016/j.jallcom.2006.11.210.

[42] S.M. Ross, Introduction to probability and statistics for engineers and scientists, 4th ed., Academic Press, 2014.

[43] J. Hayya, D. Armstrong, N. Gressis, A Note on the Ratio of Two Normally Distributed Variables, Manage. Sci. 21 (1975) 1338–1341. doi:10.1287/mnsc.21.11.1338.

[44] IAEA, Nuclear Material Accounting Handbook, IAEA Services Series No. 15, 2008.

[45] US Department of Energy, DOE Fundamentals Handbook Nuclear Physics Volume 2 of 2,

DOE-HDBK-1019/2-93, 1993.

[46] A.E. Isotalo, J. Leppänen, J. Dufek, Preventing xenon oscillations in Monte Carlo burnup calculations by enforcing equilibrium xenon distribution, Ann. Nucl. Energy. 60 (2013) 78–85.

[47] N.E. Todreas, M.S. Kazimi., Nuclear systems: thermal hydraulic fundamentals. Vol. 1., Taylor & Francis Group, 1990.

[48] F.E. Osaisai, S.G. Prussin, D.R. Olander, Concentration profiles of neutron-induced radioactivities in UO2 fuel specimens, J. Nucl. Mater. 173 (1990) 149–158.

[49] H. Matzke, On the rim effect in high burnup UO2LWR fuels, J. Nucl. Mater. 189 (1992) 141–148. doi:10.1016/0022-3115(92)90428-N.

[50] M.E. Cunningham, M.D. Freshley, D.D. Lanning, Development and characteristics of the rim region in high burnup UO2 fuel pellets, J. Nucl. Mater. 188 (1992) 19–27. doi:10.1016/0022-3115(92)90449-U.